

Simulating two-phase flows with thermodynamically consistent energy stable Cahn-Hilliard Navier-Stokes equations on parallel adaptive octree based meshes

Makrand A. Khanwale^a, Alec D. Lofquist^{a,1}, Hari Sundar^c, James A. Rossmanith^{b,*},
Baskar Ganapathysubramanian^{a,*}

^aDepartment of Mechanical Engineering, Iowa State University, Iowa, USA 50011

^bDepartment of Mathematics, Iowa State University, Iowa, USA 50011

^cSchool of Computing, The University of Utah, Salt Lake City, Utah, USA 84112

Abstract

We report on simulations of two-phase flows with deforming interfaces at various density contrasts by solving thermodynamically consistent Cahn-Hilliard Navier-Stokes equations. An (essentially) unconditionally energy-stable Crank-Nicolson-type time integration scheme is used. Detailed proofs of energy stability of the semi-discrete scheme and for the existence of solutions of the advective-diffusive Cahn-Hilliard operator are provided. We discretize spatial terms with a conforming continuous Galerkin finite element method in conjunction with a residual-based variational multi-scale (VMS) approach in order to provide pressure stabilization. We deploy this approach on a massively parallel numerical implementation using fast octree-based adaptive meshes. A detailed scaling analysis of the solver is presented. Numerical experiments showing convergence and validation with experimental results from the literature are presented for a large range of density ratios.

Keywords: two-phase flows, energy stable, adaptive finite elements, octrees, scalable

1. Introduction

Accurate description of the dynamics of the interface in two-phase flows is essential from two perspectives: (1) accurate resolution of interfacial shapes and (2) accurate calculations of the four-way interaction of the coupling between dispersed and continuous phases. These two perspectives significantly influence modeling strategies. For example, the former becomes important in the context of simulating equilibrium shapes of bubbles and droplets (for instance, in designing micro-fluidic devices for effective bio-separations and related material science applications). The latter becomes important for understanding the fundamental coupling of energies due to the motions of the dispersed phase, for example in bubbly flows. While important, modeling two phase flows with a resolved description of the interfacial dynamics is challenging because of discontinuities due to surface tension and topological changes of the interface.

*Corresponding authors

Email addresses: khanwale@iastate.edu (Makrand A. Khanwale), alces14@gmail.com (Alec D. Lofquist), hari@cs.utah.edu (Hari Sundar), rossmani@iastate.edu (James A. Rossmanith), baskarg@iastate.edu (Baskar Ganapathysubramanian)

¹Presently at Affirm Inc., San Francisco, CA, USA

A standard approach to representing interfacial phenomena is to use jump boundary conditions, which requires interface-fitted meshes [1]. Although theoretically promising, this approach is non-trivial and impractical for large topological changes in the interfaces, especially in 3D. An alternative description of the interface is to smear the sharp discontinuity to a numerically resolvable length scale. There are many flavors of this approach; e.g., the popular level set methods [2] and front tracking approaches [3]. In these methods a tracking variable (or an indicator field) is used to track the interface (usually on a fixed grid). If one selects a physical property like density as an indicator function, and approximates the forcing due to the motion of the interface as the product of the gradient of the indicator function over the interface and the curvature of the interface, then we get the continuum surface models [4]. Each of these approaches has relative merits and demerits, and we refer the interested reader to the detailed discussion in Prosperetti and Tryggvason [5].

Phase field methods are another class of approaches to implicitly track interfaces. They offer some advantages including mass conservation, thermodynamic consistency and a natural way to account for external effects. The underlying idea of phase field models is similar to the level set methods, i.e. to use a smooth scalar field (phase field) to track the interface on a fixed grid. In phase field methods, an advective Cahn-Hilliard equation is used to track the motion of the (smeared or diffuse) interface. Compared to the level set advection equation, the advective Cahn-Hilliard equation has an added diffusive term that is inherent to the thermodynamic description of the interface. This diffusion term is analogous to numerical diffusion, which stabilizes the numerical schemes and improves mass conservation². The other advantage of using Cahn-Hilliard based phase field models is that the surface tension is represented via a free energy-based description with well established footing in thermodynamics [6, 7] (see Anderson et al. [8] and references therein for detailed discussion).

In all of these models a set of momentum equations are coupled with the interface tracking equation. Typically, a single set of momentum equations are solved for an “averaged mixture velocity” with variable density and viscosity (which are inferred from the phase field). Even for incompressible fluids, the solenoidality (divergence-free) of the averaged mixture velocity depends on the type of averaging (mass- or volume- averaging). Volume averaging usually results in solenoidal mixture velocity, while mass averaging results in a non-solenoidal mixture velocity leading to the so called quasi-incompressible models (see Guo et al. [9], Shokrpour Roudbari et al. [10], and references therein for the development of mass averaged models). The solenoidality of the mixture velocity is a useful feature while constructing numerical schemes³.

In the literature there are many versions of the Cahn-Hilliard Navier-Stokes (CHNS) coupled models [11, 7, 12, 13, 14]. Several of these models do not ensure thermodynamic consistency (i.e. ensure second law is followed) [7, 12, 14], nor are they compatible under high density and viscosity ratios of the two phases (model-H by Hohenberg and Halperin [11] was not compatible with unequal density ratios). Thus, while generally useful, there are no guarantees that such models work for high density and viscosity contrasts and remain predictive under long simulation horizons. The original CHNS model was developed for modeling binary fluids with equal densities and viscosities, which are the so-called model-H equations by Hohenberg and Halperin [11] and later extended for unequal densities and viscosities. Recasting these equations in a thermodynamically consistent manner was first attempted by Gurtin et al. [15], and the most recent contribution came from Abels et al. [16], who derive a thermodynamically consistent model with a solenoidal mixture velocity. In this paper we choose the model proposed by Abels et al. [16], which ensures that the

²We also show that this diffusive term helps in proving existence result for the phase field.

³This property however is only true under strictly isothermal conditions.

system follows an energy law consistent with the second law of thermodynamics and which does not assume equal densities and viscosities for the two fluids.

We identify three issues that have to be considered when designing numerical approaches for solving the CHNS equations. The first issue is that we would like to have a scheme that is provably energy-stable under a generously large time-step. This endows several promising traits to the numerical approach, including the ability to use larger time steps when marching towards a steady state solution (or towards a long time horizon). The second issue is the necessity of resolving the interfacial length scales for accurate capture of interface dynamics [14]. This becomes especially challenging during topological transitions (e.g. filaments, pinch-off points) with intricate changes over small length scales. In order to maintain computational efficiency, we require adaptive meshing strategies in order to resolve the interface properly. The need for adaptive meshing is especially important in 3D, where the degrees of freedom rise rapidly with the grid spacing. The third issue is the spatial discretization of the CHNS model, considering that the solenoidality of the velocity (i.e. the incompressibility constraint) requires satisfaction of the discrete inf-sup condition (see section 3.3 of [17] for details). We specifically desire a conforming Galerkin finite element approach for which efficient parallel h-refinement strategies are straightforward and available (for instance [18, 19, 20]). These three issues serve as the motivation for the current work. Specifically, our contributions are as follows.

1. **Energy stability:** We develop a time integration scheme that maintains energy stability for a large range of time steps while also satisfying mass conservation.
2. **Conforming finite elements via stabilization:** We develop a variational multiscale based treatment of the equations that allows us to use conforming Galerkin finite elements.
3. **Parallel adaptive meshing:** We implement the resulting numerical methods with a fast, massively parallel, adaptive meshing strategy based on octree meshes for resolving the length scales of the interface dynamics.

Energy stability: Kim et al. [21] reported one of the earliest studies on energy stable schemes for a CHNS model with equal densities⁴. Feng [22] (and then Han and Wang [23]) followed with a comprehensive analysis of this model reporting energy laws and other bounds on the numerical solutions. Shen and Yang [24, 25] extended this analysis for a CHNS model with unequal densities. Subsequently, Chen and Shen [26] reported analysis on the stability of time integration schemes along with a finite difference adaptive strategy for a thermodynamically consistent CHNS system. In other recent work, a Scalar Auxiliary Variable (SAV) approach has been proposed to construct energy stable schemes [27, 28]. Guo et al. [9] recently reported a detailed analysis for a mass averaged mixture velocity CHNS system. In section 3.2 of the present work we develop an implicit time scheme (similar to Crank-Nicolson) that is energy stable for large time steps, while also discretely mass conserving. The benefit of such a time integration scheme is that it does not require the storage of more than one previous time step, while still providing accuracy and ensuring energy stability. We prove that the time scheme is (essentially) unconditionally energy stable. We also subsequently prove in section 3.3 the existence of solutions of the time scheme.

Conforming finite elements via stabilization: In order to easily leverage parallel adaptive meshing tools it is helpful to have conforming finite elements. Most of the studies cited above used mixed element methods (LBB stable pairs of elements) to discretize the momentum equations in the coupled CHNS system. The distinct discrete spaces for pressure and velocities ensure local enforcement of solenoidality and satisfaction of the discrete inf-sup condition (also called the

⁴However, this model was not thermodynamically consistent.

saddle point problem). Alternatively, the saddle point problem can be resolved using stabilization (popularly known as *grad-div* stabilization), which enables using conforming finite elements. Variational multi-scale methods (VMS) provide a principled approach to derive such stabilization. They rely on a projection based decomposition of velocity and pressure fields into coarse and fine scale components following the ansatz of large eddy simulations [29]. There are multiple flavors of VMS models based on the choice of decomposition and how the fine scales are approximated. We refer interested readers to a recent and excellent review by Ahmed et al. [30]. In this work, we develop a formulation based on the Residual Based Variational Multi-scale Method (RBVMS) [31] with conforming Galerkin finite elements in section 3.4.

Parallel adaptive meshing: While the concept of adaptive space partitions is not novel, developing such methods for large distributed systems presents significant challenges. The challenge is to adaptively resolve the mesh [32, 33, 34], while ensuring appropriate load balancing across the computing cluster. A promising approach is to use structured meshes (especially based on octrees) [35], where the spatial structure of the elements is leveraged to design efficient data exchange and communication, thus resulting in fast parallel algorithms. In this work we use the octree based library DENDRO which is well-established for distributed octree-based (structured) meshing algorithms. DENDRO includes novel bottom-up octree construction algorithms that require only local computation followed by a single distributed sort [19, 20]. DENDRO also implements a 2:1 balancing algorithm⁵ that by preemptively communicating information between processes avoids synchronizations and has a provably lower communication cost. DENDRO, is freely available and has been used by several research groups across the world as the meshing scheme for a variety of methods such as finite element computations, fast multipole methods, fast Gauss transforms, and for a range of applications from cardiac biomechanics to direct numerical simulation of blood flow [20]. We detail adaptive meshing and scalability of our framework in section 4 and section 6, respectively.

2. Governing equations

Consider the bounded domain $\Omega \subset \mathbb{R}^n$, where $n = 2$ or 3 , containing two immiscible fluids, and consider the time interval $[0, T]$. Let ρ_+ (η_+) and ρ_- (η_-) denote the specific density (viscosity) of the fluids, respectively. We define a phase field, ϕ , that tracks the fluids, i.e. takes a value of $+1$ and -1 in domains occupied by each of the fluids, respectively. ϕ varies continuously across the interface between $+1$ and -1 . The non-dimensional density⁶ is given by $\rho(\phi) = \alpha\phi + \beta$, where $\alpha = \frac{\rho_+ - \rho_-}{2\rho_+}$ and $\beta = \frac{\rho_+ + \rho_-}{2\rho_+}$. Similarly, non-dimensional viscosity is given by $\eta(\phi) = \gamma\phi + \xi$, where

⁵Enforcing that adjacent octants differ by at most a factor of 2 in size is a condition often enforced during meshing to make subsequent numerical calculations convenient.

⁶Our non-dimensional form uses the specific density/viscosity of fluid 1 as the non-dimensionalising density/viscosity.

$\gamma = \frac{\eta_+ - \eta_-}{2\eta_+}$ and $\xi = \frac{\eta_+ + \eta_-}{2\eta_+}$. The governing equations in their non-dimensional form are as follows:

$$\text{Momentum Eqns: } \frac{\partial (\rho(\phi)v_i)}{\partial t} + \frac{\partial (\rho(\phi)v_i v_j)}{\partial x_j} + \frac{1}{Pe} \frac{\partial (J_j v_i)}{\partial x_j} + \frac{Cn}{We} \frac{\partial}{\partial x_j} \left(\frac{\partial \phi}{\partial x_i} \frac{\partial \phi}{\partial x_j} \right) + \frac{1}{We} \frac{\partial p}{\partial x_i} - \frac{1}{Re} \frac{\partial}{\partial x_j} \left(\eta(\phi) \frac{\partial v_i}{\partial x_j} \right) - \frac{\rho(\phi) \hat{g}_i}{Fr} = 0, \quad (1)$$

$$\text{Thermo Consistency: } J_i = \frac{(\rho_- - \rho_+)}{2} m(\phi) \frac{\partial \mu}{\partial x_i}, \quad (2)$$

$$\text{Solenoidality: } \frac{\partial v_i}{\partial x_i} = 0, \quad (3)$$

$$\text{Continuity: } \frac{\partial \rho(\phi)}{\partial t} + \frac{\partial (\rho(\phi)v_i)}{\partial x_i} + \frac{1}{Pe} \frac{\partial J_i}{\partial x_i} = 0, \quad (4)$$

$$\text{Chemical Potential: } \mu = \psi'(\phi) - Cn^2 \frac{\partial}{\partial x_i} \left(\frac{\partial \phi}{\partial x_i} \right), \quad (5)$$

$$\text{Cahn-Hilliard Eqn: } \frac{\partial \phi}{\partial t} + \frac{\partial (v_i \phi)}{\partial x_i} - \frac{1}{PeCn} \frac{\partial}{\partial x_i} \left(\frac{\partial (m(\phi)\mu)}{\partial x_i} \right) = 0. \quad (6)$$

In the above equations, \mathbf{v} is the volume averaged mixture velocity⁷, p is the volume averaged pressure, ϕ is the phase field (interface tracking variable), and μ is the chemical potential. The mobility, $m(\phi)$, is assumed to be a constant with a value of one. The non-dimensional parameters are as follows: Peclet: $Pe = \frac{u_r L_r^2}{m\sigma}$; Reynolds: $Re = \frac{u_r L_r}{\nu_r}$; Weber: $We = \frac{\rho_r u_r^2 L_r}{\sigma}$; Cahn: $Cn = \frac{\varepsilon}{L_r}$; and Froude: $Fr = \frac{u_r^2}{g L_r}$. u_r and L_r denote the reference velocity and length, respectively. $\hat{\mathbf{g}}$ is a unit vector defined as $(0, -1, 0)$ denoting the direction of gravity. ε is the interfacial thickness. $\psi(\phi(\mathbf{x}))$ is a known free-energy function. For the detailed analysis and importance of the thermodynamic consistency term see Zhu et al. [36, 37]. We use the polynomial form of the free energy density defined as follows:

$$\psi(\phi) = \frac{1}{4} (\phi^2 - 1)^2 \quad \text{and} \quad \psi'(\phi) = \phi^3 - \phi. \quad (7)$$

The system of equations eq. (1) – eq. (6) has a dissipative energy law given by:

$$\frac{dE_{\text{tot}}}{dt} = -\frac{1}{Re} \int_{\Omega} \frac{\eta(\phi)}{2} \|\nabla \mathbf{v}\|_F^2 d\mathbf{x} - \frac{Cn}{We} \int_{\Omega} m(\phi) \|\nabla \mu\|^2 d\mathbf{x}, \quad (8)$$

where the total energy is

$$E_{\text{tot}}(\mathbf{v}, \phi, t) = \int_{\Omega} \frac{1}{2} \rho \|\mathbf{v}\|^2 d\mathbf{x} + \frac{1}{CnWe} \int_{\Omega} \left(\psi(\phi) + \frac{Cn^2}{2} \|\nabla \phi\|^2 + \frac{1}{Fr} \rho(\phi) y \right) d\mathbf{x}. \quad (9)$$

The norms used in the above expression are the Euclidean vector norm and the Frobenius matrix norm:

$$\|\mathbf{v}\|^2 := \sum_i |v_i|^2 \quad \text{and} \quad \|\nabla \mathbf{v}\|_F^2 := \sum_i \sum_j \left| \frac{\partial v_i}{\partial x_j} \right|^2. \quad (10)$$

⁷We use Einstein notation throughout the manuscript. In this notation v_i represents the i^{th} component of the vector \mathbf{v} , and any repeated index is implicitly summed over.

Remark 1. Realistically, the thickness of the interface (parametrized by the Cahn number) is usually in the nanometer range. Resolving this scale is computationally intractable, as all the other scales in the problem are much larger. Therefore, a standard ansatz that diffuse interface models follow is that the solution tends to the real physics in the limit of $Cn \rightarrow 0$. Usually, one starts from a coarse Cahn number and decreases it until the simulated dynamics is independent of the Cahn number. However, the choice of Cahn number, Cn , determines the Peclet number: Pe . The Peclet number, $Pe = \frac{u_r L_r^2}{m\sigma}$, is the ratio of the advection timescale to the time scale of the diffuse interface to relax to an equilibrium \tanh profile (which is a purely computational construct). Magaletti et al. [38] reported a careful asymptotic analysis of these timescales and suggests the scaling: $1/Pe = \alpha Cn^2$. We use this scaling with $\alpha = 3$.

Remark 2. The volume averaged mixture velocity (\mathbf{v}) is solenoidal (see eq. (3)), but momentum ($\rho\mathbf{v}$) is not (see eq. (4)). Equation (4) is the mass conservation law, and technically the solenoidality of the mixture velocity has nothing to do with mass conservation law, but it is a convenient feature of the model. We make this distinction because in the context of incompressible Newtonian single phase flow, mass conservation reduces to solenoidality of the velocity field (the d'Alembert condition), which is not the case here.

3. Numerical method and its properties

We seek a Crank-Nicolson type time-stepping scheme for the set of equations given by eq. (1) – eq. (6). Such a method will provide accuracy and stability for large time-steps with storage of only one previous time-step. Additionally, using this implicit time scheme allows us to prove existence of solutions in the semi-discrete sense for the Cahn-Hilliard equation.

Let δt be a time-step; let any time be given by $t^k := k\delta t$; and let us define the following time-averages:

$$\tilde{\mathbf{v}}^k := \frac{\mathbf{v}^k + \mathbf{v}^{k+1}}{2}, \quad \tilde{p}^k := \frac{p^{k+1} + p^k}{2}, \quad \tilde{\phi}^k := \frac{\phi^k + \phi^{k+1}}{2}, \quad \text{and} \quad \tilde{\mu}^k := \frac{\mu^k + \mu^{k+1}}{2}, \quad (11)$$

and the following potential function evaluations:

$$\tilde{\psi} := \psi(\tilde{\phi}^k) \quad \text{and} \quad \tilde{\psi}' := \psi'(\tilde{\phi}^k). \quad (12)$$

With these definitions, the time-discretized scheme can be written as follows:

$$\begin{aligned} \text{Momentum Eqns: } & \rho(\phi^{k+1}) \frac{(v_i^{k+1} - v_i^k)}{\delta t} + \rho(\phi^{k+1}) \tilde{v}_j^k \frac{\partial \tilde{v}_i^k}{\partial x_j} + \frac{1}{Pe} \tilde{J}_j^k \frac{\partial \tilde{v}_i^k}{\partial x_j} \\ & + \frac{Cn}{We} \frac{\partial}{\partial x_j} \left(\frac{\partial \tilde{\phi}^k}{\partial x_i} \frac{\partial \tilde{\phi}^k}{\partial x_j} \right) + \frac{1}{We} \frac{\partial \tilde{p}^k}{\partial x_i} - \frac{1}{Re} \frac{\partial}{\partial x_j} \left(\eta(\phi^{k+1}) \frac{\partial \tilde{v}_i^k}{\partial x_j} \right) \\ & - \frac{\rho(\phi^{k+1}) \hat{g}_i}{Fr} = 0, \end{aligned} \quad (13)$$

$$\text{Thermo Consistency: } \tilde{J}_i^k = \frac{(\rho_- - \rho_+)}{2} \frac{\partial \tilde{\mu}^k}{\partial x_i}, \quad (14)$$

$$\text{Solenoidality: } \frac{\partial \tilde{v}_i^k}{\partial x_i} = 0, \quad (15)$$

$$\text{Continuity: } \frac{(\rho(\phi^{k+1}) - \rho(\phi^k))}{\delta t} + \frac{\partial (\rho(\tilde{\phi}^k) \tilde{v}_i^k)}{\partial x_i} + \frac{1}{Pe} \frac{\partial \tilde{J}_i^k}{\partial x_i} = 0, \quad (16)$$

$$\text{Chemical Potential: } \tilde{\mu}^k = \tilde{\psi}' - Cn^2 \frac{\partial}{\partial x_i} \left(\frac{\partial \tilde{\phi}^k}{\partial x_i} \right), \quad (17)$$

$$\text{Cahn-Hilliard Eqn: } \frac{(\phi^{k+1} - \phi^k)}{\delta t} + \frac{\partial (\tilde{v}_i^k \tilde{\phi}^k)}{\partial x_i} - \frac{1}{PeCn} \frac{\partial}{\partial x_i} \left(\frac{\partial \tilde{\mu}^k}{\partial x_i} \right) = 0, \quad (18)$$

with boundary conditions $\frac{\partial \tilde{u}}{\partial x_i} \hat{n}_i = 0$, $\frac{\partial \tilde{\phi}}{\partial x_i} \hat{n}_i = 0$, where $\hat{\mathbf{n}}$ is the outward pointing normal to the boundary $\partial\Omega$, and $\tilde{\mathbf{v}}^k = \mathbf{0}$ on $\partial\Omega$. In the definition below we use the notation that $\mathbf{v} \in \mathbf{H}_0^1 \implies \mathbf{v} = \mathbf{0}$ on $\partial\Omega$. Note that we have chosen to write the momentum equation, eq. (13), in convective form by combining the conservative form, eq. (1), and the continuity equation, eq. (4).

3.1. Fully discrete scheme

The fully discrete method proposed in this work is a continuous Galerkin (cG(1)) spatial discretization of eq. (13) – eq. (18). The fully discrete method is based on the variational form of eq. (13) – eq. (18), which we define below.

Definition 1. Let (\cdot, \cdot) be the standard L^2 inner product. The time-discretized variational problem can stated

as follows: find $\mathbf{v}^{k+1}(\mathbf{x}) \in \mathbf{H}_0^1(\Omega)$, $p^{k+1}(\mathbf{x})$, $\phi^{k+1}(\mathbf{x})$, $\mu^{k+1}(\mathbf{x}) \in H^1(\Omega)$ such that

$$\begin{aligned} \text{Momentum Eqns: } & \left(w_i, \rho(\phi^{k+1}) \frac{(v_i^{k+1} - v_i^k)}{\delta t} \right) + \left(w_i, \rho(\phi^{k+1}) \tilde{v}_j^k \frac{\partial \tilde{v}_i^k}{\partial x_j} \right) \\ & + \frac{1}{Pe} \left(w_i, \tilde{J}_j^k \frac{\partial \tilde{v}_i^k}{\partial x_j} \right) - \frac{Cn}{We} \left(\frac{\partial w_i}{\partial x_j}, \frac{\partial \tilde{\phi}^k}{\partial x_i} \frac{\partial \tilde{\phi}^k}{\partial x_j} \right) - \frac{1}{We} \left(\frac{\partial w_i}{\partial x_i}, \tilde{p}^k \right) \\ & + \frac{1}{Re} \left(\frac{\partial w_i}{\partial x_j}, \eta(\phi^{k+1}) \frac{\partial \tilde{v}_i^k}{\partial x_j} \right) - \left(w_i, \frac{\rho(\phi^{k+1}) \hat{g}_i}{Fr} \right) = 0, \end{aligned} \quad (19)$$

$$\text{Thermo Consistency: } \tilde{J}_i^k = \frac{(\rho_- - \rho_+)}{2} \frac{\partial \tilde{\mu}^k}{\partial x_i}, \quad (20)$$

$$\text{Solenoidality: } \left(q, \frac{\partial \tilde{v}_i^k}{\partial x_i} \right) = 0, \quad (21)$$

$$\text{Chemical Potential: } - \left(q, \tilde{\mu}^k \right) + \left(q, \tilde{\psi}' \right) + Cn^2 \left(\frac{\partial q}{\partial x_i}, \frac{\partial \tilde{\phi}^k}{\partial x_i} \right) = 0, \quad (22)$$

$$\text{Cahn-Hilliard Eqn: } \left(q, \frac{\phi^{k+1} - \phi^k}{\delta t} \right) - \left(\frac{\partial q}{\partial x_i}, \tilde{v}_i^k \tilde{\phi}^k \right) + \frac{1}{PeCn} \left(\frac{\partial q}{\partial x_i}, \frac{\partial \tilde{\mu}^k}{\partial x_i} \right) = 0, \quad (23)$$

$\forall \mathbf{w} \in \mathbf{H}_0^1(\Omega)$, $\forall q \in H^1(\Omega)$, given $\mathbf{v}^k \in \mathbf{H}_0^1(\Omega)$, and $\phi^k, \mu^k \in H^1(\Omega)$.

We solve the cG(1) approximated version of variational problem eq. (19) – eq. (23) using a block iteration technique, i.e., we treat the Navier-Stokes equations and the Cahn-Hilliard equations as two distinct sub-problems. Thus, two non-linear solvers are stacked together inside the time loop. These non-linear solvers are solved self-consistently until the change (error between current non-linear solve and previous non-linear solve) in the respective solutions is less than a set tolerance within every time step. See fig. 1 for a flowchart of the approach. We emphasize that a block iterative approach allows us to make the coupling variables from one equation constant in the other during each respective non-linear solve. For example, for the momentum equation, all the terms depending on ϕ (which is solved in the Cahn-Hilliard sub problem) are known. Similarly the mixture velocity used in the Cahn-Hilliard equation solve is known.

Remark 3. While $\phi \in [-1, 1]$ in the original equations, there is a possibility of excursions of ϕ outside these bounds due to numerical errors. While this does not adversely affect the ϕ evolution (i.e. the CH equation), it may cause non-positivity of the mixture density $\rho(\phi)$ and the mixture viscosity $\eta(\phi)$, which directly depend on ϕ . This causes drift of the bulk phase density from the true specific density of that phase, with some locations exhibiting negative density (or viscosity). This effect is especially possible for very high density ratio between the two fluids, like in the case of a water-air system ($1 : 10^{-3}$). A simple fix for this issue is by saturation scaling, i.e., pulling back the value of ϕ only for the calculation of density and viscosity. We therefore define ϕ^* that is only used for the calculation of mixture density and viscosity, where ϕ^* is given by:

$$\phi^* := \begin{cases} \phi, & \text{if } |\phi| \leq 1, \\ \text{sign}(\phi), & \text{otherwise.} \end{cases} \quad (24)$$

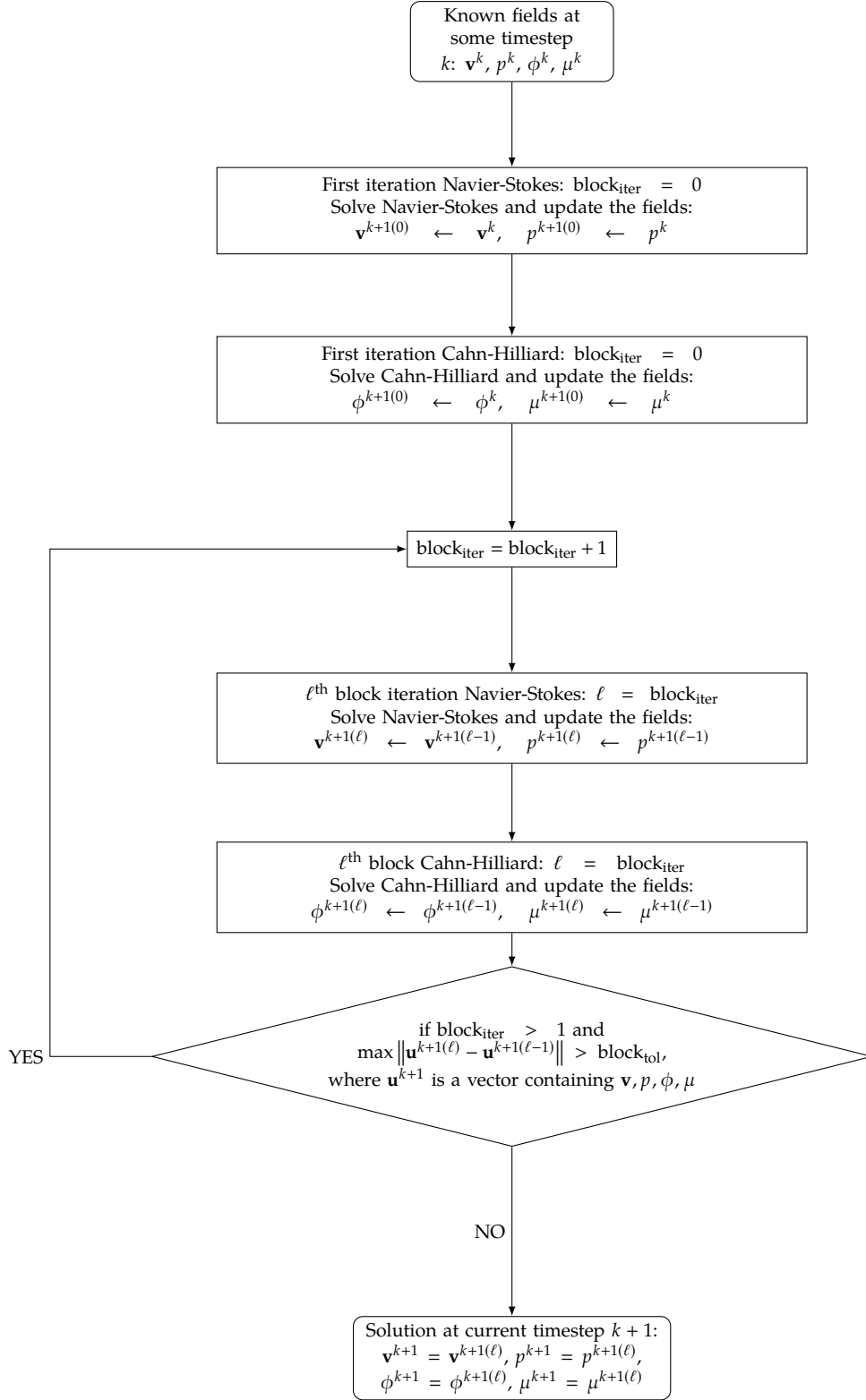


Figure 1: Flowchart for the block iteration technique as described in section 3.1 .

Remark 4. It is important to note here that we are using the block iteration technique. Therefore, ϕ and μ are known when solving momentum equations and v_i is known when solving the advective Cahn-Hilliard equation. The theorems and proofs we present in the subsequent subsections all assume that we are using the block iterative technique. However, it is not difficult to extend these theorems and proofs for the case of a fully coupled implementation; the theorems of unconditional stability and existence presented here hold even in the fully coupled case.

3.2. Energy stability of the time-stepping scheme

In this subsection we give a rigorous proof of the energy-stability of the time-stepping scheme as described above. We begin with a result about mass conservation.

Proposition 1 (Mass conservation). *The scheme given by eq. (19) – eq. (23) with the following boundary conditions:*

$$\frac{\partial \tilde{\mu}}{\partial x_i} \hat{n}_i \Big|_{\partial\Omega} = 0, \quad \frac{\partial \tilde{\phi}}{\partial x_i} \hat{n}_i \Big|_{\partial\Omega} = 0, \quad \tilde{\mathbf{v}}^k \Big|_{\partial\Omega} = \mathbf{0}, \quad (25)$$

where $\hat{\mathbf{n}}$ is the outward pointing normal to the boundary $\partial\Omega$, is globally mass conservative:

$$\int_{\Omega} \phi^{k+1} \, d\mathbf{x} = \int_{\Omega} \phi^k \, d\mathbf{x}. \quad (26)$$

This is a well known result shown previously in literature [9, 22]. The proof involves selecting the test function as $1.0 \in H^1(\Omega)$ in the variational form of eq. (19) – eq. (23) (see definition 1) and proving the integral of the time derivative to be zero. Since this is a well-known result, we do not provide the proof here. We verify the claim numerically in the results section for a wide variety of canonical problems.

Lemma 1 (Weak equivalence of forcing). *The forcing term due to Cahn-Hilliard in the momentum equation, eq. (19), with the test function $w_i = \delta t \, \tilde{v}_i^k$, can be written equivalently as*

$$\frac{Cn}{We} \left(\frac{\partial}{\partial x_j} \left(\frac{\partial \tilde{\phi}^k}{\partial x_i} \frac{\partial \tilde{\phi}^k}{\partial x_j} \right), \delta t \, \tilde{v}_i^k \right) = \frac{\delta t}{We Cn} \left(\tilde{\phi}^k \frac{\partial \tilde{\mu}^k}{\partial x_i}, \tilde{v}_i^k \right), \quad (27)$$

$\forall \, \tilde{\phi}^k, \tilde{\mu}^k \in H^1(\Omega)$, and $\forall \, \tilde{\mathbf{v}}^k \in \mathbf{H}_0^1(\Omega)$, where $\mathbf{v}^k, \mathbf{v}^{k+1}, p^k, p^{k+1}, \phi^k, \phi^{k+1}, \mu^k, \mu^{k+1}$, satisfy eq. (19) – eq. (23).

Proof. To prove this we will manipulate $\frac{\partial}{\partial x_j} \left(\frac{\partial \tilde{\phi}^k}{\partial x_i} \frac{\partial \tilde{\phi}^k}{\partial x_j} \right)$ using vector calculus. Using the product rule we have:

$$\begin{aligned} \frac{\partial}{\partial x_j} \left(\frac{\partial \tilde{\phi}^k}{\partial x_i} \frac{\partial \tilde{\phi}^k}{\partial x_j} \right) &= \frac{\partial \tilde{\phi}^k}{\partial x_i} \left(\frac{\partial}{\partial x_j} \left(\frac{\partial \tilde{\phi}^k}{\partial x_j} \right) \right) + \frac{\partial \tilde{\phi}^k}{\partial x_j} \left(\frac{\partial}{\partial x_j} \left(\frac{\partial \tilde{\phi}^k}{\partial x_i} \right) \right) \\ &= \frac{\partial \tilde{\phi}^k}{\partial x_i} \left(\frac{\partial}{\partial x_j} \left(\frac{\partial \tilde{\phi}^k}{\partial x_j} \right) \right) + \frac{1}{2} \frac{\partial}{\partial x_i} \left(\frac{\partial \tilde{\phi}^k}{\partial x_j} \frac{\partial \tilde{\phi}^k}{\partial x_j} \right), \end{aligned} \quad (28)$$

where the second equality follows from proposition 3 in [Appendix A](#). We manipulate this expression to write it in terms of μ :

$$\begin{aligned} \frac{\partial}{\partial x_j} \left(\frac{\partial \tilde{\phi}^k}{\partial x_i} \frac{\partial \tilde{\phi}^k}{\partial x_j} \right) &= \frac{\partial \tilde{\phi}^k}{\partial x_i} \left(\frac{\partial}{\partial x_j} \left(\frac{\partial \tilde{\phi}^k}{\partial x_j} \right) \right) + \frac{1}{2} \frac{\partial}{\partial x_i} \left(\frac{\partial \tilde{\phi}^k}{\partial x_j} \frac{\partial \tilde{\phi}^k}{\partial x_j} \right) + \frac{1}{Cn^2} \tilde{\psi}' \frac{\partial \tilde{\phi}^k}{\partial x_i} - \frac{1}{Cn^2} \tilde{\psi}' \frac{\partial \tilde{\phi}^k}{\partial x_i}, \\ &= \frac{\partial \tilde{\phi}^k}{\partial x_i} \left(\frac{\partial}{\partial x_j} \left(\frac{\partial \tilde{\phi}^k}{\partial x_j} \right) - \frac{1}{Cn^2} \tilde{\psi}' \right) + \frac{1}{2} \frac{\partial}{\partial x_i} \left(\frac{\partial \tilde{\phi}^k}{\partial x_j} \frac{\partial \tilde{\phi}^k}{\partial x_j} \right) + \frac{1}{Cn^2} \tilde{\psi}' \frac{\partial \tilde{\phi}^k}{\partial x_i}. \end{aligned} \quad (29)$$

The expression in the parenthesis in the first term can be replaced using the chemical potential equation (17), which leads to:

$$\frac{\partial}{\partial x_j} \left(\frac{\partial \tilde{\phi}^k}{\partial x_i} \frac{\partial \tilde{\phi}^k}{\partial x_j} \right) = -\frac{\partial \tilde{\phi}^k}{\partial x_i} \frac{\tilde{\mu}^k}{Cn^2} + \frac{1}{2} \frac{\partial}{\partial x_i} \left(\frac{\partial \tilde{\phi}^k}{\partial x_j} \frac{\partial \tilde{\phi}^k}{\partial x_j} \right) + \frac{1}{Cn^2} \tilde{\psi}' \frac{\partial \tilde{\phi}^k}{\partial x_i}. \quad (30)$$

Using the product and chain rules we obtain:

$$\begin{aligned} \frac{\partial}{\partial x_j} \left(\frac{\partial \tilde{\phi}^k}{\partial x_i} \frac{\partial \tilde{\phi}^k}{\partial x_j} \right) &= \frac{\tilde{\phi}^k}{Cn^2} \frac{\partial \tilde{\mu}^k}{\partial x_i} - \frac{1}{Cn^2} \frac{\partial}{\partial x_i} \left(\tilde{\mu}^k \tilde{\phi}^k \right) + \frac{1}{2} \frac{\partial}{\partial x_i} \left(\frac{\partial \tilde{\phi}^k}{\partial x_j} \frac{\partial \tilde{\phi}^k}{\partial x_j} \right) + \frac{1}{Cn^2} \frac{\partial \tilde{\psi}}{\partial x_i} \\ &= \frac{\tilde{\phi}^k}{Cn^2} \frac{\partial \tilde{\mu}^k}{\partial x_i} - \frac{\partial}{\partial x_i} \left(\frac{\tilde{\mu}^k \tilde{\phi}^k}{Cn^2} - \frac{1}{2} \frac{\partial \tilde{\phi}^k}{\partial x_j} \frac{\partial \tilde{\phi}^k}{\partial x_j} - \frac{\tilde{\psi}}{Cn^2} \right). \end{aligned} \quad (31)$$

Next we substitute this simplification into the appropriate inner product term in eq. (23):

$$\begin{aligned} \left(\frac{\partial}{\partial x_j} \left(\frac{\partial \tilde{\phi}^k}{\partial x_i} \frac{\partial \tilde{\phi}^k}{\partial x_j} \right), \delta t \tilde{v}_i^k \right) &= \delta t \left(\frac{\tilde{\phi}^k}{Cn^2} \frac{\partial \tilde{\mu}^k}{\partial x_i} - \frac{\partial}{\partial x_i} \left(\frac{\tilde{\mu}^k \tilde{\phi}^k}{Cn^2} - \frac{1}{2} \frac{\partial \tilde{\phi}^k}{\partial x_j} \frac{\partial \tilde{\phi}^k}{\partial x_j} - \frac{\tilde{\psi}}{Cn^2} \right), \tilde{v}_i^k \right) \\ &= \delta t \left(\frac{\tilde{\phi}^k}{Cn^2} \frac{\partial \tilde{\mu}^k}{\partial x_i}, \tilde{v}_i^k \right) - \delta t \left(\frac{\partial}{\partial x_i} \left(\frac{\tilde{\mu}^k \tilde{\phi}^k}{Cn^2} - \frac{1}{2} \frac{\partial \tilde{\phi}^k}{\partial x_j} \frac{\partial \tilde{\phi}^k}{\partial x_j} - \frac{\tilde{\psi}}{Cn^2} \right), \tilde{v}_i^k \right) \\ &= \frac{\delta t}{Cn^2} \left(\tilde{\phi}^k \frac{\partial \tilde{\mu}^k}{\partial x_i}, \tilde{v}_i^k \right) + \delta t \left(\frac{\tilde{\mu}^k \tilde{\phi}^k}{Cn^2} - \frac{1}{2} \frac{\partial \tilde{\phi}^k}{\partial x_j} \frac{\partial \tilde{\phi}^k}{\partial x_j} - \frac{\tilde{\psi}}{Cn^2}, \frac{\partial \tilde{v}_i^k}{\partial x_i} \right). \end{aligned} \quad (32)$$

The last term vanishes due to the solenoidality of the velocity field, eq. (18); and therefore, after multiplying by Cn/We , we achieve the desired result. ■

Corollary 1 (Strong equivalence of forcing). *If we have the following equivalence in the weak sense:*

$$\frac{Cn}{We} \left(\frac{\partial}{\partial x_j} \left(\frac{\partial \tilde{\phi}^k}{\partial x_i} \frac{\partial \tilde{\phi}^k}{\partial x_j} \right), \delta t \tilde{v}_i^k \right) = \frac{\delta t}{We Cn} \left(\tilde{\phi}^k \frac{\partial \tilde{\mu}^k}{\partial x_i}, \tilde{v}_i^k \right), \quad (33)$$

$\forall \tilde{\phi}^k, \tilde{\mu}^k \in H^1(\Omega)$, and $\forall \tilde{\mathbf{v}}^k \in \mathbf{H}_0^1(\Omega)$, where $\tilde{\mathbf{v}}^k, \tilde{\mathbf{v}}^{k+1}, p^k, p^{k+1}, \phi^k, \phi^{k+1}, \mu^k, \mu^{k+1}$ satisfy eq. (19) – eq. (23), then the following equivalence also holds in the strong sense:

$$\frac{Cn}{We} \frac{\partial}{\partial x_j} \left(\frac{\partial \tilde{\phi}^k}{\partial x_i} \frac{\partial \tilde{\phi}^k}{\partial x_j} \right) = \frac{1}{We Cn} \tilde{\phi}^k \frac{\partial \tilde{\mu}^k}{\partial x_i}, \quad (34)$$

if $\tilde{\phi}^k, \tilde{\mu}^k \in H^1(\Omega) \cap C_c^\infty(\Omega)$, and $\tilde{\mathbf{v}}^k \in \mathbf{H}_0^1(\Omega) \cap \mathbf{C}_c^\infty(\Omega)$.

There are numerous papers in the literature which uses the $\tilde{\phi}^k \frac{\partial \tilde{\mu}^k}{\partial x_i}$ as the surface tension forcing [26, 23, 7, 39]. The above corollary shows that the form of stress used in the CHNS model presented in this system is equivalent to the more popular $\tilde{\phi}^k \frac{\partial \tilde{\mu}^k}{\partial x_i}$ in the weak sense.

Remark 5. The advection term in eq. (1) can be defined in the skew-symmetric form as (see lemma 6.10 of section 6.1.2 of [17] for details):

$$B(v_i, v_j) := v_j \frac{\partial v_i}{\partial x_j} + \frac{1}{2} v_i \frac{\partial v_j}{\partial x_j}. \quad (35)$$

Using the solenoidality of the mixture velocity eq. (4) we have that

$$B_1(v_i, v_j) = \rho v_j \frac{\partial v_i}{\partial x_j} \quad \text{and} \quad B_2(v_i, v_j) = J_j \frac{\partial v_i}{\partial x_j}. \quad (36)$$

The skew symmetric form induces a trilinear form when weakened; for three general vectors $u_i, v_i, w_i \in \mathbf{H}_0^1(\Omega)$ we have⁸:

$$b_1(u_i, v_j, w_i) = \left(B_1(v_i, v_j), w_i \right) = \frac{1}{2} \left(v_j \frac{\partial v_i}{\partial x_j}, w_i \right) - \frac{1}{2} \left(v_j \frac{\partial w_i}{\partial x_j}, v_i \right), \quad (37)$$

$$b_2(u_i, J_j, w_i) = \left(B_2(v_i, J_j), w_i \right) = \frac{1}{2} \left(J_j \frac{\partial v_i}{\partial x_j}, w_i \right) - \frac{1}{2} \left(J_j \frac{\partial w_i}{\partial x_j}, v_i \right). \quad (38)$$

Then for our case in the momentum equations, consider the situation where we have $\mathbf{J}, \mathbf{v} \in \mathbf{H}_0^1(\Omega)$, and we are working towards energy estimates, which entails taking an inner product of momentum equation with \mathbf{v} to get an energy functional (to obtain the second order moment). In which case we have for both the non-linear terms in momentum equations:

$$b_1(v_i, v_j, v_i) = \left(B_1(v_i, v_j), v_i \right) = \frac{1}{2} \left(\rho v_j \frac{\partial v_i}{\partial x_j}, v_i \right) - \frac{1}{2} \left(\rho v_j \frac{\partial v_i}{\partial x_j}, v_i \right) = 0, \quad (39)$$

$$b_2(v_i, J_j, v_i) = \left(B_2(v_i, J_j), v_i \right) = \frac{1}{2} \left(J_j \frac{\partial v_i}{\partial x_j}, v_i \right) - \frac{1}{2} \left(J_j \frac{\partial v_i}{\partial x_j}, v_i \right) = 0. \quad (40)$$

This makes physical sense from the point-of-view of energy balance, since the aforementioned non-linear terms do not act as sinks or sources; instead, they provide the mechanism for redistribution of energy to various length scales.

Lemma 2. The variational advection term from the Cahn-Hilliard contribution in the momentum equation, eq. (19), can be written as follows:

$$\begin{aligned} \frac{\delta t}{WeCn} \left(\tilde{\phi}^k \tilde{v}_i^k, \frac{\partial \tilde{\mu}^k}{\partial x_i} \right) &= \frac{1}{2} \int_{\Omega} \left(\rho \left(\phi^{k+1} \right) \|\mathbf{v}^{k+1}\|^2 - \rho \left(\phi^k \right) \|\mathbf{v}^k\|^2 \right) d\mathbf{x} - \frac{\delta t}{Re} \left\| \sqrt{\eta \left(\phi^{k+1} \right)} \nabla \tilde{\mathbf{v}}^k \right\|_{L^2}^2 \\ &\quad - \frac{1}{Fr} \left(y, \rho \left(\phi^{k+1} \right) - \rho \left(\phi^k \right) \right), \end{aligned} \quad (41)$$

$\forall \tilde{\phi}^k, \phi^{k+1}, \tilde{\mu}^k \in H^1(\Omega)$, and $\forall \mathbf{v}^k, \mathbf{v}^{k+1} \in \mathbf{H}_0^1(\Omega)$, where $\mathbf{v}^k, \mathbf{v}^{k+1}, p^k, p^{k+1}, \phi^k, \phi^{k+1}, \mu^k, \mu^{k+1}$ satisfy

⁸Here the subscript 0 for the Sobolev space $\mathbf{H}_0^1(\Omega)$ represents zero velocities on the boundary in the trace sense.

eq. (19) – eq. (23), and

$$\begin{aligned} \|\mathbf{v}\|^2 &:= \sum_i |v_i|^2, \\ \left\| \sqrt{\eta(\phi^{k+1})} \nabla \tilde{\mathbf{v}}^k \right\|_{L^2}^2 &:= \int_{\Omega} \sqrt{\eta(\phi^{k+1})} \sum_i \sum_j \left| \frac{\partial \tilde{v}_i^k}{\partial x_j} \right|^2 d\mathbf{x} = \int_{\Omega} \sqrt{\eta(\phi^{k+1})} \|\nabla \mathbf{v}\|_F^2 d\mathbf{x}. \end{aligned} \quad (42)$$

Proof. We start by taking the L^2 inner product of momentum equation (19) with $\delta t \tilde{v}_i^k$:

$$\begin{aligned} &\left(\rho(\phi^{k+1}) \frac{(v_i^{k+1} - v_i^k)}{\delta t}, \delta t \tilde{v}_i^k \right) + \left(\rho(\phi^{k+1}) \tilde{v}_j^k \frac{\partial \tilde{v}_i^k}{\partial x_j}, \delta t \tilde{v}_i^k \right) \\ &\quad + \frac{1}{Pe} \left(\tilde{J}_j^k \frac{\partial \tilde{v}_i^k}{\partial x_j}, \delta t \tilde{v}_i^k \right) + \frac{Cn}{We} \left(\frac{\partial}{\partial x_j} \left(\frac{\partial \tilde{\phi}^k}{\partial x_i} \frac{\partial \tilde{\phi}^k}{\partial x_j} \right), \delta t \tilde{v}_i^k \right) \\ &\quad + \frac{1}{We} \left(\frac{\partial \tilde{p}^k}{\partial x_i}, \delta t \tilde{v}_i^k \right) - \frac{1}{Re} \left(\frac{\partial}{\partial x_j} \left(\eta(\phi^{k+1}) \frac{\partial \tilde{v}_i^k}{\partial x_j} \right), \delta t \tilde{v}_i^k \right) \\ &\quad - \frac{1}{Fr} \left(\rho(\phi^{k+1}) \hat{g}_i, \delta t \tilde{v}_i^k \right) = 0. \end{aligned} \quad (43)$$

Notice that the second and third terms are in a trilinear form so from eq. (39) and eq. (40) they go to zero and we have:

$$\begin{aligned} &\left(\rho(\phi^{k+1}) (v_i^{k+1} - v_i^k), \tilde{v}_i^k \right) + \frac{Cn}{We} \left(\frac{\partial}{\partial x_j} \left(\frac{\partial \tilde{\phi}^k}{\partial x_i} \frac{\partial \tilde{\phi}^k}{\partial x_j} \right), \delta t \tilde{v}_i^k \right) \\ &\quad + \frac{1}{We} \left(\frac{\partial \tilde{p}^k}{\partial x_i}, \delta t \tilde{v}_i^k \right) - \frac{1}{Re} \left(\frac{\partial}{\partial x_k} \left(\eta(\phi^{k+1}) \frac{\partial \tilde{v}_i^k}{\partial x_k} \right), \delta t \tilde{v}_i^k \right) \\ &\quad - \frac{1}{Fr} \left(\hat{g}_i, \delta t \rho(\phi^{k+1}) \tilde{v}_i^k \right) = 0, \\ \Rightarrow &\frac{1}{2} \int_{\Omega} \left(\rho(\phi^{k+1}) \|\mathbf{v}^{k+1}\|^2 - \rho(\phi^k) \|\mathbf{v}^k\|^2 \right) d\mathbf{x} \\ &\quad + \frac{Cn}{We} \left(\frac{\partial}{\partial x_j} \left(\frac{\partial \tilde{\phi}^k}{\partial x_i} \frac{\partial \tilde{\phi}^k}{\partial x_j} \right), \delta t \tilde{v}_i^k \right) \\ &\quad + \frac{1}{We} \left(\frac{\partial \tilde{p}^k}{\partial x_i}, \delta t \tilde{v}_i^k \right) - \frac{1}{Re} \left(\frac{\partial}{\partial x_j} \left(\eta(\phi^{k+1}) \frac{\partial \tilde{v}_i^k}{\partial x_j} \right), \delta t \tilde{v}_i^k \right) \\ &\quad - \frac{1}{Fr} \left(\hat{g}_i, \delta t \rho(\phi^{k+1}) \tilde{v}_i^k \right) = 0, \end{aligned} \quad (44)$$

where we made use of the fact that $\tilde{v}_i^k = (v_i^{k+1} + v_i^k)/2$ and lemma 8 from Appendix A. We can now use solenoidality of the velocity field to get rid of the pressure term. We can do this by weakening

the pressure term:

$$\begin{aligned} & \frac{1}{2} \int_{\Omega} \left(\rho \left(\phi^{k+1} \right) \left\| \mathbf{v}^{k+1} \right\|^2 - \rho \left(\phi^k \right) \left\| \mathbf{v}^k \right\|^2 \right) d\mathbf{x} + \frac{Cn}{We} \left(\frac{\partial}{\partial x_j} \left(\frac{\partial \tilde{\phi}^k}{\partial x_i} \frac{\partial \tilde{\phi}^k}{\partial x_j} \right), \delta t \tilde{v}_i^k \right) \\ & - \frac{\delta t}{We} \left(\tilde{p}^k, \frac{\partial \tilde{v}_i^k}{\partial x_i} \right) - \frac{1}{Re} \left(\frac{\partial}{\partial x_j} \left(\eta \left(\phi^{k+1} \right) \frac{\partial \tilde{v}_i^k}{\partial x_j} \right), \delta t \tilde{v}_i^k \right) \\ & - \frac{1}{Fr} \left(\hat{g}_i, \delta t \rho \left(\phi^{k+1} \right) \tilde{v}_i^k \right) = 0, \end{aligned} \quad (46)$$

$$\begin{aligned} \Rightarrow & \frac{1}{2} \int_{\Omega} \left(\rho \left(\phi^{k+1} \right) \left\| \mathbf{v}^{k+1} \right\|^2 - \rho \left(\phi^k \right) \left\| \mathbf{v}^k \right\|^2 \right) d\mathbf{x} + \frac{Cn}{We} \left(\frac{\partial}{\partial x_j} \left(\frac{\partial \tilde{\phi}^k}{\partial x_i} \frac{\partial \tilde{\phi}^k}{\partial x_j} \right), \delta t \tilde{v}_i^k \right) \\ & - \frac{1}{Re} \left(\frac{\partial}{\partial x_j} \left(\eta \left(\phi^{k+1} \right) \frac{\partial \tilde{v}_i^k}{\partial x_j} \right), \delta t \tilde{v}_i^k \right) - \frac{1}{Fr} \left(\hat{g}_i, \delta t \rho \left(\phi^{k+1} \right) \tilde{v}_i^k \right) = 0, \end{aligned} \quad (47)$$

$$\begin{aligned} \Rightarrow & \frac{1}{2} \int_{\Omega} \left(\rho \left(\phi^{k+1} \right) \left\| \mathbf{v}^{k+1} \right\|^2 - \rho \left(\phi^k \right) \left\| \mathbf{v}^k \right\|^2 \right) d\mathbf{x} + \frac{Cn}{We} \left(\frac{\partial}{\partial x_j} \left(\frac{\partial \tilde{\phi}^k}{\partial x_i} \frac{\partial \tilde{\phi}^k}{\partial x_j} \right), \delta t \tilde{v}_i^k \right) \\ & + \frac{\delta t}{Re} \left(\left(\sqrt{\eta \left(\phi^{k+1} \right)} \frac{\partial \tilde{v}_i^k}{\partial x_j} \right), \left(\sqrt{\eta \left(\phi^{k+1} \right)} \frac{\partial \tilde{v}_i^k}{\partial x_j} \right) \right) - \frac{1}{Fr} \left(\hat{g}_i, \delta t \rho \left(\phi^{k+1} \right) \tilde{v}_i^k \right) = 0, \end{aligned} \quad (48)$$

$$\begin{aligned} \Rightarrow & \frac{1}{2} \int_{\Omega} \left(\rho \left(\phi^{k+1} \right) \left\| \mathbf{v}^{k+1} \right\|^2 - \rho \left(\phi^k \right) \left\| \mathbf{v}^k \right\|^2 \right) d\mathbf{x} + \frac{Cn}{We} \left(\frac{\partial}{\partial x_j} \left(\frac{\partial \tilde{\phi}^k}{\partial x_i} \frac{\partial \tilde{\phi}^k}{\partial x_j} \right), \delta t \tilde{v}_i^k \right) \\ & + \frac{\delta t}{Re} \left\| \sqrt{\eta \left(\phi^{k+1} \right)} \nabla \tilde{\mathbf{v}}^k \right\|_{L^2}^2 - \frac{1}{Fr} \left(\hat{g}_i, \delta t \rho \left(\phi^{k+1} \right) \tilde{v}_i^k \right) = 0. \end{aligned} \quad (49)$$

Next we invoke lemma 1 and write eq. (49) as:

$$\begin{aligned} & \frac{1}{2} \int_{\Omega} \left(\rho \left(\phi^{k+1} \right) \left\| \mathbf{v}^{k+1} \right\|^2 - \rho \left(\phi^k \right) \left\| \mathbf{v}^k \right\|^2 \right) d\mathbf{x} + \frac{\delta t}{WeCn} \left(\tilde{\phi}^k \tilde{v}_i^k, \frac{\partial \tilde{\mu}^k}{\partial x_i} \right) + \frac{\delta t}{Re} \left\| \sqrt{\eta \left(\phi^{k+1} \right)} \nabla \tilde{\mathbf{v}}^k \right\|_{L^2}^2 \\ & - \frac{1}{Fr} \left(\hat{g}_i, \delta t \rho \left(\phi^{k+1} \right) \tilde{v}_i^k \right) = 0. \end{aligned} \quad (50)$$

Next we simplify the gravity term. Notice that

$$-\frac{1}{Fr} \left(\hat{g}_i, \delta t \rho \left(\phi^{k+1} \right) \tilde{v}_i^k \right) = -\frac{1}{Fr} \left(\frac{\partial (-y)}{\partial x_i}, \delta t \rho \left(\phi^{k+1} \right) \tilde{v}_i^k \right) = -\frac{1}{Fr} \left(y, \delta t \frac{\partial \left(\rho \left(\phi^{k+1} \right) \tilde{v}_i^k \right)}{\partial x_i} \right), \quad (51)$$

where $y = x_2$ and $\hat{\mathbf{g}} = (0, -1, 0)$. Here we invoke that $\tilde{\mathbf{v}}^{k+1} \in \mathbf{H}_0^1(\Omega)$ so the boundary terms go to zero while doing integration by parts. Let $C_1 = \frac{(\rho_- - \rho_+)}{2} m(\phi)$, then using the continuity equation,

eq. (4), and the definition of J_i we obtain:

$$\begin{aligned}
\frac{1}{Fr} \left(y, \delta t \frac{\partial \left(\rho(\phi^{k+1}) \tilde{v}_i^k \right)}{\partial x_i} \right) &= -\frac{1}{Fr} \left(y, \rho(\phi^{k+1}) - \rho(\phi^k) \right) - \frac{\delta t C_1}{Fr Pe} \left(y, \frac{\partial}{\partial x_i} \left(\frac{\partial \tilde{\mu}^k}{\partial x_i} \right) \right) \\
&= -\frac{1}{Fr} \left(y, \rho(\phi^{k+1}) - \rho(\phi^k) \right) + \frac{\delta t C_1}{Fr Pe} \left(\frac{\partial y}{\partial x_i}, \frac{\partial \tilde{\mu}^k}{\partial x_i} \right) \\
&= -\frac{1}{Fr} \left(y, \rho(\phi^{k+1}) - \rho(\phi^k) \right) - \frac{\delta t C_1}{Fr Pe} \left(\frac{\partial}{\partial x_i} \left(\frac{\partial y}{\partial x_i} \right), \tilde{\mu}^k \right) + \frac{\delta t C_1}{Fr Pe} \int_{\partial\Omega} \tilde{\mu}^k \left(\frac{\partial y}{\partial x_i} \right) \hat{n}_i d\mathbf{x} \\
&= -\frac{1}{Fr} \left(y, \rho(\phi^{k+1}) - \rho(\phi^k) \right) - \frac{\delta t C_1}{Fr Pe} \left(\frac{\partial}{\partial x_i} \left(\frac{\partial y}{\partial x_i} \right), \tilde{\mu}^k \right) + \frac{\delta t C_1}{Fr Pe} \int_{\partial\Omega} \tilde{\mu}^k \hat{g}_i \hat{n}_i d\mathbf{x},
\end{aligned} \tag{52}$$

where \hat{n}_i is outward pointing normal to the boundary of the domain Ω .

Remark 6. We will assume that

$$\frac{\delta t C_1}{Fr Pe} \int_{\partial\Omega} \tilde{\mu}^k \hat{g}_i \hat{n}_i d\mathbf{x} = 0, \tag{53}$$

which is true as long as there is no three-phase contact line on any boundary on which $\hat{n}_i \hat{g}_i$ is non-zero.

Under the above assumption we can write

$$-\frac{1}{Fr} \left(\hat{g}_i, \delta t \rho(\phi^{k+1}) \tilde{v}_i^k \right) = -\frac{1}{Fr} \left(y, \delta t \frac{\partial \left(\rho(\phi^{k+1}) \tilde{v}_i^k \right)}{\partial x_i} \right) = \frac{1}{Fr} \left(y, \rho(\phi^{k+1}) - \rho(\phi^k) \right). \tag{54}$$

Combining this last result with eq. (50) yields the desired result:

$$\begin{aligned}
\frac{1}{2} \int_{\Omega} \left(\rho(\phi^{k+1}) \|\mathbf{v}^{k+1}\|^2 - \rho(\phi^k) \|\mathbf{v}^k\|^2 \right) d\mathbf{x} &+ \frac{\delta t}{We Cn} \left(\tilde{\phi}^k \tilde{v}_i^k, \frac{\partial \tilde{\mu}^k}{\partial x_i} \right) + \frac{\delta t}{Re} \left\| \sqrt{\eta(\phi^{k+1})} \nabla \mathbf{v} \right\|_{L^2}^2 \\
&+ \frac{1}{Fr} \left(y, \rho(\phi^{k+1}) - \rho(\phi^k) \right) = 0.
\end{aligned} \tag{55}$$

■

Proposition 2. The following identity holds:

$$\left(\psi'(\tilde{\phi}^k), \phi^{k+1} - \phi^k \right) = \left(\psi(\phi^{k+1}) - \psi(\phi^k), 1 \right) - \left(\frac{\psi'''(\lambda)}{24}, (\phi^{k+1} - \phi^k)^3 \right), \tag{56}$$

for some λ between ϕ^k and ϕ^{k+1} .

Proof. Recall that $\tilde{\phi}^k = (\phi^{k+1} + \phi^k)/2$. From Taylor series we note the following:

$$\psi' \left(\frac{\phi^{k+1} + \phi^k}{2} \right) - \frac{\psi(\phi^{k+1}) - \psi(\phi^k)}{\phi^{k+1} - \phi^k} = -\frac{\psi'''(\lambda)}{24} (\phi^{k+1} - \phi^k)^2,$$

for some λ between ϕ^k and ϕ^{k+1} . Computing the inner product of this expression with $\phi^{k+1} - \phi^k$ and slightly re-arranging yields the desired result. ■

Claim 1 (Estimate of the correction). *The following estimate holds:*

$$\left| \left(\frac{\psi'''(\lambda)}{24}, (\phi^{k+1} - \phi^k)^3 \right) \right| \leq C_m L^3 \delta t^3 \left\| \frac{\psi'''(\lambda)}{24} \right\|_{L^\infty(\Omega)}, \quad (57)$$

where L is a Lipschitz constant and C_m is the volume of the physical domain:

$$|\phi^{k+1} - \phi^k| \leq L \delta t \quad \text{and} \quad C_m := \int_{\Omega} d\mathbf{x}.$$

Proof. We start with the error term in proposition 2 and obtain the following upper bound:

$$\begin{aligned} \left| \left(\frac{\psi'''(\lambda)}{24}, (\phi^{k+1} - \phi^k)^3 \right) \right| &= \left| \int_{\Omega} \frac{\psi'''(\lambda)}{24} (\phi^{k+1} - \phi^k)^3 d\mathbf{x} \right| \\ &\leq \left\| \frac{\psi'''(\lambda)}{24} \right\|_{L^\infty(\Omega)} \int_{\Omega} |\phi^{k+1} - \phi^k|^3 d\mathbf{x}. \end{aligned} \quad (58)$$

Using the Lipschitz continuity of ϕ we arrive at the desired result: eq. (57). ■

We are now in a position to prove energy stability. The argument we present here is based on the fact that the energy functional given by eq. (9) is decreasing as the discrete solution is evolving in time. This represents the strict adherence to the second law of thermodynamics at the semi-discrete level. Therefore, if the difference between the energy functional between two time steps is negative, then we have achieved energy stability. We prove energy stability in the following theorem.

Theorem 1 (Energy stability). *The time discretization of the Cahn-Hilliard Navier-Stokes (CHNS) equations as described by eq. (19) – eq. (23) is energy stable and satisfies the following energy law:*

$$\begin{aligned} E_{tot}(\mathbf{v}^{k+1}, \phi^{k+1}) - E_{tot}(\mathbf{v}^k, \phi^k) &= \frac{-\delta t}{Re} \left\| \sqrt{\eta(\phi^{k+1})} \tilde{\mathbf{v}}^k \right\|_{L^2}^2 - \frac{\delta t}{Pe Cn^2 We} \left\| \nabla \tilde{\mu}^k \right\|_{L^2}^2 \\ &\quad + \frac{1}{We Cn} \left(\frac{\psi'''(\lambda)}{24}, (\phi^{k+1} - \phi^k)^3 \right), \end{aligned} \quad (59)$$

provided the following time-step restriction is observed:

$$0 \leq \delta t \leq \left(\frac{\frac{1}{Re} \left(\left\| \sqrt{\eta(\phi^{k+1})} \nabla \tilde{\mathbf{v}}^k \right\|_{L^2}^2 \right) + \frac{1}{Pe Cn^2 We} \left\| \nabla \tilde{\mu}^k \right\|_{L^2}^2}{\frac{C_m L^3}{We Cn} \left\| \frac{\psi'''(\lambda)}{24} \right\|_{L^\infty(\Omega)}} \right)^{\frac{1}{2}}. \quad (60)$$

where,

$$E_{tot}(\mathbf{v}^k, \phi^k) = \int_{\Omega} \frac{1}{2} \rho(\phi^k) \|\mathbf{v}^k\|^2 d\mathbf{x} + \frac{1}{Cn We} \int_{\Omega} \left(\psi(\phi^k) + \frac{Cn^2}{2} \|\nabla \phi^k\|^2 + \frac{1}{Fr} \rho(\phi^k) y \right) d\mathbf{x}. \quad (61)$$

Proof. We begin with taking the L^2 inner product of eq. (18) with $\delta t \tilde{\mu}^k$:

$$\left(\phi^{k+1} - \phi^k, \tilde{\mu}^k \right) = - \left(\frac{\partial \left(\tilde{v}_i^k \tilde{\phi}^k \right)}{\partial x_i}, \delta t \tilde{\mu}^k \right) + \frac{\delta t}{PeCn} \left(\frac{\partial}{\partial x_i} \left(\frac{\partial \tilde{\mu}^k}{\partial x_i} \right), \tilde{\mu}^k \right), \quad (62)$$

and integrate-by-parts on the right-hand side:

$$\left(\phi^{k+1} - \phi^k, \tilde{\mu}^k \right) = \left(\tilde{v}_i^k \tilde{\phi}^k, \delta t \frac{\partial \tilde{\mu}^k}{\partial x_i} \right) - \frac{\delta t}{PeCn} \left\| \nabla \tilde{\mu}^k \right\|_{L^2}^2. \quad (63)$$

We now work with the μ equation by taking the L^2 inner product of eq. (17) with $\phi^{k+1} - \phi^k$:

$$\left(\tilde{\mu}^k, \phi^{k+1} - \phi^k \right) = \left(\tilde{\psi}', \phi^{k+1} - \phi^k \right) - Cn^2 \left(\frac{\partial}{\partial x_i} \left(\frac{\partial \tilde{\phi}^k}{\partial x_i} \right), \phi^{k+1} - \phi^k \right), \quad (64)$$

where $\tilde{\psi}'$ is defined by eq. (12), and integrate-by-parts on the last term:

$$\left(\tilde{\mu}^k, \phi^{k+1} - \phi^k \right) = \left(\tilde{\psi}', \phi^{k+1} - \phi^k \right) + \frac{Cn^2}{2} \left(\left\| \nabla \phi^{k+1} \right\|_{L^2}^2 - \left\| \nabla \phi^k \right\|_{L^2}^2 \right), \quad (65)$$

where we also used the fact that $\tilde{\phi}^k = (\phi^{k+1} + \phi^k)/2$. The first term on right-hand side of eq. (65) can be simplified further using proposition 2:

$$\begin{aligned} \left(\tilde{\mu}^k, \phi^{k+1} - \phi^k \right) &= \left(\psi(\phi^{k+1}) - \psi(\phi^k), 1 \right) - \left(\frac{\psi'''(\lambda)}{24}, (\phi^{k+1} - \phi^k)^3 \right) \\ &\quad + \frac{Cn^2}{2} \left(\left\| \nabla \phi^{k+1} \right\|_{L^2}^2 - \left\| \nabla \phi^k \right\|_{L^2}^2 \right). \end{aligned} \quad (66)$$

Now, combining eq. (66) and eq. (63) we have:

$$\begin{aligned} &\left(\psi(\phi^{k+1}) - \psi(\phi^k), 1 \right) - \left(\frac{\psi'''(\lambda)}{24}, (\phi^{k+1} - \phi^k)^3 \right) + \frac{Cn^2}{2} \left(\left\| \nabla \phi^{k+1} \right\|_{L^2}^2 - \left\| \nabla \phi^k \right\|_{L^2}^2 \right) \\ &= \left(\tilde{v}_i^k \tilde{\phi}^k, \delta t \frac{\partial \tilde{\mu}^k}{\partial x_i} \right) - \frac{\delta t}{PeCn} \left\| \nabla \tilde{\mu}^k \right\|_{L^2}^2. \end{aligned} \quad (67)$$

Next we divide eq. (67) by $WeCn$ and from lemma 2 we can replace the first term on the right-hand side by eq. (41):

$$\begin{aligned} &\frac{1}{2} \int_{\Omega} \left(\rho(\phi^{k+1}) \left\| \mathbf{v}^{k+1} \right\|^2 - \rho(\phi^k) \left\| \mathbf{v}^k \right\|^2 \right) d\mathbf{x} + \frac{\delta t}{Re} \left(\left\| \sqrt{\eta(\phi^{k+1})} \nabla \tilde{\mathbf{v}}^k \right\|_{L^2}^2 \right) \\ &\quad + \frac{1}{WeCn} \left(\psi(\phi^{k+1}) - \psi(\phi^k), 1 \right) - \frac{1}{WeCn} \left(\frac{\psi'''(\lambda)}{24}, (\phi^{k+1} - \phi^k)^3 \right) \\ &\quad + \frac{Cn}{2We} \left(\left\| \nabla \phi^{k+1} \right\|_{L^2}^2 - \left\| \nabla \phi^k \right\|_{L^2}^2 \right) + \frac{\delta t}{PeCn^2 We} \left\| \nabla \tilde{\mu}^k \right\|_{L^2}^2 \\ &\quad + \frac{1}{Fr} \left(y, \rho(\phi^{k+1}) - \rho(\phi^k) \right) = 0. \end{aligned} \quad (68)$$

Simplifying and using the definition of the energy functional, eq. (9), we obtain the energy law:

$$E_{\text{tot}}(\mathbf{v}^{k+1}, \phi^{k+1}) - E_{\text{tot}}(\mathbf{v}^k, \phi^k) = \frac{-\delta t}{Re} \left\| \sqrt{\eta(\phi^{k+1})} \nabla \tilde{\mathbf{v}}^k \right\|_{L^2}^2 - \frac{\delta t}{PeCn^2We} \|\nabla \tilde{\mu}^k\|_{L^2}^2 + \frac{1}{WeCn} \left(\frac{\psi'''(\lambda)}{24}, (\phi^{k+1} - \phi^k)^3 \right). \quad (69)$$

In order for this energy to be non-increasing in forward time, we require the following:

$$\frac{\delta t}{Re} \left\| \sqrt{\eta(\phi^{k+1})} \nabla \tilde{\mathbf{v}}^k \right\|_{L^2}^2 + \frac{\delta t}{PeCn^2We} \|\nabla \tilde{\mu}^k\|_{L^2}^2 \geq \frac{1}{WeCn} \left(\frac{\psi'''(\lambda)}{24}, (\phi^{k+1} - \phi^k)^3 \right). \quad (70)$$

Using the estimate from claim 1 we can guarantee this inequality provided that:

$$\frac{\delta t}{Re} \left\| \sqrt{\eta(\phi^{k+1})} \nabla \tilde{\mathbf{v}}^k \right\|_{L^2}^2 + \frac{\delta t}{PeCn^2We} \|\nabla \tilde{\mu}^k\|_{L^2}^2 \geq \frac{1}{WeCn} \left\| \frac{\psi'''(\lambda)}{24} \right\|_{L^\infty(\Omega)} C_m L^3 \delta t^3. \quad (71)$$

This condition can be turned into a condition on the maximum energy-stable time-step:

$$0 \leq \delta t \leq \left(\frac{\frac{1}{Re} \left\| \sqrt{\eta(\phi^{k+1})} \nabla \tilde{\mathbf{v}}^k \right\|_{L^2}^2 + \frac{1}{PeCn^2We} \|\nabla \tilde{\mu}^k\|_{L^2}^2}{\frac{C_m L^3}{WeCn} \left\| \frac{\psi'''(\lambda)}{24} \right\|_{L^\infty(\Omega)}} \right)^{\frac{1}{2}}, \quad (72)$$

which proves the theorem. ■

Remark 7. It is important to note that condition eq. (72) is a very weak condition (satisfied for most δt), as all the quantities in the condition are order one quantities. The bounds presented for $\left(\frac{\psi'''(\lambda)}{24}, (\phi^{k+1} - \phi^k)^3 \right)$ are the absolute worst case scenarios, which in practice would only rarely be achieved. Therefore, though we cannot claim unconditional stability for the scheme, we can say that the scheme is energy stable for large range of δt values and allows us to take large time steps. It is common practice in the literature to approximate the free energy functional such that it has a form which will not result in the cubic term in eq. (56) (see [40, 24, 25] for examples), which results in an unconditionally stable scheme. In the estimate we have presented we do not make any approximations on the form of free energy functional, which results in a slightly tighter restriction on the time step restriction.

3.3. Solvability of the discrete-in-time, continuous-in-space CHNS system

In this subsection we establish the solvability of system of equations eq. (19) – eq. (23). We follow the basic strategy used by Han and Wang [23], which, after adaptation to the specific Cahn-Hilliard Navier-Stokes system considered in this work, can be summarized as follows:

- Show that eq. (22) has the following property: given $\tilde{\mu}^k$, then $\tilde{\phi}^k$ is uniquely determined;
- Show that eq. (19) – eq. (21) have the following property: given $\tilde{\mu}^k$, and hence ϕ^{k+1} from eq. (22) as stated above, then $\tilde{\mathbf{v}}^k$ and \tilde{p}^k are uniquely determined;
- This establishes $\tilde{\phi}^k$, $\tilde{\mathbf{v}}^k$, and \tilde{p}^k as uniquely determined by $\tilde{\mu}^k$; with this knowledge in hand, we can now view the remaining equation, eq. (23), as a scalar equation for $\tilde{\mu}^k$;

- Show that there exists a solution, $\tilde{\mu}^k$, to eq. (23), with $\tilde{\phi}^k$ and $\tilde{\mathbf{v}}^k$ understood to be functions of $\tilde{\mu}^k$ via eq. (19) – eq. (22).

The key to the above argumentation is the Browder-Minty theorem (e.g., see theorem 9.14 Ciarlet [41]) and the main theorem on pseudo-monotone operators due to Brezis (see theorem 27.A Zeidler [42]), both of which we reproduce below for completeness.

Theorem 2. (Browder-Minty (1963)) *Let X be a real, reflexive, Banach space and let $T : X \longrightarrow X^*$ be a monotone, coercive, continuous, and bounded operator, then for any $b \in X^*$, there exists a solution to*

$$T(u) = b. \quad (73)$$

further, if $T : X \longrightarrow X^$ is strictly monotone, then the solution u is unique*

Theorem 3. (Brezis (1968)) *Let X be a real, reflexive, Banach space and let $T : X \longrightarrow X^*$ be a pseudo-monotone, coercive, continuous, and bounded operator, then for any $b \in X^*$, there exists a solution to*

$$T(u) = b. \quad (74)$$

Lemma 3 (Solvability of (22)). *Given $\tilde{\mu}^k \in H^1(\Omega)$ and $\phi^k \in H^1(\Omega)$, there exists a unique solution $\tilde{\phi}^k \in H^1(\Omega)$ to eq. (22). This establishes the solution operator:*

$$\tilde{\phi}^k(\tilde{\mu}^k) : \tilde{\mu}^k \mapsto \tilde{\phi}^k.$$

Proof of the above lemma follows from theorem 2, where the continuity and boundedness of the solution operator follows from the fact that eq. (22) is an elliptic semi-linear equation. The detailed proof is omitted here for brevity.

Lemma 4 (Solvability of (19) – (21)). *Given $\tilde{\mu}^k \in H^1(\Omega)$, $\mathbf{v}^k \in \mathbf{H}_0^1(\Omega)$, and $\phi^k \in H^1(\Omega)$, there exists a unique solution $\tilde{\mathbf{v}}^k \in \mathbf{H}_0^1(\Omega)$ and $\tilde{p}^k \in H^1(\Omega)$ to eq. (19) – eq. (21). This establishes the solution operator:*

$$\tilde{\mathbf{v}}^k(\tilde{\mu}^k) : \tilde{\mu}^k \mapsto \tilde{\mathbf{v}}^k.$$

Proof of this lemma follows from the generalized Lax-Milgram theorem under a suitable inf-sup condition. We again omit the details of this proof for brevity, and instead refer the interested reader to Volker [17] for a detailed explanation.

Remark 8. *In the fully discrete setting one needs to satisfy the discrete inf-sup condition (which is a modified coercivity condition) to prove uniqueness for the fully discrete analog of eq. (22). However, we use the variational multi-scale technique, described below in section 3.4, which circumvents the need of a discrete inf-sup condition. The variational multi-scale technique allows for the use of classical Lax-Milgram to prove uniqueness as one can prove classical definition of coercivity directly in this case.*

We now prove solvability for the full time-discretized Cahn-Hilliard Navier-Stokes system by showing that eq. (23) has a solution, $\tilde{\mu}^k$, with ϕ^{k+1} and $\tilde{\mathbf{v}}^k$ understood to be functions of $\tilde{\mu}^k$ via eq. (19) – eq. (22). We aim to show that all the conditions of theorem 3 are satisfied; theorem 3 is a generalization of theorem 2 for operators that are a summation of a higher order monotone operator and a strongly continuous lower order operator. To this end, it is important to note that proving strong continuity for our lower order operators in eq. (23) is difficult. However, Liu [43] showed an equivalent condition called local monotonicity which is easier to prove.

Lemma 5. Given an operator $A : X \longrightarrow X^*$, where X is a real, reflexive Banach space, i.e. $H^1(\Omega)$ in our case. If A has the following properties:

(H1) (Hemicontinuity) The map $t \mapsto \langle A(\xi_1 + t \xi_2), q \rangle$ is continuous on \mathbb{R} ;

(H2) (Local monotonicity) The following inequality holds:

$$\langle A(\xi_1) + A(\xi_2), \xi_1 - \xi_2 \rangle_{H^1(\Omega)} \leq (C + v(\xi_1) + \gamma(\xi_2)) \|\xi_1 - \xi_2\|_{H^1(\Omega)}^2, \quad (75)$$

where $v(\xi_1)$ and $\gamma(\xi_2)$ are bounded, measurable functions in $H^1(\Omega)$;

then A is pseudo-monotone operator.

Liu [43] proves lemma 5 in a more general setting for Banach spaces which are compactly embedded in Hilbert spaces.

Definition 2. Consider the following shorthand notation:

$$\mu := \bar{\mu}^k, \quad \phi(\mu) := \bar{\phi}^k(\bar{\mu}^k), \quad \text{and} \quad v_i(\mu) := \bar{v}_i^k(\bar{\mu}^k). \quad (76)$$

Then, given $\phi^k \in H^1(\Omega)$, from eq. (23) we establish the following solution operator:

$$\langle T(\mu), q \rangle := 2 \left(\phi(\mu) - \phi^k, q \right) - \frac{\delta t}{2} \left(v_i(\mu) \phi(\mu), \frac{\partial q}{\partial x_i} \right) + \frac{\delta t}{PeCn} \left(\frac{\partial \mu}{\partial x_i}, \frac{\partial q}{\partial x_i} \right), \quad (77)$$

for all $q \in H^1(\Omega)$.

Lemma 6. If we assume the solution operator $\phi(\mu)$ to be Lipschitz in μ , then the first term from the operator in definition 2, i.e., $2(\phi(\mu) - \phi^k, q)$ satisfies (H1) and (H2) from lemma 5 and is therefore pseudo-monotone.

Proof. (H1) follows from the continuity of the solution operator from lemma 3. We proceed to check local monotonicity. Using the Lipschitz continuity of ϕ and standard inequality, one can show that

$$\begin{aligned} 2(\phi(\xi_1) - \phi(\xi_2), \xi_1 - \xi_2) &\leq 2L^2 \|\xi_1 - \xi_2\|_{H^1}^2 \left[\|\phi(\xi_1)\|_{L^4}^4 + \|\phi(\xi_2)\|_{L^4}^4 \right. \\ &\quad + 2\|\phi(\xi_1)\|_{L^6}^3 \|\phi(\xi_2)\|_{L^2} + 3\|\phi(\xi_1)\|_{L^4}^2 \|\phi(\xi_2)\|_{L^4}^2 \\ &\quad \left. + 2\|\phi(\xi_2)\|_{L^6}^3 \|\phi(\xi_1)\|_{L^2} + \frac{1}{2}(1 + Cn^2) \right], \end{aligned} \quad (78)$$

where L is the Lipschitz constant for ϕ . This proves local monotonicity (H2). In the interest of brevity we do not provide the detailed steps here. We refer interested readers to Liu [43] which presents similar estimates. ■

Lemma 7. If we assume the solution operators $\phi(\mu)$ and $\mathbf{v}(\mu)$ to be Lipschitz in μ , then the second term from the operator in definition 2, i.e., $\frac{\delta t}{2} \left(v_i(\mu) \phi(\mu), \frac{\partial q}{\partial x_i} \right)$ satisfies (H1) and (H2) from lemma 5 and is therefore pseudo-monotone.

Proof. (H1) follows from the continuity of the solution operators from lemma 3 and lemma 4. We proceed to check local monotonicity. Using Lipschitz continuity and standard inequalities one can show that

$$\left(v_i(\xi_1) \phi(\xi_1) - v_i(\xi_2) \phi(\xi_2), \frac{\partial(\xi_1 - \xi_2)}{\partial x_i} \right) \leq L \|(\xi_1 - \xi_2)\|_{H^1}^2 \left[\|\mathbf{v}(\xi_1)\|_{L^\infty} + \|\phi(\xi_2)\|_{L^\infty} \right], \quad (79)$$

where L is the maximum Lipschitz constant for ϕ and \mathbf{v} . This proves local monotonicity (H2). ■

Theorem 4 (Solvability of (23)). *Given $\phi^k \in H^1(\Omega)$, there exists a solution, $\mu \in H^1(\Omega)$, to eq. (23) in the sense of the solution operator defined in definition 2 that satisfies the conditions of the existence theorem of pseudo-monotone operators (see theorem 3 above).*

Proof. We now proceed by proving that $T(\mu)$ satisfies the conditions of the Browder-Minty theorem.

1. **Continuous and bounded.** We compute the absolute value of eq. (77) and use standard inequalities:

$$\begin{aligned} |\langle T(\mu), q \rangle| &\leq C_1 \|q\|_{L^2} \left(\|\phi(\mu)\|_{L^2} + \|\phi^k\|_{L^2} \right) \\ &\quad + C_2 \delta t \|\nabla q\|_{L^2} \|\mathbf{v}(\mu)\|_{L^2} \|\phi(\mu)\|_{L^2} + \frac{C_3 \delta t}{PeCn} \|\nabla q\|_{L^2} \|\nabla \mu\|_{L^2}. \end{aligned} \quad (80)$$

Using the fact that $\|\cdot\|_{L^2} \leq \|\cdot\|_{H^1}$ and combining all the constants yields:

$$|\langle T(\mu), q \rangle| \leq C(\delta t) \|q\|_{H^1} \left[\|\phi^k\|_{L^2} + (1 + \|\mathbf{v}(\mu)\|_{L^2}) \|\phi(\mu)\|_{L^2} + \|\nabla \mu\|_{L^2} \right]. \quad (81)$$

Therefore, operator T is bounded as a consequence of the boundedness of $\phi(\mu)$ and $\mathbf{v}(\mu)$ from lemma 3 and lemma 4, respectively. Continuity of T follows from a similar argument.

2. **Pseudo-monotonicity.** We begin with the following expression:

$$\begin{aligned} \langle T(\xi_1) - T(\xi_2), \xi_1 - \xi_2 \rangle &= 2 \left(\phi(\xi_1) - \phi(\xi_2), \xi_1 - \xi_2 \right) \\ &\quad - \frac{\delta t}{2} \left(\mathbf{v}(\xi_1) \phi(\xi_1) - \mathbf{v}(\xi_2) \phi(\xi_2), \nabla(\xi_1 - \xi_2) \right) \\ &\quad + \frac{\delta t}{PeCn} \|\nabla(\xi_1 - \xi_2)\|_{L^2}^2, \end{aligned} \quad (82)$$

for all $\xi_1, \xi_2 \in H^1(\Omega)$. Note that the third term on the right hand side is strictly monotone. The first and second term on the right hand side is shown to be pseudo-monotone in lemma 6 and lemma 7 respectively. Further, the summation of a pseudo-monotone operator and a monotone operator is also pseudo-monotone (Proposition 27.6 of Zeidler [42]). Which implies T is a pseudo-monotone operator.

3. **Coercivity.** Coercivity in this context is written as

$$\frac{\langle T(u), u \rangle}{\|u\|_{H^1}} \longrightarrow \infty, \text{ as } \|u\|_{H^1} \longrightarrow \infty. \quad (83)$$

We check whether this condition is satisfied. We start from

$$\langle T(\mu), \mu \rangle = 2 \left(\left(\phi(\mu) - \phi^k \right), \mu \right) - \frac{\delta t}{2} \left(v_i(\mu) \phi(\mu), \frac{\partial \mu}{\partial x_i} \right) + \frac{\delta t}{PeCn} \left(\frac{\partial \mu}{\partial x_i}, \frac{\partial \mu}{\partial x_i} \right). \quad (84)$$

The first term can be bounded by taking the test function $q = \phi^{k+1} - \phi^k$ in eq. (22) and using the fact that ϕ^k, ϕ^{k+1} are strictly bounded between -1 and 1 :

$$\begin{aligned} (\phi^{k+1} - \phi^k, \mu) &\geq \frac{1}{8} \int_{\Omega} (\phi^{k+1})^4 dx - \frac{3}{4} \int_{\Omega} (\phi^{k+1})^2 dx + \frac{Cn^2}{2} \int_{\Omega} \sum_i \left| \frac{\partial \phi^{k+1}}{\partial x_i} \right|^2 dx \\ &\quad + \frac{3}{4} \int_{\Omega} (\phi^k)^2 dx + \frac{1}{8} \int_{\Omega} (\phi^k)^4 dx - \frac{Cn^2}{2} \int_{\Omega} \sum_i \left| \frac{\partial \phi^k}{\partial x_i} \right|^2 dx \\ &\geq \frac{1}{16} \|\phi^{k+1}\|_{L^4}^4 + \frac{Cn^2}{2} \|\nabla \phi^{k+1}\|_{L^2}^2 - C \left(\|\phi^k\|_{H^1}^4 + \|\phi^k\|_{H^1}^2 + 1 \right). \end{aligned} \quad (85)$$

Using the estimate from lemma 2, the second term on the right can be written as

$$-\delta t \left(v_i \phi, \frac{\partial \mu}{\partial x_i} \right) \geq C_3 \left[\|\mathbf{v}^{k+1}\|_{L^2}^2 - \|\mathbf{v}^k\|_{L^2}^2 + \left\| \sqrt{\eta(\phi^{k+1})} \nabla \mathbf{v} \right\|_{L^2}^2 + \left(y, \rho^{k+1} - \rho^k \right) \right]. \quad (86)$$

Collecting all inequalities, we get

$$\begin{aligned} \langle T(\mu), \mu \rangle &\geq C \|\nabla \mu\|_{L^2}^2 + \frac{1}{16} \|\phi^{k+1}\|_{L^4}^4 + \frac{Cn^2}{2} \|\nabla \phi^{k+1}\|_{L^2}^2 + C_5 \|\mathbf{v}^{k+1}\|_{L^2}^2 \\ &\quad + C_3 \left(\left\| \sqrt{\eta(\phi^{k+1})} \nabla \mathbf{v} \right\|_{L^2}^2 + \left(y, \rho(\phi^{k+1}) \right) \right) - C_b. \end{aligned} \quad (87)$$

Note, that the all the terms which depend on μ in eq. (87) are positive, and all the fields at the previous timestep (known functions) are constant, and are absorbed in C_b . To show coercivity we need to use Poincaré inequality to get the inequality in terms of μ instead of $\nabla \mu$; thus,

$$\langle T(\mu), \mu \rangle \geq C_a \|\mu\|_{H^1}^n - C_b, \quad (88)$$

where the constants are adjusted for the inequalities used and $n = 4/3$ which implied coercivity. Here we do not write other positive terms ($\frac{Cn^2}{2} \|\nabla \phi^{k+1}\|_{L^2}^2 + C_5 \|\mathbf{v}^{k+1}\|_{L^2}^2$.. so on) which are μ dependent to show the inequality in a clearer form, as they are positive and the coercivity condition is still satisfied with them included.

Remark 9. To go from eq. (87) to eq. (88), we use a particular form of the Poincaré inequality for μ given in [44]:

$$\|f\|_{H^1(\Omega)}^2 \leq (C' + 1) \|\nabla f\|_{L^2(\Omega)}^2 + C' \left(\int_{\Omega} f dx \right)^2, \quad (89)$$

$\forall f \in H^1(\Omega)$. To use this inequality for μ , one needs to bound the average $\int_{\Omega} \mu dx$ and use it in conjunction with eq. (87). Using standard inequalities one can show that $\|\phi^{k+1}\|_{L^4}^4$ bounds $\left(\int_{\Omega} \mu dx \right)^{4/3}$. Therefore, the second term in eq. (87) can be used to replace the average term in eq. (89), which gives the exponent $n = 4/3$ for $\|\mu\|_{H^1}^n$. The proof is similar to that shown in [23], so we do not reproduce it in detail here.

We proved all the required conditions for existence theorem for pseudo-monotone operators, this implies that there exists a solution μ' such that $\langle T(\mu'), w \rangle = 0, \forall w \in H^1(\Omega)$. Consequently, there $\tilde{\mu}^k$ is a solution to eq. (77). The same $\tilde{\mu}^k(\mathbf{x})$ is the source function for the mapping in lemmas 3 and 4 which provide unique solutions $\phi^{k+1}(\mathbf{x})$, and $\mathbf{v}^{k+1}(\mathbf{x})$ respectively. ■

Remark 10. *Contrary to strictly monotone operator in Han and Wang [23], the operator for our fully implicit time-scheme is pseudo-monotone. The strictly monotone operator along with the Browder-Minty theorem (theorem 2) gives uniqueness of solutions. In our case we are using a generalization of Browder-Minty theorem to pseudo-monotone operators which only gives existence of solutions. Rigorously proving uniqueness in our case is not trivial, but for practical situations we do not see any problems.*

3.4. Spatial discretization and variational multi-scale approach

In this work all the unknown variables, $(\phi, \mu, \mathbf{v}, \text{ and } p)$, are discretized in space using the standard piecewise linear continuous Galerkin or cG(1) finite element method. It is well-known in the literature that numerical instabilities occur when solving the incompressible Navier-Stokes with a numerical method that uses the same polynomial order for both the velocity and the pressure. These instabilities are due to fact that equal polynomial order representations of p and \mathbf{v} will not satisfy the inf-sup condition (Ladyzhenskaya-Babuska-Brezzi condition, see page 31 in Volker [17]). In order to overcome this difficulty, additional numerical stabilization needs to be introduced. One of the most popular stabilization techniques for this problem is the SUPG-PSPG approach: streamline-upwind/Petrov-Galerkin (SUPG) [45] and pressure-stabilizing/Petrov-Galerkin (PSPG) [46]. A generalization of these approaches is the variational multi-scale approach [47]. In this work we make use of the variational multi-scale (VMS) approach proposed in the context of large-eddy simulations (LES) [48]. This approach has the advantage that it provides a stabilization mechanism such that the inf-sup stability condition is converted to a coercivity condition, while also providing a natural leeway into modeling high Reynolds number flows in the context of LES [31].

The philosophy of VMS models follows that of LES, where we seek a direct-sum decomposition of the discrete spaces which approximate the continuous spaces. If $\mathbf{v} \in \mathbf{V}$ and $p \in Q$, then we can decompose these spaces as follows:

$$\mathbf{V} = \overline{\mathbf{V}} \oplus \mathbf{V}' \quad \text{and} \quad Q = \overline{Q} \oplus Q', \quad (90)$$

where $\overline{\mathbf{V}}$ and \overline{Q} are the cG(1) subspaces of \mathbf{V} and Q , respectively, and the primed versions are the complements of the cG(1) subspaces in \mathbf{V} and Q , respectively. We can write the decomposition for velocity and pressure as follows: $\mathbf{v} = \overline{\mathbf{v}} + \mathbf{v}'$ and $p = \overline{p} + p'$, where the *coarse scale* solution is $\overline{\mathbf{v}} \in \overline{\mathbf{V}}$, $\overline{p} \in \overline{Q}$, and the *fine scale* solution is $\mathbf{v}' \in \mathbf{V}'$ and $p' \in Q'$. We define a projection operator, $\mathcal{P} : \mathbf{V} \rightarrow \overline{\mathbf{V}}$, such that $\overline{\mathbf{v}} = \mathcal{P}\{\mathbf{v}\}$ and $\mathbf{v}' = \mathbf{v} - \mathcal{P}\{\mathbf{v}\}$. A similar operator can be used for the decomposition of

p . Substituting this decomposition in the original variational form in definition 1 yields:

$$\begin{aligned}
\text{Momentum Eqns: } & \left(w_i, \rho(\phi) \frac{\partial \bar{v}_i}{\partial t} \right) + \left(w_i, \frac{\partial (\rho(\phi) v'_i)}{\partial t} \right) + \left(w_i, \rho(\phi) \bar{v}_j \frac{\partial \bar{v}_i}{\partial x_j} \right) \\
& + \left(w_i, \rho(\phi) v'_j \frac{\partial \bar{v}_i}{\partial x_j} \right) + \left(w_i, \frac{\partial (\rho(\phi) \bar{v}_j v'_i)}{\partial x_j} \right) + \left(w_i, \frac{\partial (\rho(\phi) v'_j v'_i)}{\partial x_j} \right) \\
& + \frac{1}{Pe} \left(w_i, J_j \frac{\partial \bar{v}_i}{\partial x_j} \right) + \frac{1}{Pe} \left(w_i, \frac{\partial (J_j v'_i)}{\partial x_j} \right) + \frac{Cn}{We} \left(w_i, \frac{\partial}{\partial x_j} \left(\frac{\partial \phi}{\partial x_i} \frac{\partial \phi}{\partial x_j} \right) \right) \\
& + \frac{1}{We} \left(w_i, \frac{\partial (\bar{p} + p')}{\partial x_i} \right) + \frac{1}{Re} \left(\frac{\partial w_i}{\partial x_k}, \eta(\phi) \frac{\partial (\bar{v}_i + v'_i)}{\partial x_k} \right) - \left(\frac{w_i, \rho(\phi) \hat{g}_i}{Fr} \right) \\
& + \left(q, \frac{\partial \bar{v}_i}{\partial x_i} \right) + \left(q, \frac{\partial v'_i}{\partial x_i} \right) = 0,
\end{aligned} \tag{91}$$

$$\text{Cahn-Hilliard Eqn: } \left(q, \frac{\partial \phi}{\partial t} \right) + \left(q, \frac{\partial (\bar{v}_i \phi)}{\partial x_i} \right) - \frac{1}{Pe Cn} \left(q, \frac{\partial^2 (m(\phi) \mu)}{\partial x_i \partial x_i} \right) = 0, \tag{92}$$

$$\text{Chemical Potential: } - (q, \mu) + \left(q, \frac{d\psi}{d\phi} \right) - Cn^2 \left(q, \frac{\partial}{\partial x_i} \left(\frac{\partial \phi}{\partial x_i} \right) \right) = 0, \tag{93}$$

where $\mathbf{w}, \bar{\mathbf{v}} \in \mathcal{P}\mathbf{H}^1(\Omega)$, $\bar{p}, \phi \in \mathcal{P}H^1(\Omega)$, $\mathbf{v}' \in (\mathcal{I} - \mathcal{P})\mathbf{H}^1(\Omega)$, $p' \in (\mathcal{I} - \mathcal{P})H^1(\Omega)$, and $\mu, q \in \mathcal{P}H^1(\Omega)$. Here \mathcal{I} is the identity operator and \mathcal{P} is the projection operator. We use the residual-based approximation proposed by Bazilevs et al. [31] for fine scale components to close the equations, which is given by

$$\rho(\phi) v'_i = -\tau_m \mathcal{R}_m(\rho, \bar{v}_i, \bar{p}) \quad \text{and} \quad p' = -\rho(\phi) \tau_c \mathcal{R}_c(\bar{v}_i). \tag{94}$$

It is important to note that because we are using block iterative method, the momentum equations, eq. (91), and the Cahn-Hilliard equations, eq. (92) and eq. (93), are solved as two different nonlinear sub-problems. We use conforming Galerkin based finite elements and replace the continuous spaces with their discrete counterparts; notice that as we only solve for course scale components, the trial functions and the basis functions are in the same space. Then we can write a discrete variational formulation can we written as follows.

Definition 3. Find $\bar{\mathbf{v}}^h \in \mathcal{P}\mathbf{H}^{1,h}(\Omega)$ and $\bar{p}^h, \phi^h, \mu^h \in \mathcal{P}H^{1,h}(\Omega)$ such that

$$\begin{aligned}
\text{Momentum Eqns: } & \left(w_i, \rho(\phi^h) \frac{\partial \bar{v}_i^h}{\partial t} \right) + \left(w_i, \rho(\phi^h) \bar{v}_j^h \frac{\partial \bar{v}_i^h}{\partial x_j} \right) - \left(w_i, \tau_m \mathcal{R}_m(\bar{v}_j^h, \bar{p}^h) \frac{\partial \bar{v}_i^h}{\partial x_j} \right) \\
& + \left(\frac{\partial w_i}{\partial x_j}, \bar{v}_j^h \left(\tau_m \mathcal{R}_m(\bar{v}_i^h, \bar{p}^h) \right) \right) - \left(\frac{\partial w_i}{\partial x_j}, \frac{\tau_m^2}{\rho(\phi^h)} \mathcal{R}_m(\bar{v}_j^h, \bar{p}^h) \mathcal{R}_m(\bar{v}_i^h, \bar{p}^h) \right) \\
& + \frac{1}{Pe} \left(w_i, J_j^h \frac{\partial \bar{v}_i^h}{\partial x_j} \right) + \frac{1}{Pe} \left(\frac{\partial w_i}{\partial x_j}, J_j^h \frac{\tau_m}{\rho(\phi^h)} \mathcal{R}_m(\bar{v}_i^h, \bar{p}^h) \right) \\
& - \frac{Cn}{We} \left(\frac{\partial w_i}{\partial x_j}, \frac{\partial \phi^h}{\partial x_i} \frac{\partial \phi^h}{\partial x_j} \right) - \frac{1}{We} \left(\frac{\partial w_i}{\partial x_i}, \bar{p}^h \right) \\
& + \frac{1}{We} \left(\frac{\partial w_i}{\partial x_i}, \rho(\phi^h) \tau_c \mathcal{R}_c(\bar{v}_i^h) \right) + \frac{1}{Re} \left(\frac{\partial w_i}{\partial x_k}, \eta(\phi^h) \frac{\partial \bar{v}_i^h}{\partial x_k} \right) \\
& - \left(\frac{w_i, \rho(\phi^h) \hat{g}_i}{Fr} \right) + \left(q, \frac{\partial \bar{v}_i^h}{\partial x_i} \right) - \left(\frac{\partial q}{\partial x_i}, \frac{\tau_m}{\rho(\phi^h)} \mathcal{R}_m(\bar{v}_i^h, \bar{p}^h) \right) = 0,
\end{aligned} \tag{95}$$

$$\text{Cahn-Hilliard Eqn: } \left(q, \frac{\partial \phi^h}{\partial t} \right) - \left(\frac{\partial q}{\partial x_i}, \bar{v}_i^h \phi^h \right) + \frac{1}{PeCn} \left(\frac{\partial q}{\partial x_i}, \frac{\partial (m(\phi^h) \mu^h)}{\partial x_i} \right) = 0, \tag{96}$$

$$\text{Chemical Potential: } - \left(q, \mu^h \right) + \left(q, \frac{d\psi}{d\phi^h} \right) + Cn^2 \left(\frac{\partial q}{\partial x_i}, \frac{\partial \phi^h}{\partial x_i} \right) = 0, \tag{97}$$

where,

$$\tau_m = \left(\frac{4}{\Delta t^2} + \bar{v}_i^h G_{ij} \bar{v}_j^h + \frac{1}{(\rho(\phi^h) Pe)} \bar{v}_i^h G_{ij} J_j^h + C_I \left(\frac{\eta(\phi^h)}{\rho(\phi^h) Re} \right)^2 G_{ij} G_{ij} \right)^{-1/2}, \tag{98}$$

$$\tau_c = \frac{1}{tr(G_{ij}) \tau_m}. \tag{99}$$

Here we set C_I for all our simulations to 6 and the residuals are given by

$$\begin{aligned}
\mathcal{R}_m(\bar{v}_i^h, \bar{p}^h) &= \rho(\phi) \frac{\partial \bar{v}_i^h}{\partial t} + \rho(\phi) \bar{v}_j^h \frac{\partial \bar{v}_i^h}{\partial x_j} + \frac{1}{Pe} J_j^h \frac{\partial \bar{v}_i^h}{\partial x_j} + \frac{Cn}{We} \frac{\partial}{\partial x_j} \left(\frac{\partial \phi^h}{\partial x_i} \frac{\partial \phi^h}{\partial x_j} \right) \\
&+ \frac{1}{We} \frac{\partial \bar{p}^h}{\partial x_i} - \frac{1}{Re} \frac{\partial}{\partial x_k} \left(\eta(\phi) \frac{\partial \bar{v}_i^h}{\partial x_k} \right) - \frac{\rho(\phi) \hat{g}_i}{Fr},
\end{aligned} \tag{100}$$

$$\mathcal{R}_c(\bar{v}_i^h) = \frac{\partial \bar{v}_i^h}{\partial x_i}. \tag{101}$$

Finally, we note that in the above expressions the time derivative is still continuous. In the fully discrete numerical method we replace the time-derivatives in the momentum and phase field equations using the trapezoidal rule in the form of the scheme presented in eq. (13) – eq. (18).

3.5. Handling non-linearity

The fully discretized system is a collection of two non-linear systems of algebraic equations, one corresponding to the discretized version of the momentum equations (eqs. (19) to (21)), the other

corresponding to the Cahn-Hilliard equations, eqs. (21) and (23). Because we use an implicit time-stepping strategy, an internal (within each block iteration) Newton’s method is used to solve the aforementioned non-linear algebraic equations. Newton’s method for a system of equations can be written as follows:

$$J_{ij}^k \delta U_j^k = -F_i^{s,k}(U_1^{s,k}, U_2^{s,k}, \dots, U_n^{s,k}), \quad (102)$$

$$J_{ij}^k := \frac{\partial}{\partial U_j}(F_i^{s,k}(U_1^s, U_2^s, \dots, U_n^s)), \quad (103)$$

where $U_j^{s,k}$ is a vector of all degrees of freedom at the k^{th} time step and at the s^{th} Newton iteration. δU_j^k is a vector of the “perturbation” in the degrees of freedom from the previous Newton iteration. An initial guess $U_i^{0,k}$ must be provided to start the iteration. J_{ij}^k is a Jacobian matrix (very similar to the gradient term in the 1D root finding Newton’s algorithm). $F_i^{s,k}$ is the function of the degrees of freedom at the s^{th} Newton iteration which is being minimized. One can calculate J_{ij}^k either numerically using finite differences or analytically. We calculate J_{ij}^k analytically by calculating the variations (partial differentials) of the operators with respect to the degrees of freedoms. Using this technique, $U_j^{s,k}$ can be updated as follows until the desired tolerances are reached:

$$U_j^{s+1,k} = U_j^{s,k} + \delta U_j^k. \quad (104)$$

In the time-stepping context the solution vector at the previous time step can be used to initiate the Newton iteration at each timestep. Here eq. (102) is the linear system which has to be solved at each Newton iteration on a massively parallel scale for two sets of PDEs working in a block iteration setup. In order to handle the Newton iterations and the embedded linear solves, we make use of the PETSC library, which provides parallel efficient implementations of the above ideas along with a large suite of preconditioners and solvers for the linear system [49, 50, 51]. The choice of linear solvers and preconditioner is different for different numerical experiments and more details are provided in the respective sections for those results.

4. Octree based finite element discretisation and remeshing

While the concept of adaptive space partitions is well studied, developing such methods for applications demanding frequent refinements on large distributed systems presents significant challenges. This work builds on existing methods for performing large-scale finite element computations using octree-refined meshes. The octree-based framework, DENDRO is extended to support sub-domains, primarily with the objective of supporting long channels and division of the domain based on arbitrary functions that define the geometry. We provide a brief description on building the octree mesh in parallel and performing finite element computations. Additional details can be found in [52]. DENDRO provides the adaptive mesh refinement (AMR) and all parallel data-structures, and for this project, DENDRO was extended to support domains that are not cuboidal in shape. We give a brief overview of the DENDRO framework and provide details on the new contributions. The main steps in building and maintaining an adaptively refined mesh in a distributed-memory machine are described below.

Refinement:. The sparse grid is constructed based on the geometry. Proceeding in a top-down fashion, a cell is refined if a surface (defined by a zero level-set of a field, or a cloud of points) passes

through it. We also provide an additional function that tests for membership and eliminates regions outside the domain. This is necessary as by definition the octree maps to a cuboidal domain. By eliminating regions, we can support arbitrary domains, including domains with holes, such as porous media. For long channels, such a pruning of the octree mesh is preferable to stretching the domain, as it keeps the elements isotropic and results in better conditioning of the operators.

Since the refinement happens in an element-local fashion, this step is embarrassingly parallel. The user provides a function (as a C++ lambda function) that given coordinates, x, y, z returns the distance from the surface. The eight corners of an octant are tested using this function. If all 8 points have a positive distance (outside), then we retain this element, but do not refine further. If all 8 points have a negative distance (inside), then this element is removed from the mesh. If some of the corners of the octant are inside and others outside, then this octant is refined. This is repeated till the desired level of refinement is achieved.

In distributed memory, the initial top-down tree construction, also enables an efficient partitioning of the domain across an arbitrary number of processes. All processes start at the root node (i.e., the cubic bounding box for the entire domain). In order to avoid communication during the refinement stage, we opt to perform redundant computations on all processes. Starting from the root node, all processes refine (similar to the sequential code) until at least $\mathcal{O}(p)$ octants requiring further refinement are produced. Then using a weighted space-filling-curve (SFC) based partitioning, we partition the octants across all processes. Note that we do not communicate the octants as every process has a copy of the octants, and all that needs to be done at each process is to retain a subset of the current octants corresponding to its sub-domain. This allows us to have excellent scalability, as all processes perform (roughly) the same amount of work without requiring any communication. The SFC-based partitioning also ensures load balancing for subsequent stages and minimizes data-dependencies from the resulting partition. See Sundar et al. [53], Fernando et al. [54] for additional details on the tree construction and partitioning. This produces a non-cuboidal octree that is refined to the geometry. For geometry that are stretched along certain directions, or domains with large voids/holes, eliminating regions keeps the overall problem sizes small, without adversely affecting the conditioning of the system. Refinement is followed by enforcing a constraint on the size of neighbouring elements, called 2:1 balancing. This is important to ensure that the neighborhood maps and data-structures are bounded, and also maximizes the sparsity of the assembled matrices.

2:1 Balancing: We enforce a condition in our distributed octrees that no two neighboring octants differ in size by more than a factor of two. This makes subsequent operations simpler without affecting the adaptive properties. Our balancing algorithm is similar to existing approaches for balancing octrees [55, 56, 53] with the added aspect that it does not generate octants if the ancestor does not exist in the input. This is done to ensure that regions that were previously eliminated are not filled in. The algorithm proposed by Bern et al. [55] is easily extensible to support this case, as we simply need to skip adding balancing octants that violate the criteria. The basic idea is to visit each element and generate balancing octants, i.e., neighbouring octants that are larger without violating the balance condition. These can be generated (locally) in an efficient manner by using an efficient ordered set data-structure like AVL-trees [57]. In distributed memory, we sort the octants according to the Morton order and remove duplicate octants to obtain the balanced octree.

Partition: Refinement and the subsequent 2:1 balancing of the octree can result in a non-uniform distribution of elements across the processes, leading to load imbalance. This is particularly challenging when arbitrary geometries are meshed, as this can make the mesh heavily load-imbalanced. The Morton ordering enables us to equipartition the elements by performing a parallel scan on the

number of elements on each process followed by point-to-point communication to redistribute the elements. As we refine near the two-phase interface, it can affect the performance, as it is likely localized on a small subset of processes, this where Morton ordering comes to rescue and delivers an effective partition. The partitioning scheme is able to handle arbitrary geometries as the partition only tries to equally divide the retained elements across the processes. The weighted partitioning, is a straightforward extension of our SFC-based partitioning that provides variable weight to the elements based on whether the element lies inside the retained domain of the arbitrary geometry or not. This allows us to more accurately estimate the work on each partition and provide better parallel load-balancing. Additional details on SFC-based partitioning and its implementation details in DENDRO can be found in Fernando et al. [54].

Meshing:. By meshing we refer to the construction of the (numerical) data structures required for finite element computations from the (topological) octree data. DENDRO already has efficient implementations for building the required neighborhood information and for managing overlapping domains between processors (*ghost* or *halo* regions). The key difference with our previous applications is the requirement to handle arbitrary geometries, as all neighbors might not be present in the mesh. This also complicates the process of applying boundary conditions. We added support for defining *subdomains* within DENDRO. The subdomains are defined using a function that takes a coordinate (x, y, z) as input and returns true or false depending on whether that coordinate is part of the subdomain or not. The subdomain leverages the core mesh data-structure and additionally defines a unique mapping for nodes that are part of the subdomain. It also keeps track of which nodes belong to subdomain boundaries. Therefore, subdomains have a small overhead and store significantly less data than the main mesh data-structure. For our target application, it is important to identify the external (domain) boundary as this dictates which elements will be retained in the domain. Therefore, the subdomain stores two bits to keep track of whether a node is non-boundary, or external. Additional details on the construction of the meshing-related data structures can be found in Sundar et al. [52].

Handling hanging nodes:. While the use of quasi-structured grids such as octree-grids makes parallel meshing scalable and efficient, without sacrificing adaptivity, one challenge is to efficiently handle the resulting non-conformity. This results in so called *hanging nodes* occurring on faces/edges shared between unequal elements that do not represent independent degrees of freedom. In order to minimize the memory footprint and overall efficiency, the hanging nodes are not stored in DENDRO. Instead, since they are constrained by the order of the elements and the non-hanging nodes on the hanging face/edge, we introduce these as temporary variables before elemental matrix assembly or matrix-vector multiplication⁹ and eliminate them following the elemental operation. This is fairly straightforward given that our meshes are limited to a 2:1 balance, limiting the number of overall cases to be considered. Additional details on the handling of hanging nodes in DENDRO can be found in Sundar et al. [53, 52].

Intergrid transfers. An essential requirement is to adapt the spatial mesh as the interface moves across the domain. An example of the adaptive mesh refinement following the moving bubble is shown in Figure 10. In the distributed memory setting, this also indicates a need to repartition and rebalance the load. Every few time steps, we remesh. This is similar to the initial mesh generation and refinement, except that it is now based on the current position of the interface as well as the original geometry. This is followed by the 2:1 balance enforcement and meshing. Once the

⁹for Matrix-free computations

new mesh is generated, we transfer the velocity field from the old mesh to the new mesh using interpolation as needed. Since the intergrid transfer happens only between parent and child (for coarsening and refinement) or remains unchanged, this can be performed on the old mesh using standard polynomial interpolation, followed by a simple repartitioning based on the new mesh (Note that the use of SFCs makes this a linear shift). Additional details on efficient implementation of distributed-memory intergrid transfers across octree meshes can be found in Sundar et al. [58].

5. Numerical experiments

5.1. 2D manufactured solutions

We first compare convergence and other properties using the method of manufactured solutions. The idea of this approach is to input a “solution” that satisfies solenoidality, but not necessarily the full set of evolution equations. Instead, the residual from plugging this “solution” into the full Cahn-Hilliard Navier-Stokes system becomes a forcing term on the right-hand side of eq. (19) – eq. (23). We select the following “solution” with appropriate forcing terms:

$$\begin{aligned} \mathbf{v} &= (\sin(\pi x_1) \cos(\pi x_2) \sin(t), -\cos(\pi x_1) \sin(\pi x_2) \sin(t), 0), \\ p &= \sin(\pi x_1) \sin(\pi x_2) \cos(t), \quad \phi = \cos(\pi x_1) \cos(\pi x_2) \sin(t), \\ \mu &= \cos(\pi x_1) \cos(\pi x_2) \sin(t). \end{aligned} \tag{105}$$

We compute numerical solutions with the following non-dimensional parameters: $Re = 10$, $We = 1$, $Cn = 1.0$, $Pe = 3.0$, and $Fr = 1.0$. The density ratio is set to be $\rho_-/\rho_+ = 0.85$. We use a 2D uniform mesh with 450×450 bilinear elements (quads) for all the numerical experiments in this sub-section. We test the numerical framework using various time-steps to check for convergence in time. Panel (a) of fig. 2 shows the temporal convergence of the L^2 errors (numerical solution compared with the manufactured solution) calculated at $t = \pi$ to allow for one complete phase with respect to time-steps. It can be clearly seen that on a log-log scale of error vs. time-step, the errors are decreasing with a slope close to two for the phase-field parameter ϕ which demonstrates second order convergence. For velocity the slopes taper off from close to 1.5 with decreasing time steps. We expect this tapering off at smaller time-steps due to the effect of spatial errors.

We next conduct a spatial convergence study. We fix the time step at $\delta t = 10^{-3}$, and vary the spatial mesh resolution. Panel (b) of fig. 2 shows the spatial convergence of L^2 errors (numerical solution compared with the manufactured solution) at $t = 0.2$. Table 1 shows the errors and the rate of change of errors for varying spatial grid spacing for velocity and ϕ ; we observe second order convergence for both velocity and ϕ .

Panel (c) of fig. 2 shows mass conservation for an intermediate resolution simulation with $\delta t = 10^{-3}$ and 175×175 elements. We plot mass drift (i.e. $\int_{\Omega} \phi(., t) dx - \int_{\Omega} \phi(., t = 0) dx$), and we expect this value to be very close to zero as per the theoretical prediction of proposition 1. We observe excellent mass conservation with fluctuations of the order of 10^{-12} (which is close to machine precision).

For the Navier-Stokes (NS) block we use a relative tolerance of 10^{-10} , and for the Cahn-Hilliard (CH) block the relative tolerance is set to 10^{-10} . For the linear solves within each Newton iteration, for NS we use a relative tolerance of 10^{-7} , and for CH relative tolerance is set to 10^{-7} . The tolerance for block iteration errors is set to 10^{-4} ($\text{block}_{\text{tol}}$ from fig. 1).

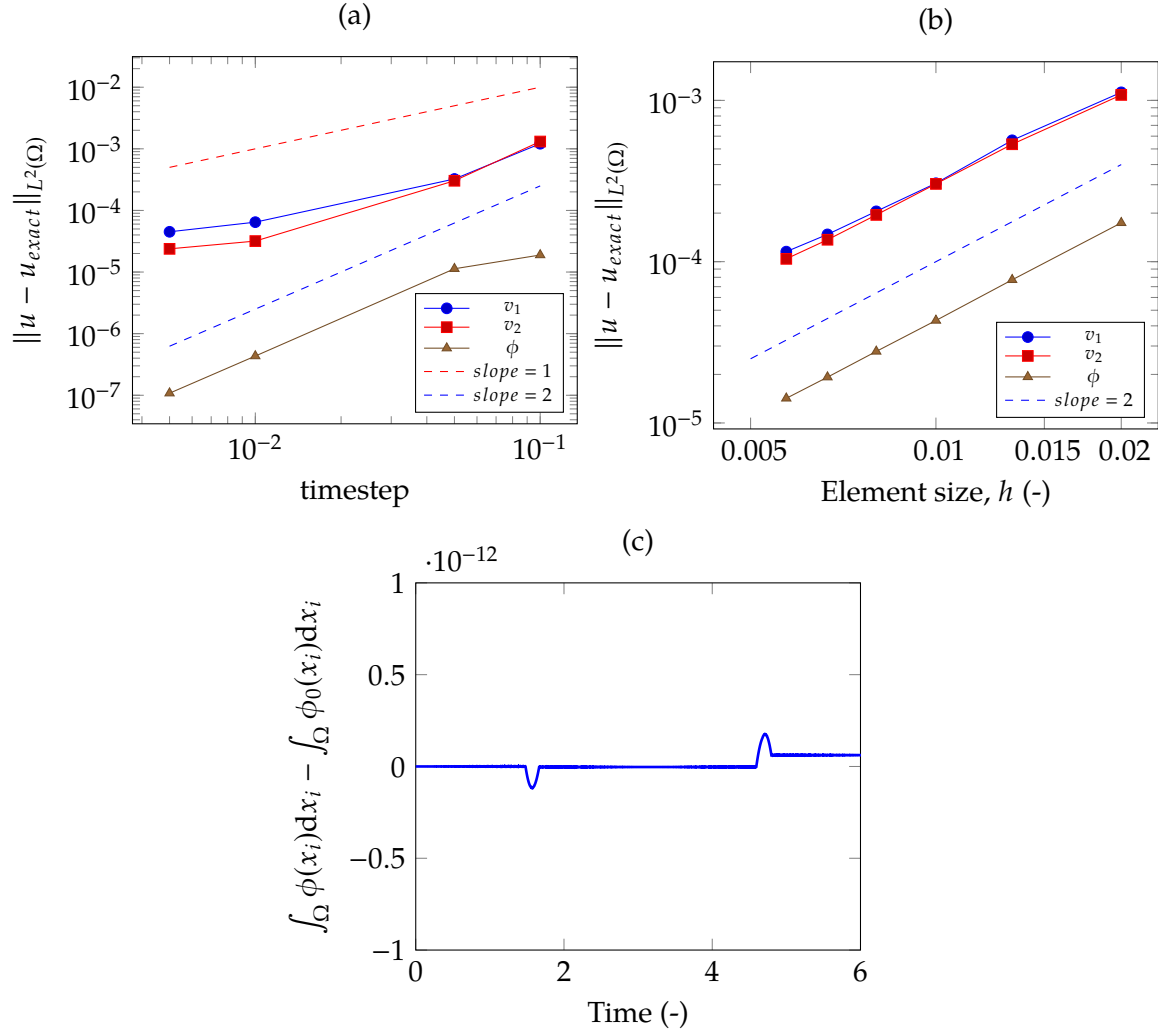


Figure 2: *Manufactured Solution Examples* (section 5.1): (a) Temporal convergence of the numerical scheme for the case of manufactured solutions; (b) spatial convergence of the numerical scheme for the case of manufactured solutions; (c) mass conservation for the case of manufactured solutions using 175×175 elements with time step of 10^{-3} .

Resolution (h)	v_1		v_2		ϕ	
	$\ v_1 - v_{1,exact}\ _{L^2(\Omega)}$	Rate	$\ v_2 - v_{2,exact}\ _{L^2(\Omega)}$	Rate	$\ \phi - \phi_{exact}\ _{L^2(\Omega)}$	Rate
1/50	1.12146×10^{-3}	-	1.08111×10^{-3}	-	1.74074×10^{-4}	-
1/75	5.65573×10^{-4}	1.678	5.34651×10^{-4}	1.726	7.71813×10^{-5}	1.9936
1/100	3.06388×10^{-4}	2.149	3.03545×10^{-4}	1.985	4.31879×10^{-5}	2.0359
1/125	2.05091×10^{-4}	1.798	1.94995×10^{-4}	1.983	2.77703×10^{-5}	1.979
1/150	1.47591×10^{-4}	1.804	1.47591×10^{-4}	1.945	1.92326×10^{-5}	2.0149
1/175	1.15397×10^{-4}	1.5963	1.15397×10^{-4}	1.768	1.42145×10^{-5}	1.9614

Table 1: *Manufactured Solution Examples* (section 5.1): Spatial convergence of the numerical scheme for the case of manufactured solutions with time step of 10^{-3} .

5.2. Single rising bubble: 2D Benchmarks

We next illustrate the framework using a canonical case of a single air bubble rising in a quiescent channel of water. This is a well studied case, and several benchmark studies have been published [59, 60, 61]. We start with selecting appropriate scales to non-dimensionalize the problem. We begin with setting the Froude number ($Fr = u^2/(gD)$) to 1.0, which fixes the non-dimensional velocity scale to $u = \sqrt{gD}$, where g is the gravitational acceleration, and D is the diameter of the bubble. This gives a Reynolds number of $\rho_c g^{1/2} D^{3/2} / \mu_c$, where ρ_c and μ_c are the specific density and specific viscosity of the continuous fluid (i.e. water) respectively. The non-dimensional group $\rho_c g^{1/2} D^{3/2} / \mu_c$ is called the Archimedes number (Ar) and is a variant of the Reynolds number; it serves as a coefficient in front of the diffusion term in the momentum equation. Further, the same choice of non-dimensional scales leads to a Weber number ($We = \rho_c g D^2 / \sigma$). We use the density of the continuous fluid (i.e., water) to non-dimensionalize; in this case $\rho_+ = 1$. Further, the density ratio is given by ρ_+ / ρ_- . Similarly, ν_+ / ν_- is the viscosity ratio. We present results for two test cases that are popularly reported in the benchmark studies.

Table 2 shows the parameters and the corresponding non-dimensional numbers. The bubble is centered at (1, 1), and since our scaling length scale is the bubble diameter, the bubble diameter for our simulations is 1. The domain is $[0, 2] \times [0, 4]$. Following the benchmark studies in the literature we choose the top and bottom wall to have no slip boundary conditions and the side walls to have boundary conditions: $v_1 = 0$ (x -velocity) and $\frac{\partial v_2}{\partial x} = 0$ (y -velocity). We use the biCGstab (bcgs) linear solver from the PETSc suite along with the Additive Schwarz (ASM) preconditioner for the linear solves in the Newton iterations (see section 3.5). We use a time step of 2.5×10^{-3} for both the test cases.

The convergence criterion for both the test cases is as follows. For the Navier-Stokes (NS) block we use a relative tolerance of 10^{-6} , and for the Cahn-Hilliard (CH) block the relative tolerance is set to 10^{-8} . The tolerance for block iteration errors is set to 10^{-4} (block_{tol} from fig. 1).

Test Case	ρ_c	ρ_b	μ_c	μ_b	ρ_+ / ρ_-	ν_+ / ν_-	g	σ	Ar	We	Fr
1	1000	100	10	1.0	10	10	0.98	24.5	35	10	1.0
2	1000	1.0	10	0.1	1000	100	0.98	1.96	35	125	1.0

Table 2: Physical parameters and corresponding non-dimensional numbers for the 2D single rising drop benchmarks considered in section 5.2.

5.2.1. Test case 1

This test case considers the effect of higher surface tension and consequently less deformation of the bubble as it rises. We compare the bubble shape in fig. 3 with benchmark quantities presented

in three previous studies [59, 60, 61]. We take $Cn = 5 \times 10^{-3}$ for this case. Panel (a) of fig. 3 shows a shape comparison against benchmark studies in the literature, and we see an excellent agreement in the shape of the bubble. Panel (b) of fig. 3 shows a comparison of centroid locations with respect to time against benchmark studies in the literature; again we see excellent agreement. We can see from the magnified inset in panel (b) of fig. 3 that as we keep increasing the mesh resolution the plot approaches the benchmark studies, and we see an almost exact overlap between the benchmark and cases with $h = 2/400$ and $h = 2/600$, where h is the size of the element, demonstrating spatial convergence.

We next check whether the numerical method follows the theoretical energy stability proved in theorem 1. We present the evolution of the energy functional defined in eq. (9) for test case 1. Panel (c) of fig. 3 shows that the energy is decreasing in accordance with the energy stability condition for all three spatial resolutions of $h = 2.0/200$, $h = 2.0/400$, and $h = 2.0/600$.

Finally we check the mass conservation. Panel (d) shows the total mass of the system minus the initial mass. At all reported spatial resolutions the change in the total mass is of the order of 10^{-8} , even after 1600 time steps. It is clear that the numerical method follows excellent mass conservation across long time horizons.

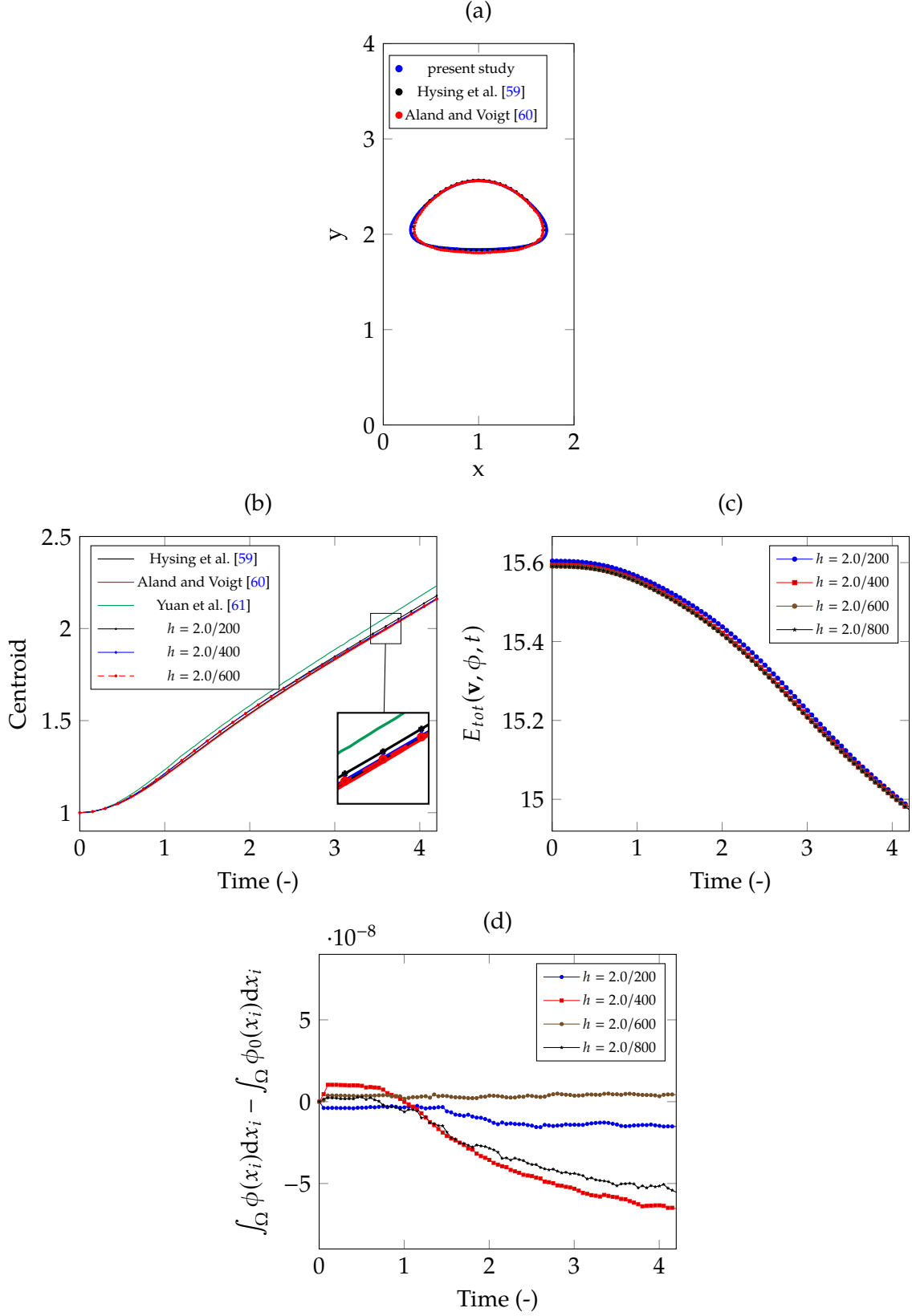


Figure 3: 2D Single Rising Drop Test Case 1 (section 5.2.1): (a) Comparison of the computed bubble shape against results from the literature at non-dimensional time $T = 4.2$; (b) comparison of the rise of the bubble centroid against results from the literature; (c) decay of the energy functional illustrating theorem 1; and (d) total mass conservation (integral of total ϕ).

5.2.2. Test case 2

This test case considers a lower surface tension resulting in high deformations of the bubble as it rises. As before, we compare the bubble shape in fig. 4 with benchmark quantities presented in three previous studies [59, 60, 61]. Panel (a) shows the shape comparison with benchmark studies in the literature and we see an excellent agreement in the shape of the bubble. All simulations (our results and benchmarks) exhibit a skirted bubble shape. We see an excellent match in the overall shape of the bubble with some minor differences in the dynamics of the tails of the bubble. Specifically, we see that the tails of bubble in our case pinch-off to form satellite bubbles¹⁰. We performed this simulation with a $Cn = 0.0025$ and three different spatial resolutions. We can see in panel (a) of fig. 4 that our simulation captures this filament pinch off in the tails very well. It is important to note that Aland and Voigt [60], Yuan et al. [61] did not observe these thin tails and pinch-off, whereas Hysing et al. [59] did observe pinch-off of the tails and satellite bubbles. The dynamics of this bubble tail is highly dependent on the numerical method used.

Panel (b) of fig. 4 shows comparison of centroid location with respect to time. Again we see an excellent agreement with all three previous benchmark studies. We can see from the magnified inset in panel (b) of fig. 4 that as we keep increasing the mesh resolution the plot approaches the benchmark studies and we see an almost exact overlap between the benchmark and cases with $h = 2/1000$ and $h = 2/2000$ demonstrating spatial convergence. Next, we report the evolution of the energy functional defined in eq. (9) for test case 2. Panel (c) of fig. 4 shows the decay of the total energy functional in accordance with the energy stability condition for all three spatial resolutions of $h = 2.0/800$, $h = 2.0/1000$, and $h = 2.0/1200$. Finally, panel (d) of fig. 4 shows the total mass of the system in comparison with the total initial mass of the system. We can see that for all spatial resolution the change in the total mass with respect to the initial total mass is of the order of 1×10^{-8} . This illustrates that the numerical method satisfies mass conservation over long time horizons.

¹⁰Such instabilities require a very low Cn number, as a very thin interfacial thickness is required to capture the dynamics of the thin tails of the bubble

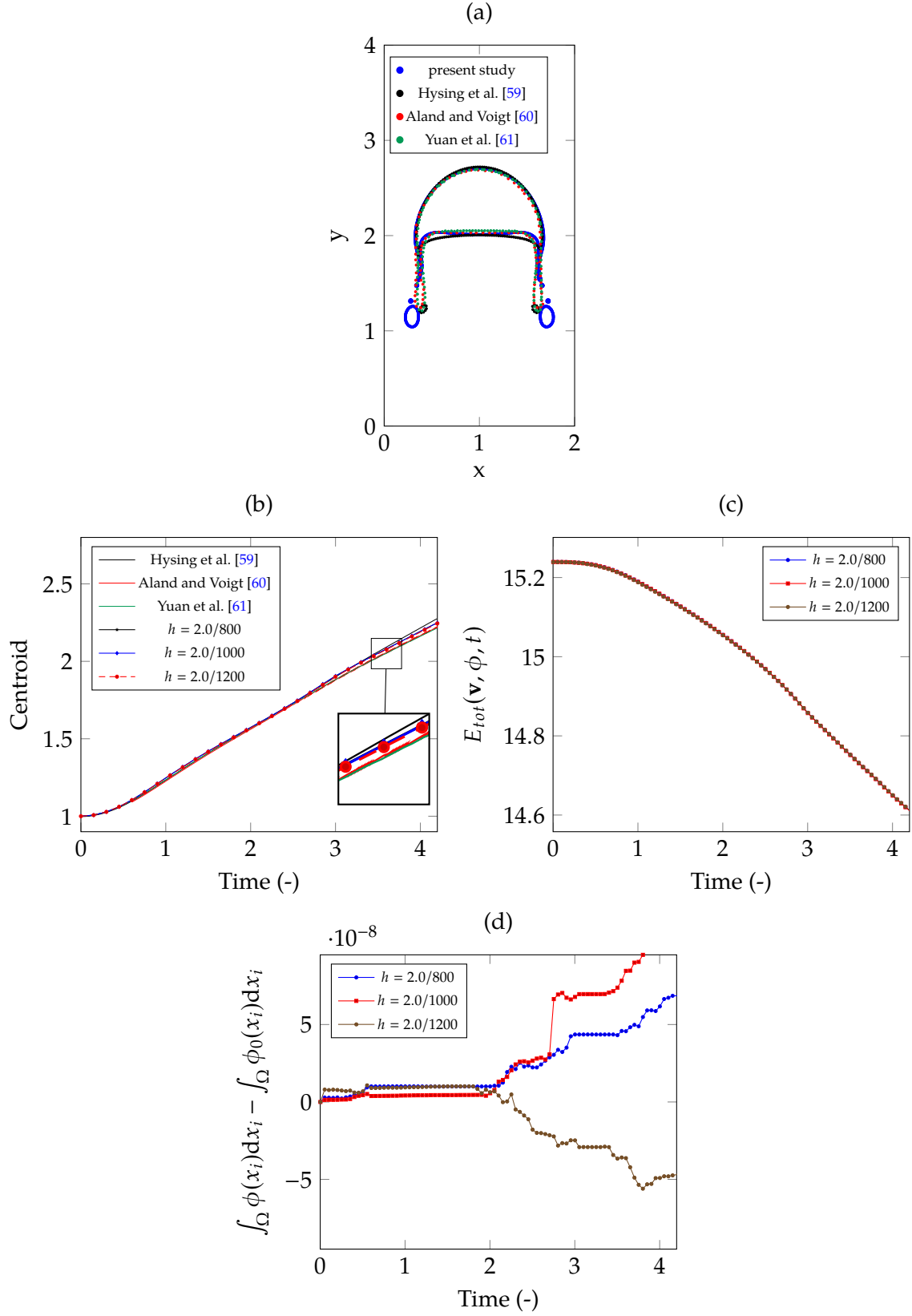


Figure 4: 2D Single Rising Drop Test Case 2 (section 5.2.2): (a) Comparison of the computed bubble shape against results from the literature at non-dimensional time $T = 4.2$; (b) comparison of the rise of the bubble centroid against results from the literature; (c) decay of the energy functional illustrating theorem 1; and (d) total mass conservation (integral of total ϕ).

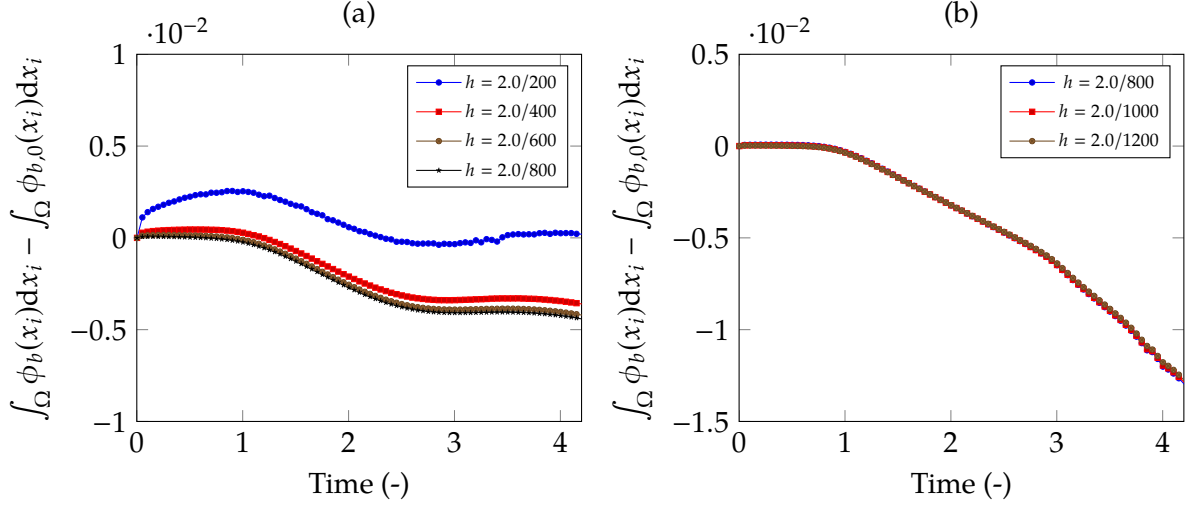


Figure 5: *Bubble Mass Conservation for the 2D Rising Drop Test Cases:* (a) Mass conservation of bubble (integral of $\phi < 0$) for test case 1 (section 5.2.1); (b) mass conservation of bubble (integral of $\phi < 0$) for test case 2 (section 5.2.2)

Another important aspect we report is the mass conservation of the lighter bubble. The mass of the bubble is a small fraction ($\sim 10\%$) of the total volume and is thus a more stringent test of mass conservation. We plot mass loss (mass of bubble at time t - initial mass of bubble) as a function of time in fig. 5 for both test cases. For test case 1 panel (a) of fig. 5 shows the mass loss of bubble as a function of time and we can see that for all four spatial resolutions, the change in mass of the bubble compared to initial mass of the bubble¹¹ is within the bound of $\pm 5 \times 10^{-3}$, which shows that the mass loss of the bubble is less than 0.5% over this long time horizon. For test 2, on the other hand, mass conservation of the bubble is typically difficult to capture because of the pinch off and formation of small satellite bubbles. Even for this challenging case (panel (b) of fig. 5), the change in mass of the bubble compared to initial mass of the bubble is within the bound of $\pm 5 \times 10^{-3}$ which is again less than a 0.5% change.

5.3. Rayleigh-Taylor instability: 2D simulations

Performance of the framework at higher Reynolds numbers and large changes in the topology of the interface can be demonstrated by simulating the Rayleigh-Taylor instability. While the bubble rise case is an interplay between surface tension and buoyancy, the physics of a Rayleigh-Taylor instability is dominated by buoyancy. A lot of studies in the literature also switch off the surface tension forcing terms in the momentum equations (see [14, 62, 63, 64] for examples). Here, the choice of non-dimensional numbers ensures that surface tension effect is small (high Weber numbers). The setup is as follows: the heavier fluid is placed on top of lighter fluid and the interface is perturbed. The heavier fluid on top penetrates into the lighter fluid and buckles, which generates instabilities. This interface motion is very difficult to track in interface resolved simulations (like the current ones), as the changes in the topology of the interface are large and Rayleigh-Taylor instabilities generally encompass turbulent conditions which calls for resolving finer scales. We non-dimensionalize the problem by selecting the width of the channel as the characteristic length scale and the density of the lighter fluid as the characteristic specific density. Just like in the case of bubble rise we use buoyancy-based scaling, setting the Froude number ($Fr = u^2/(gD)$) to 1.0,

¹¹we calculate this by integrating $\phi < 0$ over the domain

which fixes the non-dimensional velocity scale to be $u = \sqrt{gD}$, where g is the gravitational acceleration, and D is the width of the channel. Using this velocity to calculate the Reynolds number, we get $Re = \rho_L g^{1/2} D^{3/2} / \mu_L$, where ρ_L and μ_L are the specific density and specific viscosity of the light fluid respectively. We set the Reynolds number at 3000. Furthermore, the same choice of non-dimensional scales leads to a Weber number ($We = \rho_c g D^2 / \sigma$). To compare our results with previous studies, we simulate with same initial conditions as presented in Tryggvason [65], Guermont and Quartapelle [64], Ding et al. [66], Xie et al. [14]. The We number is selected to be 1000, so that the effect of surface tension is small on the evolution of interface. In this case, similar to the bubble rise case we have chosen specific density of the light fluid to non-dimensionalize, therefore $\rho_+ = 1.0$. Further, for the 2D simulations we choose two density ratios (ρ_+/ρ_-) of 0.33, and 0.1 respectively. Similarly, ν_+/ν_- is the viscosity ratio which is selected to be 1.0. In the literature Atwood number (At) is often used to parametrize the dependence on density ratio which is given by $At = (\rho_+ - \rho_-) / (\rho_+ + \rho_-)$. For the density ratios of 0.33, and 0.1, the Atwood numbers are $At = 0.5$, and $At = 0.82$ respectively. The boundary conditions we use are no-slip for velocity on all the walls and no flux conditions for ϕ and μ . We assume a 90 degree wetting angle for both the fluids. The simulations were performed using a time step of 10^{-4} .

Figure 6 shows the snapshots of the interface shape as it evolves in time. We can see the heavier fluid penetrating in the light fluid, and the light fluid rises up near the wall. For both cases of $At = 0.5$ and $At = 0.82$ a number of previous studies have presented the location of top front and bottom front as a function of time. Panel (a) fig. 7 shows the comparison of locations of bottom and top front of the interface with previous studies [14, 62, 63, 64]. We can clearly see that the results from the current study match the previous benchmarks very well. Panel (b) from fig. 7 shows the decay of energy functional in line with theorem 1 for $At = 0.5$. Panel (c) from fig. 7 shows the change in the total mass with respect to the initial total mass. We observe that it is of the order of 10^{-13} . Therefore, we see excellent mass conservation even with high amount of deformation of the interface over very large time horizons (over 30,000 time steps).

The convergence criterion for both the 2D Rayleigh-Taylor test cases are as follows. For the Navier-Stokes (NS) block we use a relative tolerance of 10^{-6} , and for the Cahn-Hilliard (CH) block the relative tolerance is set to 10^{-10} . For the linear solves within each Newton iteration, for NS we use a relative tolerance of 10^{-7} , and for CH relative tolerance is set to 10^{-7} . The tolerance for block iteration errors is set to 10^{-4} ($block_{tol}$ from fig. 1).

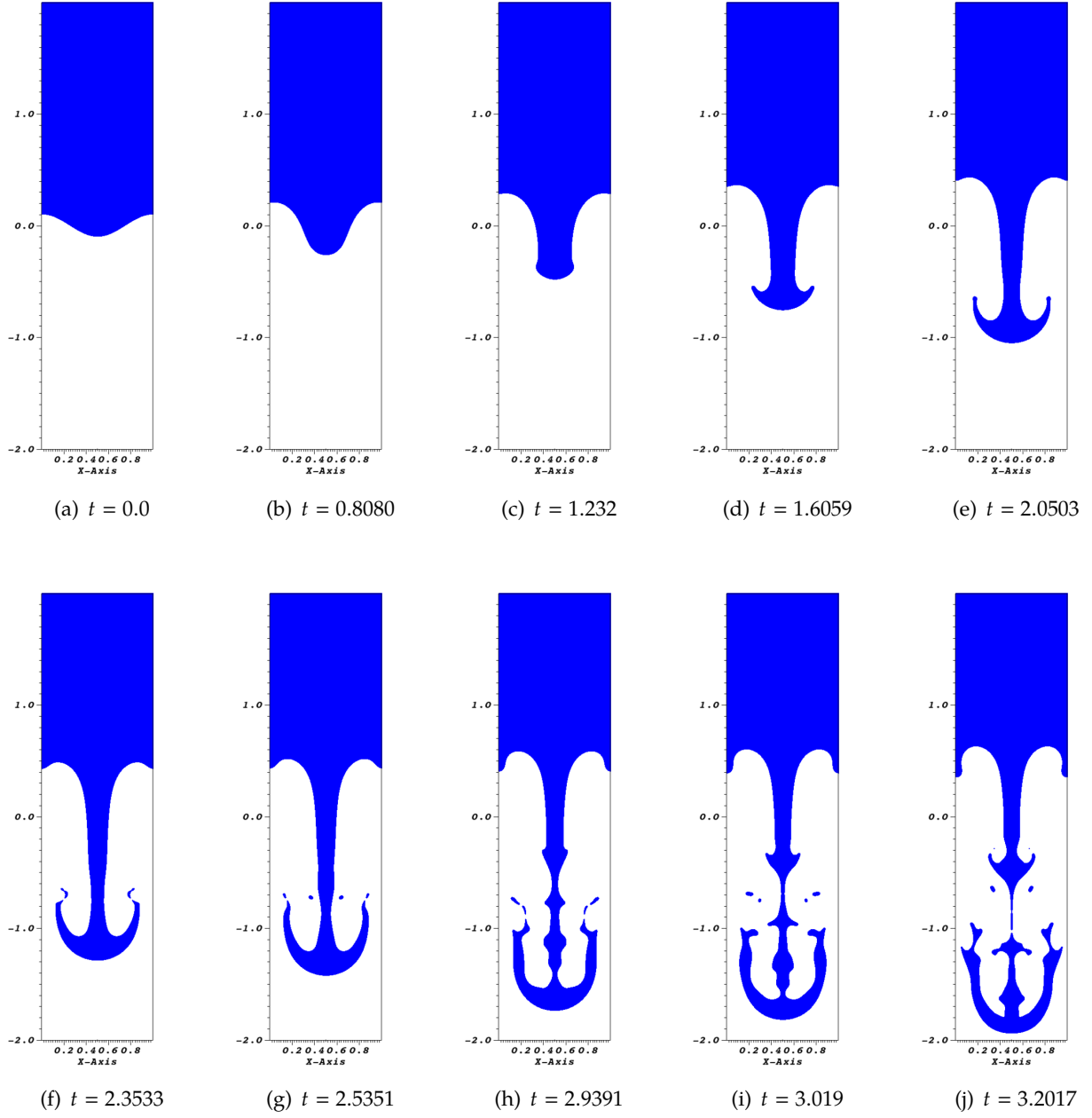


Figure 6: *Rayleigh-Taylor instability in 2D* (section 5.3): Evolution of the interface as a function of time for $At = 0.82$ (density ratio of 0.1).

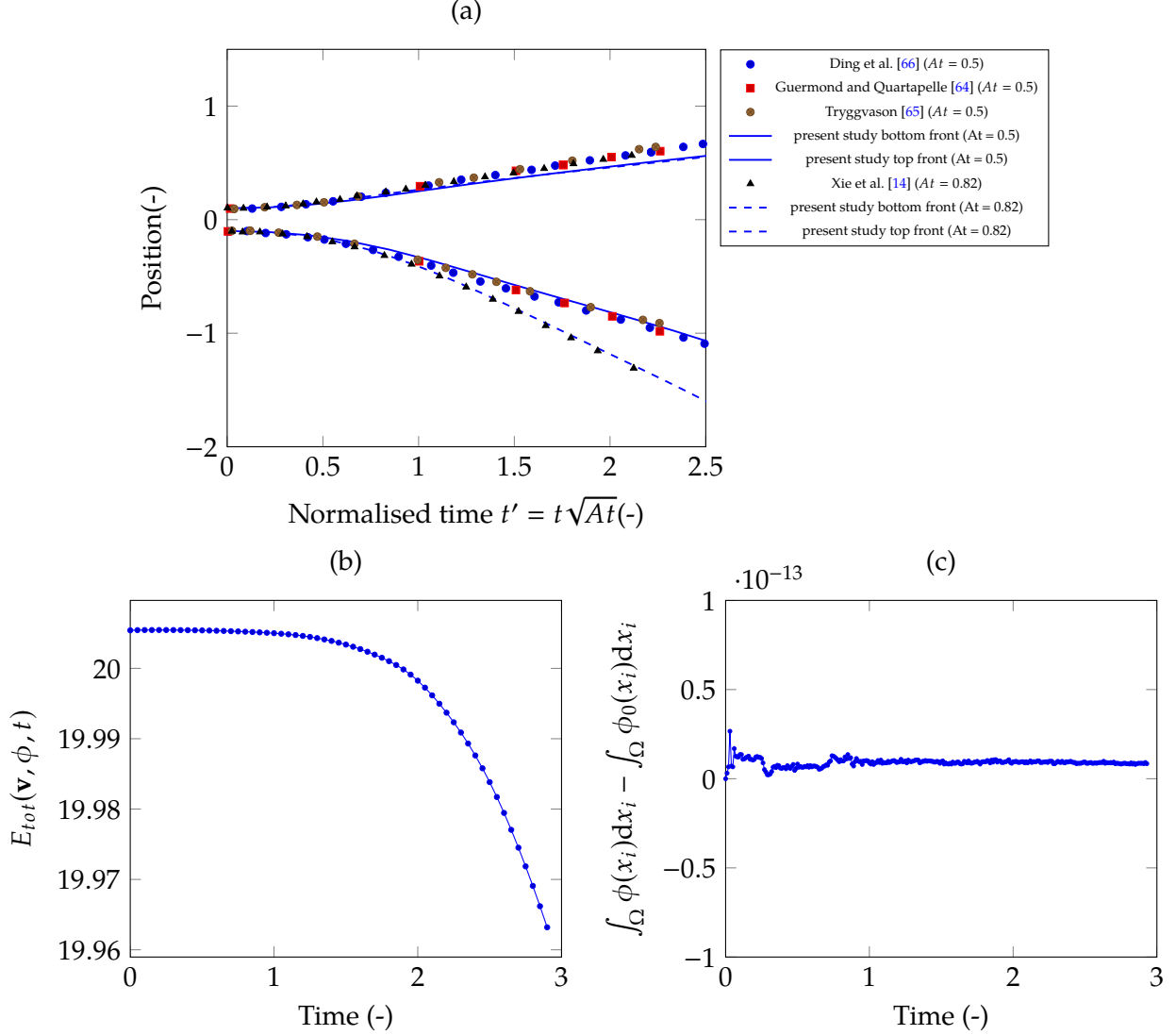


Figure 7: *Rayleigh-Taylor instability 2D* (section 5.3): (a) Comparison of positions of top and bottom front of the interface with literature; (b) decay of the energy functional illustrating theorem 1 for $At = 0.5$; (c) total mass conservation (integral of total ϕ) for $At = 0.5$.

5.4. 3D simulations and comparison with experiments: Single rising bubble

Now that we have shown that our numerical method compares well with other benchmark numerical experiments in the literature, we move to testing the method in comparison to experimental results. We now present results for single rising bubble in 3D with the octree based meshes. We compare these simulations with experimental data presented in the literature. The non-dimensional setting is same as discussed in section 5.2. In all the numerical experiments for single bubble rise we keep the viscosity ratio to be 100. We present numerical experiments with density ratios of 100, 1000, 10000, to show the robustness of the algorithm to large density ratios. See fig. 8 for a schematic of the computational domain selected. The boundary conditions are no-slip on all walls, and zero flux for both μ and ϕ , which are identical to ones used for functions spaces in the proofs. We use the biCGstab (bcgs) linear solver from the PETSc suite along with the Additive Schwarz (ASM) preconditioner for the linear solves in the Newton iterations (see section 3.5). The details of the actual command line arguments used are given in Appendix B.

The convergence criterion for all the 3D bubble rise cases are as follows. For the Navier-Stokes (NS) block we use a relative tolerance of 10^{-6} , and for the Cahn-Hilliard (CH) block the relative tolerance is set to 10^{-8} . The tolerance for block iteration errors is set to 10^{-4} ($\text{block}_{\text{tol}}$ from fig. 1).

From the numerical experiments we can predict the non-dimensional terminal rise velocity u_T of the bubbles as the velocity of the centre of mass of the bubbles. This allows us to calculate Reynolds number based on terminal velocity as $Re_T = Ar \cdot u_T$. Re_T is our first metric for comparison with experiments reported in Bhaga and Weber [67]. The second metric to compare with experiments is chosen to be the terminal shape of the bubble. To show the importance of energy stability, in the cases we present we use a fairly large time-step of 10^{-2} .

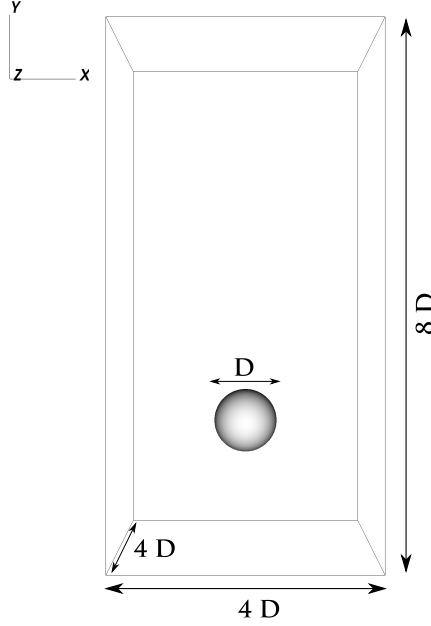


Figure 8: Schematic of the computational domain used for 3D single bubble rise described in section 5.4.

5.4.1. Effect of Cn number

As the model relies on selecting a computationally feasible thickness of the interface, it becomes important to study the effect of Cn (represents the non-dimensional thickness of the interface) on the performance of the model in comparison with the experiments. The model approaches real physics in the limit of $Cn \rightarrow 0$, but as we decrease Cn we need to resolve smaller and smaller length scales. Therefore, decreasing Cahn number requires increasing mesh density, thereby making simulations more and more expensive. One usually selects an 'optimum' Cn_{opt} , such that decreasing Cn beyond this threshold, the quality of the solutions does not change (either measured by comparison with experiments or via lack of change of key quantities of interest). To find this Cn_{opt} number, we conduct three numerical experiments with $Cn = 0.0125$, 0.01 , and 0.0075 . We select the case of $Ar = 13.95$, $We = 116$. fig. 9 shows the results from numerical experiments compared with the experiments for the respective Cn numbers. First of all, we can clearly see that the results show an excellent match with the experimental data, both in terms of shape of the bubble and the terminal Reynolds numbers. An important observation is that there is a small difference between shape of the bubbles between case for $Cn = 0.0125$, and for the case of $Cn = 0.01$. But, there is no noticeable difference in the shape between the cases for $Cn = 0.01$ and $Cn = 0.0075$. This indicates that an asymptotic behavior independent of Cn number is reached and we set $Cn_{opt} = 0.01$. The rest of the numerical experiments presented in the paper for single bubble rising, we use a Cn number of

0.01. The choice of Cn_{opt} allows us to determine the adaptive meshing criterion for the case. We maintain at least 6 elements with the size of $8D/2^{11}$ within the diffuse interface and a very coarse mesh everywhere else with element size of $8D/2^6$. fig. 10 shows the adaptivity of mesh as the air-water interface moves in the domain.

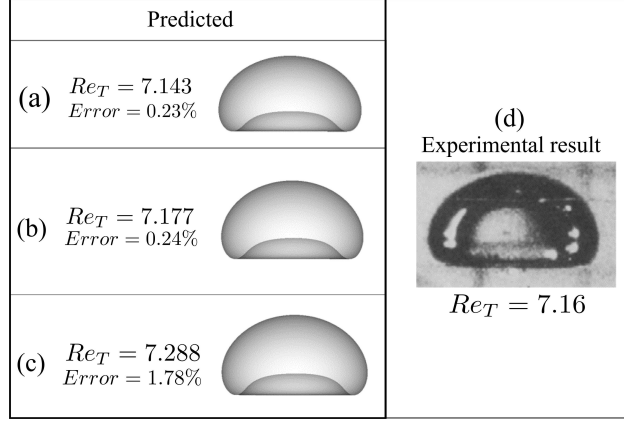


Figure 9: *Effect of Cn number* (section 5.4.1): (a) Bubble shape for $Cn = 0.0125$; (b) bubble shape for $Cn = 0.01$; (c) bubble shape for $Cn = 0.0075$; (d) experimental result from Bhaga and Weber [67].

5.4.2. Effect of density ratio

We now investigate the effect of density ratio. Typically with air-water system we see a density ratio ρ_+/ρ_- (continuous to dispersed) of 1000. We test the algorithm for three density ratios of 10^4 , 10^3 , and 10^2 . Tryggvason et al. [68] reported the effect of density ratios is primarily on the rise velocity of the bubble and the shape does not change after a threshold density ratio is high enough (Tryggvason et al. [68] reported this threshold to be 50). Figure 11 shows the independence of bubble shape for density three density ratios of 10^2 (panel (a)), 10^3 (panel (b)), and 10^4 (panel (c)). We observe that the shape predicted by the simulation for all the density ratios have no variation. Therefore, we see the same independence of bubble shape on density ratio as reported by Tryggvason et al. [68]. We next investigate the effect of density ratio on the temporal variation of bubble rise velocity. fig. 12 shows the temporal evolution of rise velocity of the bubble for three density ratios. It is clear that the difference between the curves is not very high, but the inset plots show that the rise velocity increases as the density ratio is increased. This behavior is reported in multiple studies in the literature [68, 69, 70].

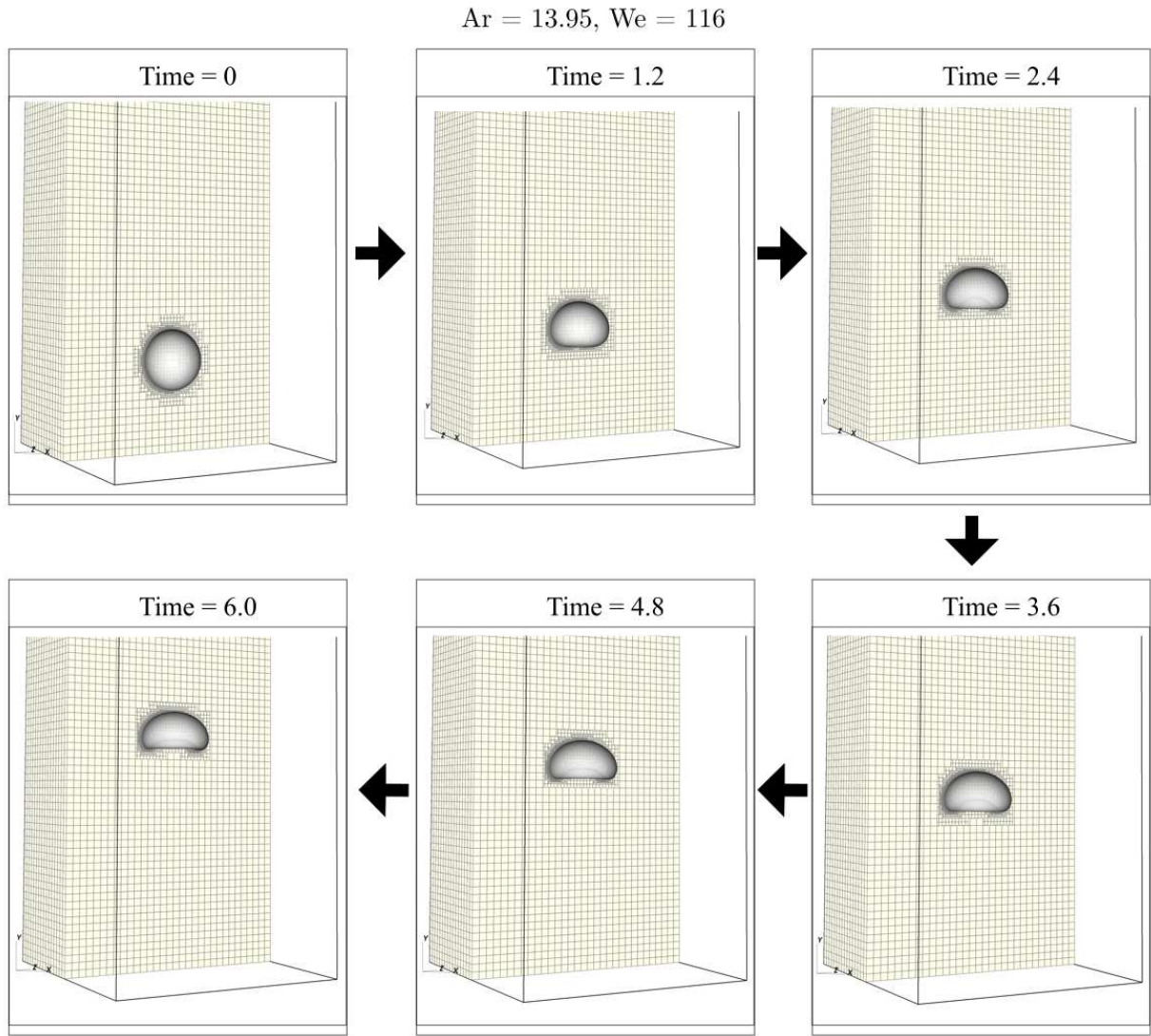


Figure 10: *Evolution of mesh* (section 5.4.1): Snapshots of the mesh at various time-points in the simulation. Only half the mesh of the actual domain is shown in the figure to illustrate the refinement around the air-water interface.

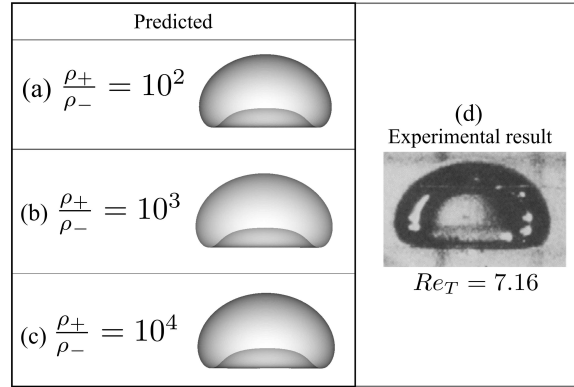


Figure 11: *Effect of density ratio on bubble shape* (section 5.4.2): (a) Bubble shape for $\rho_+/\rho_- = 10^2$; (b) bubble shape for $\rho_+/\rho_- = 10^3$; (c) bubble shape for $\rho_+/\rho_- = 10^4$; (d) experimental result from Bhaga and Weber [67] (reproduced with permission from D. Bhaga, M. Weber, Bubbles in viscous liquids: shapes, wakes and velocities, Journal of fluid Mechanics 105 (1981) 61–85.)

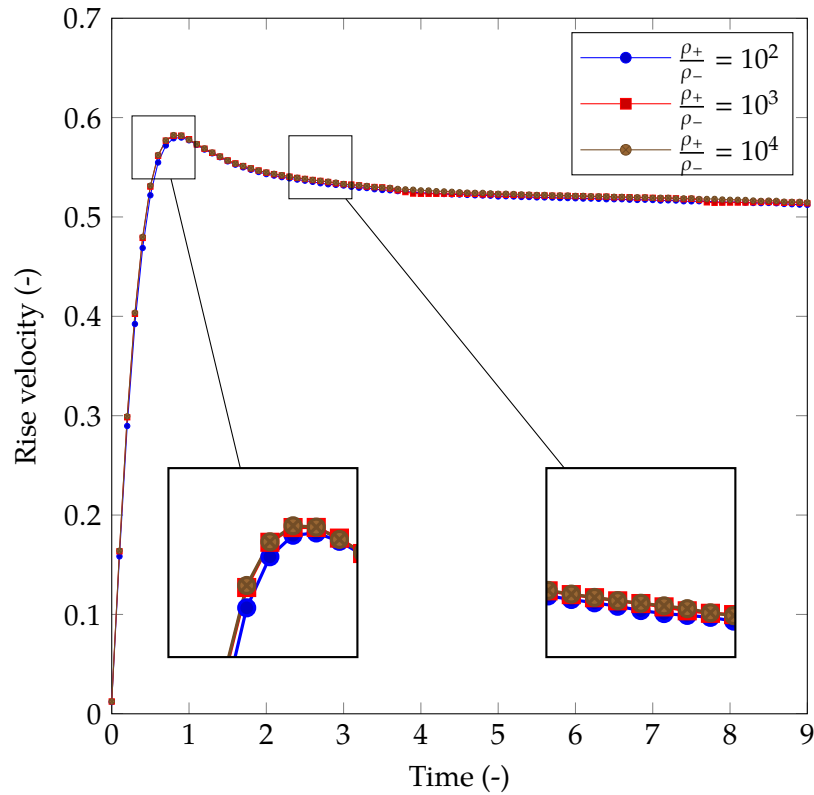


Figure 12: *Effect of density ratio on rise velocity of the bubble* (section 5.4.2).

5.4.3. Comparison with other cases, energy stability

We illustrate our numerical method with two other cases. We select a case where bubble deformation is not very high with $Ar = 6.54$ and $We = 116$, and another case with very high deformation (crowing effect) with $Ar = 30.83$ and $We = 339$. Figure 13 shows comparison of the numerical method with the aforementioned cases. We see an excellent match between simulations

and experiments with errors of less than 3% in Re_T . We emphasize the fact that the mesh is refined only near the interface of the bubble and it is quite coarse everywhere else in the domain, and we are using only linear elements. This shows that the VMS based approximation accurately captures the evolution of the system. This is comparable to recent work by Yan et al. [71] which uses higher order NURBS with levels sets with no adaptive meshing.

We check whether the numerical method follows the theoretical energy stability proved in theorem 1. We present the evolution of the energy functional defined in eq. (9) for the case of $Ar = 6.54$ and $We = 116$. fig. 14 shows the decay of the total energy functional in accordance with the energy stability condition. Similar behavior of the energy functional is seen for all our bubble rise numerical experiments.





Ar = 6.54, We = 116		Ar = 30.89, We = 339	
Experiment		Experiment	
(a)	$Re_T = 2.47$ 	(c)	$Re_T = 18.3$ 
Simulation		Simulation	
(b)	 $Re_T = 2.53$ Error = 2.3%	(d)	 $Re_T = 17.9$ Error = 2.19%

Figure 13: Comparison of the simulations with experiments (section 5.4.3): (a) Experimental terminal shape of the bubble with terminal velocity for $Ar = 6.54$, $We = 116$; (b) terminal bubble shape from simulations for the same conditions as panel (a); (c) experimental terminal shape of the bubble with terminal velocity for $Ar = 30.89$, $We = 339$; (d) terminal bubble shape from simulations for the same conditions as panel (c); (panel (a) and (c) reproduced with permission from D. Bhaga, M. Weber, Bubbles in viscous liquids: shapes, wakes and velocities, Journal of fluid Mechanics 105 (1981) 61–85.)

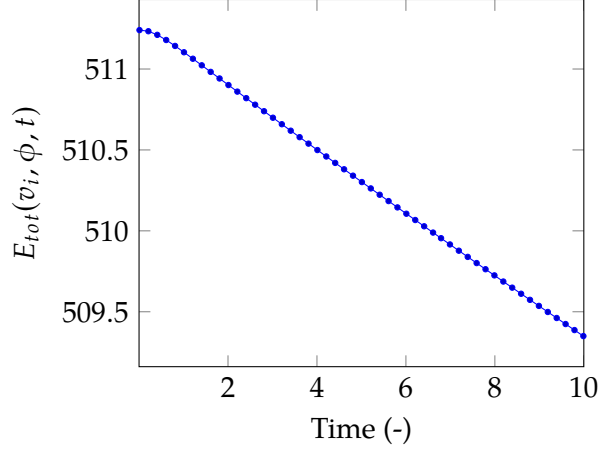


Figure 14: Decay of the energy functional illustrating theorem 1 for the case of $Ar = 6.54$, $We = 116$ (section 5.4.3).

5.5. 3D simulations: Rayleigh-Taylor instability

For the 3D simulations we choose an analytical initial condition for ϕ which governs the interface given by

$$\phi(x_i) = \tanh\left(\frac{(h_0 - x_2) - g(x_i)}{\sqrt{2}Cn}\right), \quad (106)$$

$$g(x_i) = A \exp\left(-\left(\frac{(x_1 - c_1)^2}{\lambda} + \frac{(x_3 - c_3)^2}{\lambda}\right)\right). \quad (107)$$

Here, h_0 is the location in the vertical direction for the interface, in this case chosen to be 2D from the bottom of the channel, x_i is the position vector, c_i is position of the centre of the Gaussian chosen to be $(0.5, 2.1, 0.5)$. λ is the spread of the Gaussian, and A is the amplitude of the Gaussian. See fig. 15 for a schematic of the computational domain selected along with the initial condition of the interface. We use a Cn number of 0.01 and the simulations resolve the large scales very well. We set the Reynolds number at 3000. Further, the same choice of non-dimensionalising scales leads to a Weber number ($We = \rho_c g D^2 / \sigma$). We simulate two different initial conditions. The We number is selected to be 1000. Further, in the 3D simulations we choose the density ratio (ρ_+ / ρ_-) of 0.33. Similarly, ν_+ / ν_- is the viscosity ratio which is selected to be 1.0.

The simulations were performed using a time step of 0.0025. With the refinement near the interface being the finest at $4/2^{10}$ ensuring about 5 elements for resolving the diffuse interface, where as the refinement away from the interface was kept at $4/2^7$. The boundary conditions we use are no-slip for velocity on all the walls and no flux conditions for ϕ and μ . We assume a 90 degree wetting angle for both the fluids. An algebraic multigrid linear solver with additive Schwarz based smoothers is setup for the linear solves in the Newton iterations (see section 3.5). The details of the actual command line arguments used are given in Appendix B.

The convergence criterion for all the 3D Rayleigh-Taylor cases are as follows. For the Navier-Stokes (NS) block we use a relative tolerance of 10^{-6} , and for the Cahn-Hilliard (CH) block the relative tolerance is set to 10^{-8} . For the linear solves within each Newton iteration, for NS we use a relative tolerance of 10^{-7} , and for CH relative tolerance is set to 10^{-7} . The tolerance for block iteration errors is set to 10^{-4} (block_{tol} from fig. 1).

5.5.1. Case 1 : λ of 0.2

The evolution of the interface along with the mesh adaption is shown in fig. 16. Figure 17 shows a qualitative comparison of the interface shape with the shape previously reported for the same density ratio in Tryggvason and Unverdi [62]. Although, the initial conditions for the interface in our case (inverted Gaussian) is different than the initial conditions used in [62] (two-dimensional harmonic wave), the nature of the instability evolving from both of the them is similar where a blob of heavy fluid on top penetrates into light fluid at the bottom, setting up interfacial instabilities. It can be clearly seen from fig. 17 that the shapes at this fairly evolved times are quite similar to each other qualitatively.

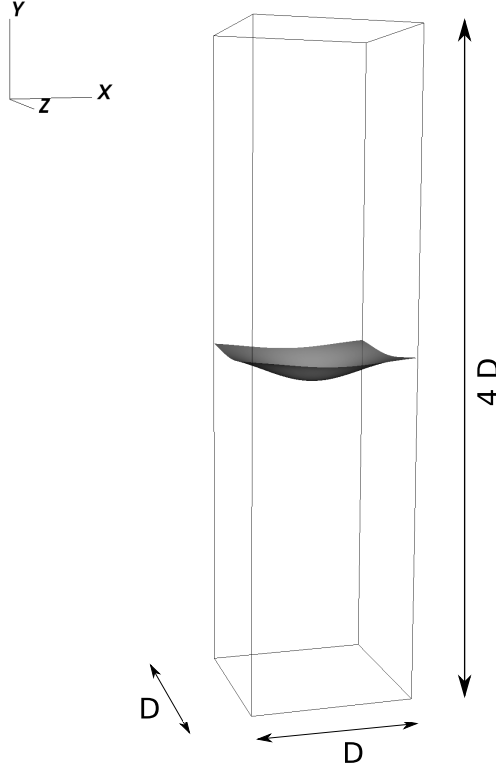


Figure 15: Schematic of the computational domain used for Rayleigh-Taylor instability (section 5.5) with the iso-surface $\phi = 0$ showing the initial condition of the interface.

The initial perturbation of the interface (quite similar to that of [62]) is chosen here such that the front of the heavy fluid penetrates into the light fluid, making the interface buckle. It can be clearly seen in the evolution in fig. 16 that the sides of the interface clinging to the wall maintain a 90 degree angle as they rise to compensate for the motion of the centre front downwards. Tryggvason and Unverdi [62] report that two counter rotating vortical structures are formed at the initial position of the interface propagate into the light fluid as vortices advance in with the blob. We also see a similar behavior in our simulations; fig. 18 show these two counter rotating vortices colored in blue. As the fluid interface moves down in the centre, the lighter fluid is displaced and moves rapidly in near the walls going towards the corner setting off two counter rotating vortices near the wall. These counter-rotating vortices are shown in red color in fig. 18. The same behavior was reported in Tryggvason and Unverdi [62]. It is important to note that the simulation presented in this study is not highly resolved as Cn here is 0.01 (which results in a mesh of about 3.5 million elements). While we have performed simulations with higher resolution (14 million elements for $Cn = 0.0075$), we

emphasize that a coarse resolution is able to resolve most of the physics reported in the literature.

$$Re = 3000, \quad We = 1000, \quad \lambda = 0.2$$

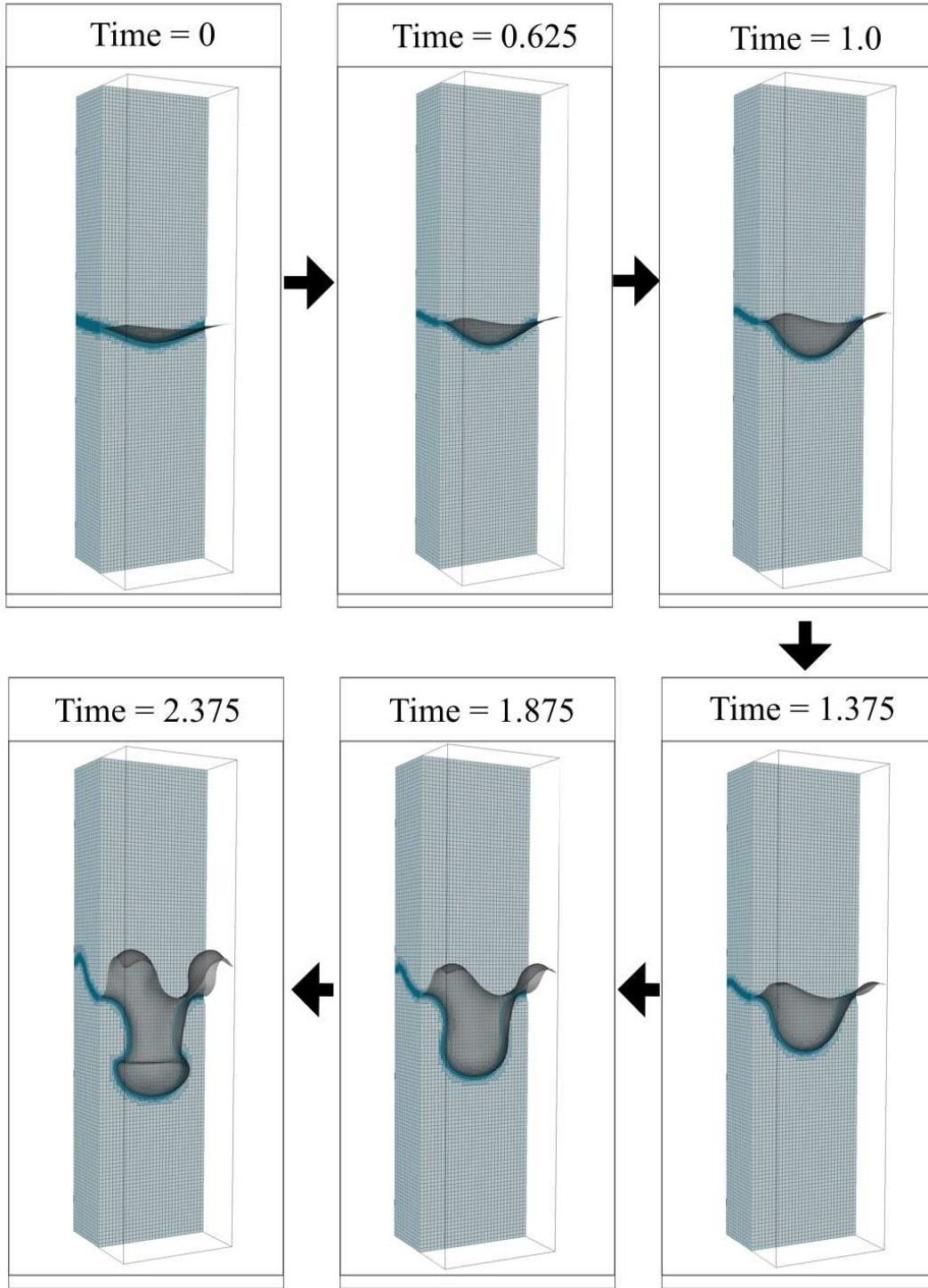


Figure 16: *Evolution of mesh*: Snapshots of the mesh at various time-points in the simulation for Rayleigh-Taylor instability (section 5.5) for $\lambda = 0.2$. Only half the mesh of the actual domain is shown in the figure to illustrate the refinement around the interface of two fluids.

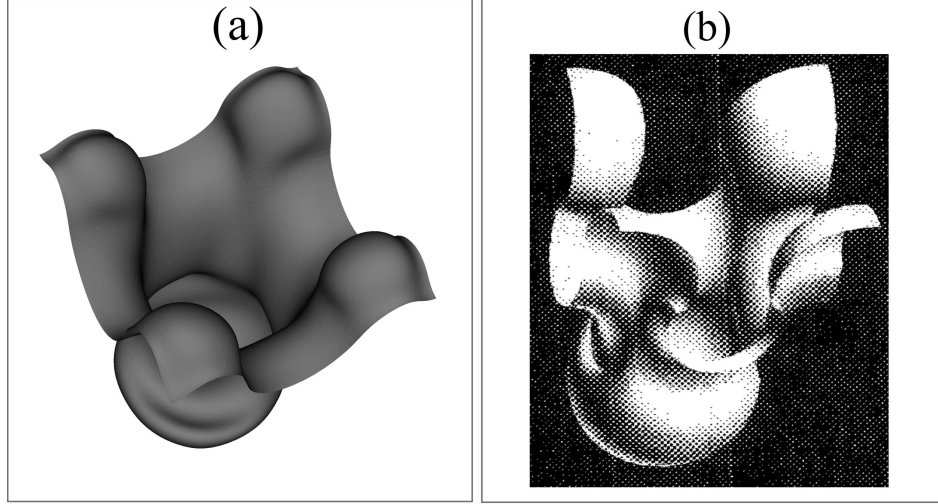


Figure 17: *Qualitative comparison with previous literature* (section 5.5): (a) Interface shape from current simulation at non-dimensional time 2.37; (b) interface shape reported in Tryggvason and Unverdi [62] at $t = 3.0$ (Reproduced from [G. Tryggvason, S. O. Unverdi, Computations of three-dimensional Rayleigh-Taylor instability, Physics of Fluids A: Fluid Dynamics 2 (5) (1990) 656–659], with the permission of AIP Publishing).

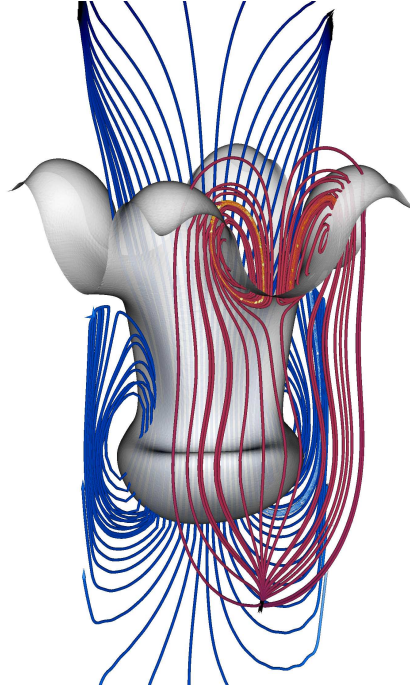


Figure 18: *Streamlines drawn on top of the interface* (section 5.5): Streamlines illustrating the vortical structures in Rayleigh-Taylor instability. The blue streamlines show the rollup of interface near the leading end of the interface. The red-orange streamlines show the roll up of interface near the boundaries.

5.5.2. Case 2 : λ of 0.08

For this case we keep all the parameters the same as the case 1 except the λ is decreased to 0.08. The evolution of the interface is shown in fig. 19. In this particular case we let the interface develop more to observe roll up and shedding at non-dimensional time $t = 2.875$. A smaller λ in the initial conditions allows for a much flatter initial profile of the interface at the wall, but a deeper

penetration at the centre. If we compare the evolution of the interface shape for the case of $\lambda = 0.2$ (fig. 16) and for the case of $\lambda = 0.08$ (fig. 19), we observe that similar shapes are observed much sooner for the case of $\lambda = 0.08$. For example, the shape of the interface at $t = 2.375$ in the case of $\lambda = 0.2$ is similar to the shape of interface at $t = 1.875$ near the center.

Just like for the case of bubble rise, we check the behavior of the energy functional to observe whether energy stability is followed. We present the evolution of the energy functional defined in eq. (9). Figure 20 shows the decay of the total energy functional in accordance with the energy stability condition. Similar behavior of the energy functional is also seen for the case of $\lambda = 0.2$.

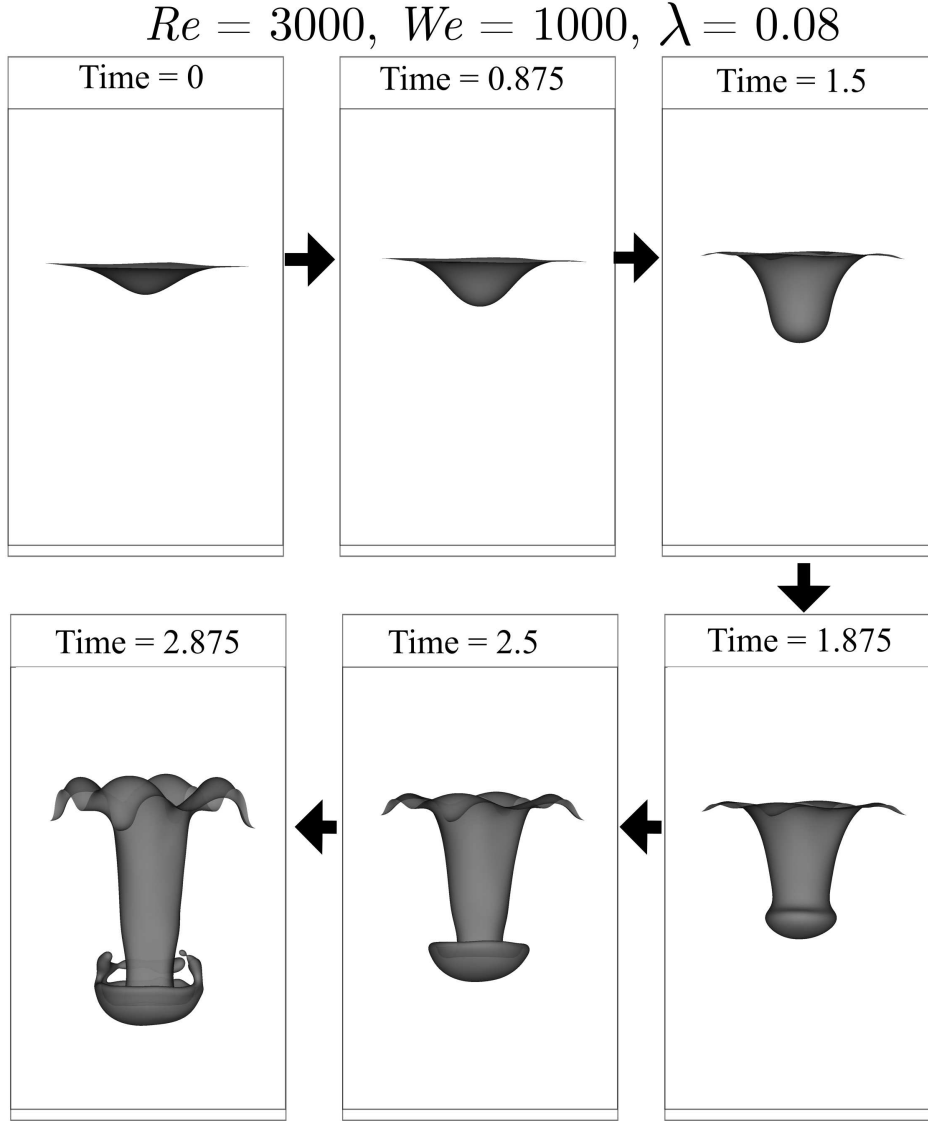


Figure 19: *Evolution of the interface* (section 5.5): Snapshots of the interface at various time-points in the simulation for Rayleigh-Taylor instability for $\lambda = 0.08$.

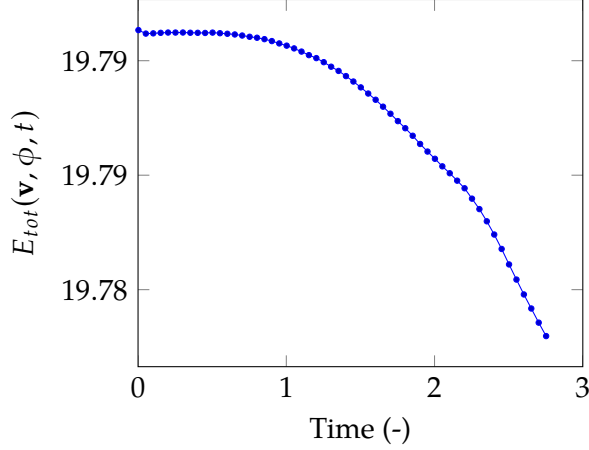


Figure 20: Decay of the energy functional illustrating theorem 1 for the case of $Re = 3000$ and $We = 1000$ in the simulation of the 3D Rayleigh-Taylor instability (section 5.5).

6. Scaling of the numerical implementation

We perform scaling analysis to demonstrate scaling and parallelization of the framework. All scaling tests were performed on TACC Stampede2 using the Knights Landing processors ($p = 136, \dots, 17408$). We used the bubble rise case in section 5.4 as a sample case for the scaling analysis with $Ar = 13.95$ and $We = 116$. The bubble rise case for each scaling experiment is run for 5 time-steps so that any deviations from the long time behavior (timing of convergence in non-linear solves) in the initial time-steps does not dominate the timing. We adaptively refine the mesh around the interface of the sphere five levels deeper than the rest of the background mesh. The mesh is defined by a pair of minimum refinement C and maximum refinement R , where the background mesh element size ranges from $8/2^C$ to $8/2^R$ at the interface. We run this experiment on four background/interface refinement levels: 5/10, 6/11, 7/12, 8/13. Each refinement level has roughly seven to eight times more degrees of freedom to solve for than the previous level, with 5/10 having around 800,000 degrees of freedom and 8/13 reaching 138 million degrees of freedom.

We note that given specific C and R and the same initial conditions, the overall problem size in spite of mesh-refinement is consistent independent of the number of processes being used for the simulation. To this effect, we believe presenting performance for different C/R combinations for different number of processes in the style of a strong scaling is appropriate. For the same initial conditions, non-dimensional numbers, and a specific choice of refinement levels (C and R), the problem is consistent independent of the number of processes being used, which allows us to use strong scaling type analysis. Therefore, we vary the number of processes for each combination of C and R and present the timing information. Figure 21 shows the strong scaling analysis, and it can be seen that c code scales well, with continuing reductions in time-to-solve. Performing weak scaling for our case is harder because of mesh refinements, and subsequently the change in problem size. Therefore, we derive the weak-scalability from a set of strong scaling experiment. We connect the points which roughly have the same number of elements per process to achieve this. Figure 22 shows weak scaling with curves being dashed lines for weak scaling, with the aforementioned approximation.

From figs. 21 and 22 we observe that the numerical framework shows very good strong and weak scaling.

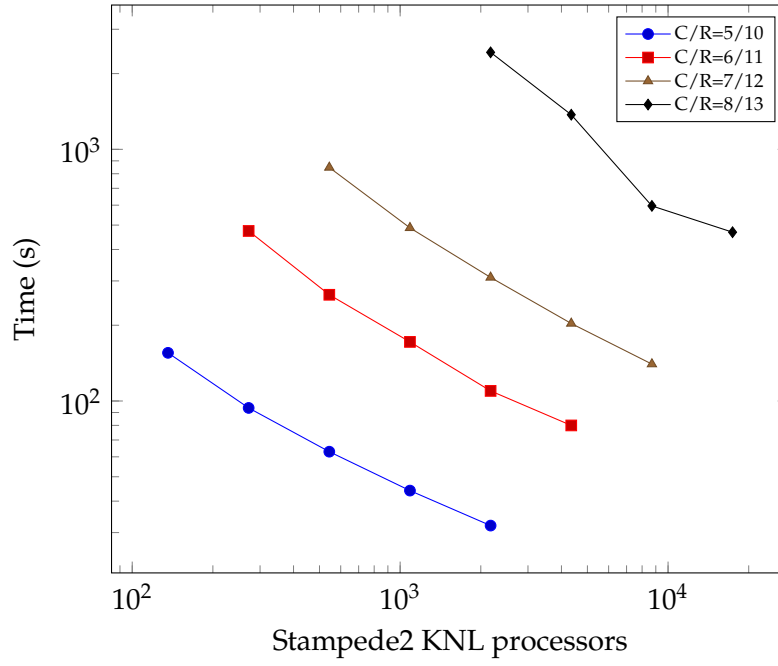


Figure 21: Total time to solve five timesteps (including remeshing) for varying refinement configurations C/R for a bubble rise in a channel. The setup is identical to the case selected in section 5.4 with the domain being the one presented in figure 8.

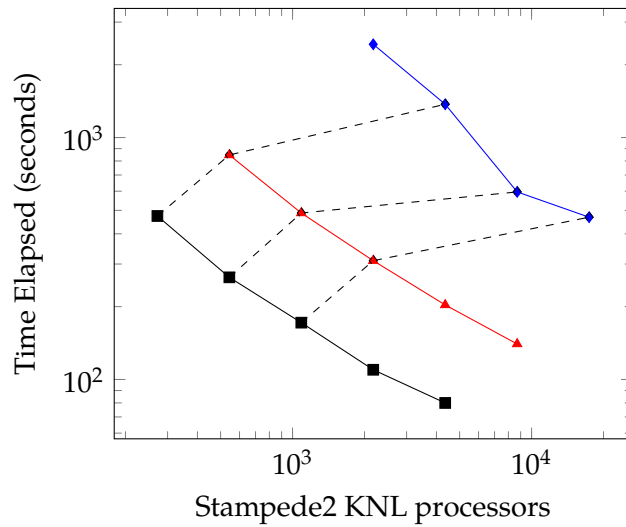


Figure 22: *Weak scalability approximated from multiple strong-scaling experiments*: We approximate the weak (dashed lines) scaling from the strong (solid lines) scaling results for $r = (6/11, 7/12, 8/13)$ and p up to 17408 on Stampede2 Knights Landing processors. Connecting the points which have same approximately same number of elements per process.

7. Conclusions and future work

We have reported on a continuous Galerkin (cG) based framework to simulate two-phase flows with the thermodynamically consistent Cahn-Hilliard Navier-Stokes model. We present rigorous proofs of energy stability for the implicit time scheme that we have selected. We also present an existence result for our system, particularly studying the advective Cahn-Hilliard operator. A variational multi-scale approach is used to model momentum equations and provide grad-div stabilisation for the proposed cG method. The continuous model is discretized in space using a cG method with a massively parallel adaptive meshing framework called DENDRO. Extensive numerical experiments were carried out to test the accuracy of the numerical model. The numerical model was validated against experimental datasets for an extreme density ratio (100 to 10000) and showed excellent agreement with the experimental results. We show that the model performs as good or better in comparison with front-tracking or level set models. We demonstrated that the fully discretized numerical scheme also follows the energy stability and mass conservation proved for the semi-discrete form of the model. Further, we used the model to simulate a turbulent case of Rayleigh-Taylor instability and the results presented show that the model resolves most of the physics reported in the literature using front tracking models. We carried out extensive scaling tests of the numerical framework and show excellent weak and strong scaling till about 17000 MPI processes.

We identify several avenues for future work. One critical aspect is related to practical applications of the CH-NS model, which require 3D simulations across long time horizons. As reported here, adaptive mesh refinement (AMR) provides an efficient strategy to model practical applications. AMR requires interpolating fields from a mesh at the previous time step to an updated mesh at the current time step. Care has to be taken to ensure that these interpolation schemes are also mass-conserving. In the current work, we see that the coarsening step (where eight daughter cells are replaced by one larger parent cell) could potentially not conserve mass. This suggests deployment of mass-conserving interpolation schemes, which is the focus of our subsequent work.

Another avenue of work is to extend the order of the basis function to consider higher order cG spaces. Higher order methods are useful on two fronts: (1) they improve the overall quality of the solutions and better enforce the solenoidality of mixture velocity; and (2) they also decrease the disparity in the largest and smallest scales for low Reynolds number applications where the disparity in length scales is only because the interface needs to be resolved with a high density of fine elements. This will help speed up the framework for optimization applications targeted towards micro-fluidics. We are currently working on developing a fully coupled solver instead of the block iteration approach presented in this paper. The fully coupled approach will be faster because of less number of matrix assemblies. In the current paper the mesh is only refined near the interface (interface scales), we are working on developing *a posteriori* estimates to refine the mesh based on both interface and velocity scales. This will help resolve wakes and boundary layers much better in many applications involving turbulence.

8. Acknowledgements

The authors acknowledge XSEDE grant number TG-CTS110007 for computing time on TACC Stampede2, ALCF computing resources and Iowa State University computing resources. JAR was supported in part by NSF Grant DMS-1620128. BG, AL and MAK was funded in part by NSF grant 1935255, 1855902. HS was funded in part by NSF grant 1912930.

References

- [1] P. K. Notz, O. A. Basaran, Dynamics and breakup of a contracting liquid filament, *Journal of Fluid Mechanics* 512 (2004) 223–256.
- [2] S. Osher, R. Fedkiw, *Level Set Methods and Dynamic Implicit Surfaces*, vol. 153 of *Applied Mathematical Sciences*, Springer, 2003.
- [3] S. O. Unverdi, G. Tryggvason, A front-tracking method for viscous, incompressible, multi-fluid flows, *Journal of Computational Physics* 100 (1) (1992) 25–37.
- [4] J. U. Brackbill, D. B. Kothe, C. Zemach, A continuum method for modeling surface tension, *Journal of Computational Physics* 100 (2) (1992) 335–354.
- [5] A. Prosperetti, G. Tryggvason, *Computational Methods for Multiphase Flow*, Cambridge University Press, 2009.
- [6] D. Jacqmin, An energy approach to the continuum surface tension method, in: 34th AIAA Aerospace Sciences Meeting & Exhibit, vol. AIAA96, American Institute of Aeronautics and Astronautics, Reno, Nevada, USA, 0858, 1996.
- [7] D. Jacqmin, Contact-line dynamics of a diffuse fluid interface, *Journal of Fluid Mechanics* 402 (2000) 57–88, [doi:10.1017/S0022112099006874](https://doi.org/10.1017/S0022112099006874).
- [8] D. M. Anderson, G. B. McFadden, A. A. Wheeler, Diffuse-interface methods in fluid mechanics, *Annual Review of Fluid Mechanics* 30 (1) (1998) 139–165, ISSN 0066-4189, [doi:10.1146/annurev.fluid.30.1.139](https://doi.org/10.1146/annurev.fluid.30.1.139).
- [9] Z. Guo, P. Lin, J. Lowengrub, S. M. Wise, Mass conservative and energy stable finite difference methods for the quasi-incompressible Navier–Stokes–Cahn–Hilliard system: Primitive variable and projection-type schemes, *Computer Methods in Applied Mechanics and Engineering* 326 (2017) 144–174, ISSN 00457825, [doi:10.1016/j.cma.2017.08.011](https://doi.org/10.1016/j.cma.2017.08.011).
- [10] M. Shokrpour Roudbari, G. Şimşek, E. H. van Brummelen, K. G. van der Zee, Diffuse-interface two-phase flow models with different densities: A new quasi-incompressible form and a linear energy-stable method, *Mathematical Models and Methods in Applied Sciences* 28 (04) (2018) 733–770, [doi:10.1142/S0218202518500197](https://doi.org/10.1142/S0218202518500197).
- [11] P. Hohenberg, B. Halperin, Theory of dynamic critical phenomena, *Reviews of Modern Physics* 49 (3) (1977) 435–479, ISSN 0034-6861, [doi:10.1103/RevModPhys.49.435](https://doi.org/10.1103/RevModPhys.49.435).
- [12] W. Villanueva, G. Amberg, Some generic capillary-driven flows, *International Journal of Multiphase Flow* 32 (9) (2006) 1072–1086.
- [13] S. Dong, An efficient algorithm for incompressible N-phase flows, *Journal of Computational Physics* 276 (2014) 691–728, ISSN 10902716, [doi:10.1016/j.jcp.2014.08.002](https://doi.org/10.1016/j.jcp.2014.08.002).
- [14] Y. Xie, O. Wodo, B. Ganapathysubramanian, Incompressible two-phase flow: Diffuse interface approach for large density ratios, grid resolution study, and 3D patterned substrate wetting problem, *Computers and Fluids* 141 (2015) 223–234, ISSN 00457930, [doi:10.1016/j.compfluid.2016.04.011](https://doi.org/10.1016/j.compfluid.2016.04.011).

- [15] M. E. Gurtin, D. Polignone, J. Vinals, Two-phase binary fluids and immiscible fluids described by an order parameter, *Mathematical Models and Methods in Applied Sciences* 6 (06) (1996) 815–831.
- [16] H. Abels, H. Garcke, G. Grün, Thermodynamically consistent, frame indifferent diffuse interface models for incompressible two-phase flows with different densities, *Mathematical Models and Methods in Applied Sciences* 22 (03) (2012) 1150013.
- [17] J. Volker, *Finite Element Methods for Incompressible Flow Problems*, vol. 51 of *Springer Series in Computational Mathematics Book*, Springer, 2016.
- [18] C. Burstedde, L. C. Wilcox, O. Ghattas, p4est: Scalable algorithms for parallel adaptive mesh refinement on forests of octrees, *SIAM Journal on Scientific Computing* 33 (3) (2011) 1103–1133.
- [19] H. Sundar, R. S. Sampath, S. S. Adavani, C. Davatzikos, G. Biros, Low-constant parallel algorithms for finite element simulations using linear octrees, in: *Proceedings of the 2007 ACM/IEEE conference on Supercomputing*, ACM, 25, 2007.
- [20] H. Sundar, R. S. Sampath, G. Biros, Bottom-up construction and 2: 1 balance refinement of linear octrees in parallel, *SIAM Journal on Scientific Computing* 30 (5) (2008) 2675–2708.
- [21] J. Kim, K. Kang, J. Lowengrub, Conservative multigrid methods for Cahn–Hilliard fluids, *Journal of Computational Physics* 193 (2) (2004) 511–543, ISSN 00219991, doi:10.1016/j.jcp.2003.07.035.
- [22] X. Feng, Fully Discrete Finite Element Approximations of the Navier–Stokes–Cahn–Hilliard Diffuse Interface Model for Two-Phase Fluid Flows, *SIAM Journal on Numerical Analysis* 44 (3) (2006) 1049–1072, ISSN 0036-1429, doi:10.1137/050638333.
- [23] D. Han, X. Wang, A second order in time, uniquely solvable, unconditionally stable numerical scheme for Cahn–Hilliard–Navier–Stokes equation, *Journal of Computational Physics* 290 (2015) 139–156, ISSN 00219991, doi:10.1016/j.jcp.2015.02.046.
- [24] J. Shen, X. Yang, A Phase-Field Model and Its Numerical Approximation for Two-Phase Incompressible Flows with Different Densities and Viscosities, *SIAM Journal on Scientific Computing* 32 (3) (2010) 1159–1179, ISSN 1064-8275, doi:10.1137/09075860X.
- [25] J. Shen, X. Yang, Energy stable schemes for Cahn–Hilliard phase-field model of two-phase incompressible flows, *Chinese Annals of Mathematics, Series B* 31 (5) (2010) 743–758, ISSN 0252-9599, doi:10.1007/s11401-010-0599-y.
- [26] Y. Chen, J. Shen, Efficient, adaptive energy stable schemes for the incompressible Cahn–Hilliard Navier–Stokes phase-field models, *Journal of Computational Physics* 308 (2016) 40–56, ISSN 00219991, doi:10.1016/j.jcp.2015.12.006.
- [27] J. Shen, J. Xu, J. Yang, The scalar auxiliary variable (SAV) approach for gradient flows, *Journal of Computational Physics* 353 (2018) 407–416.
- [28] G. Zhu, H. Chen, J. Yao, S. Sun, Efficient energy-stable schemes for the hydrodynamics coupled phase-field model, *Applied Mathematical Modelling* 70 (2019) 82–108.
- [29] T. J. Hughes, L. Mazzei, K. E. Jansen, Large eddy simulation and the variational multiscale method, *Computing and Visualization in Science* 3 (1-2) (2000) 47–59.

- [30] N. Ahmed, T. Chacón Rebollo, V. John, S. Rubino, A Review of Variational Multiscale Methods for the Simulation of Turbulent Incompressible Flows, *Archives of Computational Methods in Engineering* 24 (1) (2017) 115–164, ISSN 1886-1784, [doi:10.1007/s11831-015-9161-0](https://doi.org/10.1007/s11831-015-9161-0).
- [31] Y. Bazilevs, V. Calo, J. Cottrell, T. Hughes, A. Reali, G. Scovazzi, Variational multiscale residual-based turbulence modeling for large eddy simulation of incompressible flows, *Computer Methods in Applied Mechanics and Engineering* 197 (1-4) (2007) 173–201.
- [32] T. Coupez, E. Hachem, Solution of high-Reynolds incompressible flow with stabilized finite element and adaptive anisotropic meshing, *Computer Methods in Applied Mechanics and Engineering* 267 (2013) 65–85, ISSN 00457825, [doi:10.1016/j.cma.2013.08.004](https://doi.org/10.1016/j.cma.2013.08.004).
- [33] E. Hachem, S. Feghali, R. Codina, T. Coupez, Anisotropic adaptive meshing and monolithic Variational Multiscale method for fluid-structure interaction, *Computers and Structures* 122 (2013) 88–100, ISSN 00457949, [doi:10.1016/j.compstruc.2012.12.004](https://doi.org/10.1016/j.compstruc.2012.12.004).
- [34] E. Hachem, M. Khalloufi, J. Bruchon, R. Valette, Y. Mesri, Unified adaptive Variational MultiScale method for two phase compressible-incompressible flows, *Computer Methods in Applied Mechanics and Engineering* 308 (2016) 238–255, ISSN 00457825, [doi:10.1016/j.cma.2016.05.022](https://doi.org/10.1016/j.cma.2016.05.022).
- [35] A. M. Khokhlov, Fully threaded tree algorithms for adaptive refinement fluid dynamics simulations, *Journal of Computational Physics* 143 (2) (1998) 519–543.
- [36] G. Zhu, J. Kou, B. Yao, Y.-s. Wu, J. Yao, S. Sun, Thermodynamically consistent modelling of two-phase flows with moving contact line and soluble surfactants, *Journal of Fluid Mechanics* 879 (2019) 327–359.
- [37] G. Zhu, J. Kou, J. Yao, A. Li, S. Sun, A phase-field moving contact line model with soluble surfactants, *Journal of Computational Physics* 405 (2020) 109170.
- [38] F. Magaletti, F. Picano, M. Chinappi, L. Marino, C. M. Casciola, The sharp-interface limit of the Cahn–Hilliard/Navier–Stokes model for binary fluids, *Journal of Fluid Mechanics* 714 (2013) 95–126, [doi:10.1017/jfm.2012.461](https://doi.org/10.1017/jfm.2012.461).
- [39] P. Yue, C. Zhou, J. Feng, Sharp-interface limit of the Cahn–Hilliard model for moving contact lines, *Journal of Fluid Mechanics* 645 (2010) 279–294, ISSN 0022-1120, [doi:10.1017/S0022112009992679](https://doi.org/10.1017/S0022112009992679).
- [40] J. Shen, X. Yang, Numerical approximations of Allen–Cahn and Cahn–Hilliard equations, *Discrete Contin. Dyn. Syst* 28 (4) (2010) 1669–1691.
- [41] P. G. Ciarlet, *Linear and Nonlinear Functional Analysis with Applications*, Society for Industrial and Applied Mathematics, Philadelphia, PA, USA, ISBN 1611972582, 9781611972580, 2013.
- [42] E. Zeidler, *Functional Analysis and its Applications, Part II/B (Nonlinear Monotone Operators)* Springer, Berlin .
- [43] W. Liu, Existence and uniqueness of solutions to nonlinear evolution equations with locally monotone operators, *Nonlinear Analysis: Theory, Methods & Applications* 74 (18) (2011) 7543–7561.

- [44] J. T. Oden, J. N. Reddy, *An Introduction to the Mathematical Theory of Finite Elements*, Dover, 2011.
- [45] A. Brooks, T. Hughes, Streamline upwind/Petrov-Galerkin formulations for convection dominated flows with particular emphasis on the incompressible Navier-Stokes equations, *Computer Methods in Applied Mechanics and Engineering* 32 (1982) 199–259.
- [46] T. Tezduyar, S. Mittal, S. Ray, R. Shih, Incompressible flow computations with stabilized bilinear and linear equal-order-interpolation velocity-pressure elements, *Computer Methods in Applied Mechanics and Engineering* 95 (1992) 221–242.
- [47] T. J. Hughes, G. Scovazzi, L. P. Franca, Multiscale and stabilized methods, *Encyclopedia of Computational Mechanics Second Edition* (2018) 1–64.
- [48] T. J. Hughes, Multiscale phenomena: Green’s functions, the Dirichlet-to-Neumann formulation, subgrid scale models, bubbles and the origins of stabilized methods, *Computer Methods in Applied Mechanics and Engineering* 127 (1-4) (1995) 387–401.
- [49] S. Balay, W. D. Gropp, L. C. McInnes, B. F. Smith, Efficient Management of Parallelism in Object Oriented Numerical Software Libraries, in: E. Arge, A. M. Bruaset, H. P. Langtangen (Eds.), *Modern Software Tools in Scientific Computing*, Birkhäuser Press, 163–202, 1997.
- [50] S. Balay, S. Abhyankar, M. F. Adams, J. Brown, P. Brune, K. Buschelman, L. Dalcin, A. Dener, V. Eijkhout, W. D. Gropp, D. Karpeyev, D. Kaushik, M. G. Knepley, D. A. May, L. C. McInnes, R. T. Mills, T. Munson, K. Rupp, P. Sanan, B. F. Smith, S. Zampini, H. Zhang, H. Zhang, PETSc Web page, <https://www.mcs.anl.gov/petsc>, 2019.
- [51] S. Balay, S. Abhyankar, M. F. Adams, J. Brown, P. Brune, K. Buschelman, L. Dalcin, A. Dener, V. Eijkhout, W. D. Gropp, D. Karpeyev, D. Kaushik, M. G. Knepley, D. A. May, L. C. McInnes, R. T. Mills, T. Munson, K. Rupp, P. Sanan, B. F. Smith, S. Zampini, H. Zhang, H. Zhang, PETSc Users Manual, Tech. Rep. ANL-95/11 - Revision 3.11, Argonne National Laboratory, 2019.
- [52] H. Sundar, R. Sampath, G. Biros, Bottom-up construction and 2:1 balance refinement of linear octrees in parallel, *SIAM Journal on Scientific Computing* 30 (5) (2008) 2675–2708, [doi:10.1137/070681727](https://doi.org/10.1137/070681727).
- [53] H. Sundar, R. S. Sampath, S. S. Adavani, C. Davatzikos, G. Biros, Low-constant Parallel Algorithms for Finite Element Simulations using Linear Octrees, in: *SC’07: Proceedings of the International Conference for High Performance Computing, Networking, Storage, and Analysis*, ACM/IEEE, 1–12, 2007.
- [54] M. Fernando, D. Duplyakin, H. Sundar, Machine and application aware partitioning for adaptive mesh refinement applications, in: *Proceedings of the 26th International Symposium on High-Performance Parallel and Distributed Computing*, 231–242, 2017.
- [55] M. Bern, D. Eppstein, S.-H. Teng, Parallel construction of quadrees and quality triangulations, *International Journal of Computational Geometry & Applications* 9 (6) (1999) 517–532.
- [56] C. Burstedde, L. C. Wilcox, O. Ghattas, p4est: Scalable Algorithms for Parallel Adaptive Mesh Refinement on Forests of Octrees, *SIAM Journal on Scientific Computing* 33 (3) (2011) 1103–1133, [doi:10.1137/100791634](https://doi.org/10.1137/100791634).

- [57] D. E. Knuth, The Art of Computer Programming. Volume III. Searching and Sorting, The Art of Computer Programming, Addison-Wesley, ISBN 020103803, URL <http://www.worldcat.org/isbn/020103803>, 1973.
- [58] H. Sundar, G. Biros, C. Burstedde, J. Rudi, O. Ghattas, G. Stadler, Parallel Geometric-algebraic Multigrid on Unstructured Forests of Octrees, in: Proceedings of the International Conference on High Performance Computing, Networking, Storage and Analysis, SC '12, IEEE Computer Society Press, Los Alamitos, CA, USA, ISBN 978-1-4673-0804-5, 43:1–43:11, URL <http://dl.acm.org/citation.cfm?id=2388996.2389055>, 2012.
- [59] S.-R. Hysing, S. Turek, D. Kuzmin, N. Parolini, E. Burman, S. Ganesan, L. Tobiska, Quantitative benchmark computations of two-dimensional bubble dynamics, *International Journal for Numerical Methods in Fluids* 60 (11) (2009) 1259–1288.
- [60] S. Aland, A. Voigt, Benchmark computations of diffuse interface models for two-dimensional bubble dynamics, *International Journal for Numerical Methods in Fluids* 69 (3) (2012) 747–761, doi:10.1002/fld.2611, URL <http://doi.wiley.com/10.1002/fld.2611>.
- [61] H. Z. Yuan, Z. Chen, C. Shu, Y. Wang, X. D. Niu, S. Shu, A free energy-based surface tension force model for simulation of multiphase flows by level-set method, *Journal of Computational Physics* 345 (2017) 404–426, ISSN 10902716, doi:10.1016/j.jcp.2017.05.020, URL <http://dx.doi.org/10.1016/j.jcp.2017.05.020>.
- [62] G. Tryggvason, S. O. Unverdi, Computations of three-dimensional Rayleigh–Taylor instability, *Physics of Fluids A: Fluid Dynamics* 2 (5) (1990) 656–659.
- [63] X. Li, B. Jin, J. Glimm, Numerical study for the three-dimensional Rayleigh–Taylor instability through the TVD/AC scheme and parallel computation, *Journal of Computational Physics* 126 (2) (1996) 343–355.
- [64] J.-L. Guermond, L. Quartapelle, A projection FEM for variable density incompressible flows, *Journal of Computational Physics* 165 (1) (2000) 167–188.
- [65] G. Tryggvason, Numerical simulations of the Rayleigh–Taylor instability, *Journal of Computational Physics* 75 (2) (1988) 253–282.
- [66] H. Ding, P. D. Spelt, C. Shu, Diffuse interface model for incompressible two-phase flows with large density ratios, *Journal of Computational Physics* 226 (2) (2007) 2078–2095.
- [67] D. Bhaga, M. Weber, Bubbles in viscous liquids: shapes, wakes and velocities, *Journal of fluid Mechanics* 105 (1981) 61–85.
- [68] G. Tryggvason, J. Lu, S. Biswas, A. Esmaeeli, Direct Numerical Simulations of Bubbly Flows, in: S. Balachandar, A. Prosperetti (Eds.), *Proceedings of the IUTAM Symposium on Computational Multiphase Flow*, Springer Berlin Heidelberg, 273–281, 2006.
- [69] J. Hua, J. Lou, Numerical simulation of bubble rising in viscous liquid, *Journal of Computational Physics* 222 (2) (2007) 769–795.
- [70] N. Balcázar, O. Lehmkuhl, L. Jofre, A. Oliva, Level-set simulations of buoyancy-driven motion of single and multiple bubbles, *International Journal of Heat and Fluid Flow* 56 (2015) 91–107.
- [71] J. Yan, S. Lin, Y. Bazilevs, G. J. Wagner, Isogeometric analysis of multi-phase flows with surface tension and with application to dynamics of rising bubbles, *Computers & Fluids* .

Appendix A. Proofs of some elementary propositions

Proposition 3. *The following identity holds:*

$$\frac{\partial \tilde{\phi}^k}{\partial x_j} \left(\frac{\partial}{\partial x_j} \left(\frac{\partial \tilde{\phi}^k}{\partial x_i} \right) \right) = \frac{1}{2} \frac{\partial}{\partial x_j} \left(\frac{\partial \tilde{\phi}^k}{\partial x_i} \frac{\partial \tilde{\phi}^k}{\partial x_i} \right) \quad (\text{A.1})$$

$\forall \tilde{\phi}^k, \in H^1(\Omega)$, where $\phi^k, \phi^{k+1}, \mu^k, \mu^{k+1}, \mathbf{v}^k, \mathbf{v}^{k+1}$ solves eq. (19) – eq. (23).

Proof. We just need to recall a vector identity to prove this. Recall the vector identities

$$\frac{1}{2} \frac{\partial (A_i A_i)}{\partial x_j} = \left(A_i \frac{\partial}{\partial x_i} \right) A_j + \epsilon_{ijk} A_j \left(\epsilon_{klm} \frac{\partial A_m}{\partial x_l} \right), \quad (\text{A.2})$$

$$\epsilon_{ijk} \frac{\partial}{\partial x_j} \left(\frac{\partial f}{\partial x_k} \right) = 0, \quad (\text{A.3})$$

where f is a scalar function and ϵ is the Levi-Civita symbol. In our case $A_j = \frac{\partial \tilde{\phi}^k}{\partial x_j}$, which causes the cross product term in eq. (A.2) to be zero from eq. (A.3), and which leads to the desired result. ■

Lemma 8. *The variational evolution term from the Cahn-Hilliard contribution in the momentum equation, eq. (19), can be written as follows:*

$$\left(\rho \left(\phi^{k+1} \right) \left(v_i^{k+1} - v_i^k \right), \tilde{v}_i^k \right) = \frac{1}{2} \int_{\Omega} \left\{ \rho \left(\phi^{k+1} \right) \|\mathbf{v}^{k+1}\|^2 - \rho \left(\phi^k \right) \|\mathbf{v}^k\|^2 \right\} d\mathbf{x} \quad (\text{A.4})$$

$\forall \tilde{\phi}^k, \phi^k, \phi^{k+1} \in H^1(\Omega)$, and $\forall \mathbf{v}^k, \mathbf{v}^{k+1} \in \mathbf{H}_0^1(\Omega)$, where $\mathbf{v}^k, \mathbf{v}^{k+1}, \phi^k, \phi^{k+1}$ satisfy eq. (19) – eq. (23), and

$$\|\mathbf{v}\|^2 := \sum_i |v_i|^2. \quad (\text{A.5})$$

Proof. We start with the left-hand side and expand into two terms:

$$\left(\rho \left(\phi^{k+1} \right) \left(v_i^{k+1} - v_i^k \right), \tilde{v}_i^k \right) = \frac{1}{2} \int_{\Omega} \left\{ \rho \left(\phi^{k+1} \right) \|\mathbf{v}^{k+1}\|^2 - \rho \left(\phi^{k+1} \right) \|\mathbf{v}^k\|^2 \right\} d\mathbf{x}, \quad (\text{A.6})$$

where we made use of the fact that $\tilde{v}_i^k = (v_i^{k+1} + v_i^k)/2$. Next we add and subtract the same term:

$$\begin{aligned} \left(\rho \left(\phi^{k+1} \right) \left(v_i^{k+1} - v_i^k \right), \tilde{v}_i^k \right) &= \frac{1}{2} \int_{\Omega} \left\{ \rho \left(\phi^{k+1} \right) \|\mathbf{v}^{k+1}\|^2 - \rho \left(\phi^{k+1} \right) \|\mathbf{v}^k\|^2 \right\} d\mathbf{x} \\ &\quad + \frac{1}{2} \int_{\Omega} \left\{ \rho \left(\phi^k \right) \|\mathbf{v}^k\|^2 - \rho \left(\phi^k \right) \|\mathbf{v}^k\|^2 \right\} d\mathbf{x} \\ &= \frac{1}{2} \int_{\Omega} \left\{ \rho \left(\phi^{k+1} \right) \|\mathbf{v}^{k+1}\|^2 - \rho \left(\phi^k \right) \|\mathbf{v}^k\|^2 \right\} d\mathbf{x} \\ &\quad - \frac{1}{2} \int_{\Omega} \left\{ \rho \left(\phi^{k+1} \right) - \rho \left(\phi^k \right) \right\} \|\mathbf{v}^k\|^2 d\mathbf{x}. \end{aligned}$$

Using eq. (16) we can evaluate the last term in the above equation as follows:

$$\begin{aligned}
-\frac{1}{2} \int_{\Omega} \left\{ \rho(\phi^{k+1}) - \rho(\phi^k) \right\} \|\mathbf{v}^k\|^2 d\mathbf{x} &= \frac{1}{2} \int_{\Omega} \frac{\partial}{\partial x_i} \left\{ \rho(\tilde{\phi}^k) \tilde{v}_i^k + \frac{1}{Pe} \tilde{J}_i^k \right\} \|\mathbf{v}^k\|^2 d\mathbf{x} \\
&= -\frac{1}{2} \int_{\Omega} \left\{ \rho(\tilde{\phi}^k) \tilde{v}_i^k + \frac{1}{Pe} \tilde{J}_i^k \right\} \frac{\partial}{\partial x_i} \|\mathbf{v}^k\|^2 d\mathbf{x} \\
&= -\frac{1}{2} \int_{\Omega} \left\{ \rho(\tilde{\phi}^k) \tilde{v}_i^k + \frac{1}{Pe} \tilde{J}_i^k \right\} 2v_i \frac{\partial v_i^k}{\partial x_i} d\mathbf{x} \\
&= 0,
\end{aligned} \tag{A.7}$$

where we used the solenoidality of the mixture velocity (see eq. (3)). This gives the desired result eq. (A.4). ■

Appendix B. Details of solver selection for the numerical experiments

For the cases presented in section 5.4 we use the BiCGStab linear solver (a Krylov space solver) with additive Schwarz-based preconditioning. For better reproduction, the command line options we provide PETSC are given below which include some commands used for printing some norms as well.

```

-ns_ksp_type bcgs
-ns_pc_type asm
-ch_ksp_type bcgs
-ch_pc_type asm
-ns_snes_monitor
-ns_snes_converged_reason
-ns_ksp_converged_reason
-ch_snes_monitor
-ch_snes_converged_reason
-ch_ksp_converged_reason

```

Here the prefix `-ch` is for applying the option to the Cahn-Hilliard solver, and `-ns` for the momentum solver respectively.

For the Rayleigh-Taylor instability case (section 5.5), which was significantly more expensive, we used an algebraic multigrid (AMG) linear solver with an additive Schwarz method (ASM) as a smoother. To improve the readability we separate the options for momentum and Cahn-Hilliard equations in two separate structures to input them into PETSC and the options are shown below.

```

solver_options_ns = {
    snes_atol = 1e-4
    snes_rtol = 1e-6
    snes_stol = 1e-5
    snes_max_it = 40
    ksp_rtol = 1e-5
    ksp_diagonal_scale = True
    ksp_diagonal_scale_fix = True

    #multigrid

    #solver selection
    ksp_type = "fgmres"
    pc_type = "gamg"
    pc_gamg_asm_use_agg = True
    mg_levels_ksp_type = "bcgs"

```

```

    mg_levels_pc_type = "asm"
    mg_levels_sub_pc_type = "lu"

    #performance options
    mattransposematmult_via = "matmatmult"
    pc_gamg_reuse_interpolation = "True"
    mg_levels_ksp_max_it = 20
};

solver_options_ch = {
    snes_atol = 1e-12
    snes_rtol = 1e-8
    snes_stol = 1e-10
    snes_max_it = 20

    # multigrid
    ksp_type = "fgmres"
    pc_type = "gamg"
    pc_gamg_asm_use_agg = True
    mg_levels_ksp_type = "bcgs"
    mg_levels_pc_type = "asm"
    #performance options
    mattransposematmult_via = "matmatmult"
    pc_gamg_reuse_interpolation = "True"
    mg_levels_ksp_max_it = 4
};

```

The linear systems we handle are fairly ill-conditioned, therefore, the smoothers we need to use are fairly expensive. The ASM/LU based smoother is more expensive compared to other smoothers like block Jacobi, however ASM/LU is more robust (better convergence). This setup works very well with a relatively constant number of Krylov iterations as the number of processes are increased in the massively parallel setting. The scaling results we present use the same setup of solvers, but there is substantial room for improvement in this area of the code where fieldsplit preconditioners using Schur complement can be used as smoothers to improve speed of the AMG solver.